NEARBY INTERACTING GALAXY PAIRS: DYNAMICS AND IONIZED GAS PROPERTIES

by

S. Alireza Mortazavi

A dissertation submitted to The Johns Hopkins University in conformity with the requirements for the degree of Doctor of Philosophy.

Baltimore, Maryland

August, 2016

Abstract

Galaxy merging is an important process in galaxy formation and evolution throughout the cosmic time. Mergers are expected to play a significant role in galaxy mass assembly and transformation of galaxy morphology. In this work, we study interacting pairs of galaxies in a relatively early stage of the merging process, after they first pass by each other but before they coalesce into a single galaxy. At this stage, interacting disk galaxies display peculiar morphologies, often induced by the strong gravitational tidal field experienced during the first passage. These peculiar features can be utilized to constrain the encounter parameters of the merging galaxies, such as time since first passage, and pericentric separation (Toomre & Toomre, 1972; Hibbard & Mihos, 1995; Barnes & Hibbard, 2009). Moreover, in the early stages of galaxy mergers the individual galaxies are still clearly separated making it possible to investigate the chain of physical processes that are caused by the interaction. This includes starbursts or active galactic nuclei (AGNs) triggered by the infall of gas into the cores (Mihos & Hernquist, 1996; Hopkins & Quataert, 2011), and the shocks that are produced by feedback from starbursts and AGNs (Cox et al., 2006b; Narayanan et al., 2008; Rich et al., 2015), or by collision of gaseous clouds in the interstellar medium (ISM) of the two disks as they pass through each other (Struck, 1997).

We develop a novel automated method for modeling the dynamics of equal mass galaxy mergers that puts meaningful constraints on the system's encounter parameters. In order to understand the systematics of the measured encounter parameters, we test our method against an independent set of galaxy merger simulations with known initial conditions. For a controllable subset of these tests, our automated method recovers parameters such as merger stage and initial disk orientations within 3σ of the correct value.

We explore the effects of using different kinematic tracers on the inferred encounter parameters by applying our method to HI and Hα velocity maps of a well-studied galaxy merger system in the nearby Universe, NGC 4676 a.k.a the Mice galaxies. We show for the first time that constraints on the encounter parameters derived from HI and Hα kinematics are consistent suggesting that Hα velocity maps can also be used for dynamical modeling.

In total we observe a sample of 22 galaxy mergers in this work. Nineteen of them have morphological indicators similar to the Mice galaxies (separate cores and strong tidal features), and the other three are recently coalesced systems where cores are united, but outskirts are still disturbed. We use SparsePak integral field unit (IFU) (Bershady et al., 2004) on the WIYN telescope at Kitt Peak National Observatory (KPNO) to observe the Hα emission over the entire visible regions of these galaxies, including faint tidal tails. Relatively high spectral resolution of our data allows us to investigate multiple kinematic components in the emission lines. We separate Hα emission of photo-ionized HII regions from shocked gas, measure the velocity maps of HII regions, and discuss the fraction and spatial distribution of shocks and their power source. We apply our dynamical modeling method on equal mass systems in our sample and obtain the first ever constraints on the encounter parameters of one of them. We find a trend between shocked gas fraction and the projected separation between the galaxies in pairs, similar to Rich et al. (2015). In our sample of interacting pairs, for the first time, we also find a trend between shocked gas fraction and the light ratio (mass ratio). These trends suggest that in most of the observed systems the gravitational tidal impulse at the time of the first passage is the dominant origin of shocks. Also for the first time, we investigate the correlation between shocked gas fraction and encounter parameters from dynamical modeling. We find that time until coalescence and pericentric separation are both strongly anti-correlated with the amount of shocks. However, larger statistical sample is required for understanding the physical details and timing of shock production during galaxy mergers. Clean separation of shocks from star forming regions also improves the accuracy of star formation rate measurements in merging galaxies.

Large ongoing and upcoming IFU galaxy surveys such as MaNGA (Bundy et al., 2015) will provide spatially resolved spectra of large numbers of galaxies including many galaxy mergers. Tools and techniques developed for this thesis project are required steps for better utilization of these valuable datasets.

Primary Reader: Jennifer Lotz

Secondary Reader: Colin Norman

Acknowledgments

I would like to begin by thanking my advisor, Jennifer Lotz, without whom I would not have finished my PhD. Since I began working with her in the beginning of 2011, she has been a great mentor for me, guiding me to ask the right question, and patiently helping me to find the right track toward the answer. She has been kind and understanding throughout the challenging days of graduate school, and I could not have asked for a better advisor.

Many thanks to Colin Norman, for all his support during my graduate studies, and to Gregory Snyder who generously helped solving problems that we could not solve without him. I would like to thank my other colleagues, Joshua Barnes, Ron Allen, T.J. Cox, David Law, George Privon, and Mike Peth.

Thanks to my friends with whom I had a pleasant time in the department of Physics and Astronomy at JHU, including Veselin Kostov, Bingxiao Xu, Anirban Ghosh, Margi Gabellini, and particularly, Cathy White whose revision significantly improved this work, and Mohammadtaher Safarzadeh with whom I had many exciting and intellectual conversations. I would like to thank my Iranian friends in Baltimore,

who have been like my family, and unfortunately, I do not have room here to thank them individually. Thank you all!

And, more important than all, I would like to thank my family, my loving father whom I lost during the course of my graduate studies, my mother who has been my biggest encourager to be curious and learn since I was a little kid, and my brothers, sister, and sister-in-laws, who never stopped supporting me in every possible way they could. I am indeed lucky to have such a family.

At last, I would like to acknowledge resources I used during the course of this project. This project was supported in part by the STScI DDRF. This work used the Extreme Science and Engineering Discovery Environment (XSEDE), which is supported by National Science Foundation grant number ACI-1053575 (See Towns et al. 2014).

In the name of Allah the All-beneficent the All-merciful

To the awaited one

Oh Allah! Be for Your Wali,
Hujjat (Proof) son of alHassan [Imam Mahdi],
Your blessings be upon him and his fathers,
in this moment and in every moment,
a Guardian,
a Protector,
a Leader,
a Helper,
a Proof,
and an Eye,
until the time that You establish him on your earth with obedience,
and You make him rejoice, in it, for a long time.

Contents

List of Tables

List of Figures

Chapter 1

Introduction

In this thesis, we investigate the properties of merging disk galaxies in the nearby Universe. Galaxy mergers play an important role in galaxy formation and evolution by contributing to galaxy mass assembly and transforming galaxy morphology. We use the peculiar shapes and kinematics of galaxy mergers to constrain the encounter parameters such as the merger stage. We also investigate the properties of ionized gas in interacting disk galaxies.

1.1 Galaxy Mergers in a Cosmological Context

Galaxy mergers are central to our understanding of how the Universe has come to its current status. Observational and theoretical evidences suggest that galaxy mergers are frequent and significantly affect the properties of of galaxies. We review some of these evidences in this section.

1.1.1 Hierarchical Galaxy Formation

In the standard Λ cold dark matter (ΛCDM) cosmology, structures form hierarchically, such that small structures form early and grow with time through mergers and accretion of new material (White & Rees, 1978). About 100 million years after the Big Bang, the primordial perturbations in the early Universe started to grow non-linearly. Since then, the gravitational force have been at work driving the matter into large scale structures such as sheets, filaments, and clusters, known as the cosmic web. As dark matter flows along the cosmic web it forms gravitationally bound halos. Dark matter halos grow in form of smooth mass accretion or the infall of other bound halos. Galaxies that live in the center of merging halos will eventually merge as well. About 5-10 % of galaxies in the nearby Universe seem to be in the process of merging based on their disturbed morphology (e.g. Bridge et al. 2010). Cosmological simulations indicate that dark-matter halos (and thus the galaxies they contain) have been merging at even higher rates at earlier times (Genel et al., 2009; Fakhouri et al., 2010). Recent hydrodynamical cosmological simulations have found a similar trend for galaxy merger (Rodriguez-Gomez et al., 2015), consistent with observations of galaxy merger rates at different redshifts (Lotz et al., 2011). An average galaxy has probably experienced about one major merger since $z\sim$2-3. (See also Kartaltepe et al. 2007; Jogee et al. 2009.)

While the significance of mergers in the assembly of the total stellar mass of galaxies is a matter of debate, it is widely believed that a considerable fraction of stellar mass of the most massive galaxies in today's Universe are formed ex-situ, meaning that major and minor mergers have brought the pre-formed stars into the final galaxy.[1] For example, Rodriguez-Gomez et al. (2016) show that in the Illustris hydrodynamical cosmological simulations (Genel et al., 2014), about 80 percent of galaxy stellar mass of redshift zero galaxies with stellar masses of $\approx 10^{12} M_{\odot}$ have been formed ex-situ. They also show at a fixed stellar mass galaxies with morphologies similar to early-type galaxies (ETGs) have a higher fraction of ex-situ stars compared to late-type galaxies.

1.1.2 Morphological Transformation

Changes in the shapes, sizes, and colors of galaxies over the last 10 billion years have been observed by many groups. Star-forming disk-dominated galaxies at redshift z$\sim$ 2 have transformed into quiescent bulge dominated ones today (Bell et al., 2004; Faber et al., 2007; Brown et al., 2007). Toomre (1977) first introduced what was later known as the "merger hypothesis," suggesting that today's giant ellipticals could be the remnants of major galaxy mergers.[2] Stars in merging rotation-supported disk

---

[1] This is opposite of in-situ star formation, where stars are formed inside the galaxies out of the gas accreted from the cosmic web.

[2] Usually major and minor merger are defined with mass ratio, $\mu < 4$ and $\mu > 4$, respectively. Here mass ratio is defined as $\mu = \mathrm{M}_{\mathrm{primary}}/\mathrm{M}_{\mathrm{secondary}}$. Some authors also separate very minor

galaxies can settle via violent relaxation into a dispersion-supported remnant similar to elliptical galaxies. Minor mergers with a primary galaxy made of a thin disk can increase the velocity dispersion and thicken the disk in a similar fashion (Quinn et al., 1993; Kazantzidis et al., 2008; Moster et al., 2010). In the most extreme case, the merger hypothesis suggests all galaxies are originally formed as thin disks, and the variety of the bulge fraction, and disk thicknesses of today's galaxies result from their different merger histories. Although other scenarios are suggested for the formation of bulges (Kormendy & Kennicutt, 2004), major mergers and minor mergers remain a strong candidate to explain the transformation of galaxies.(See also Naab & Burkert 2003; Cox et al. 2006a.)

Photometry and kinematics of elliptical galaxies have shown that they can be classified into two groups: low- and intermediate-mass ellipticals display fast rotation along the photometric major axis (Emsellem et al., 2007, 2011), have disky isophotes and steep power law central light profiles (Faber et al., 1997), and have little or no X-ray or radio emission (Bender et al., 1989). Large luminous ellipticals, on the other hand are boxy, have flat cores, display strong radio or X-ray emission, rotate slowly, occasionally have kinematically decoupled cores, and show significant rotation along the minor morphological axis (Cappellari et al., 2011; Emsellem et al., 2011; Krajnović et al., 2011). Disk merger simulations have had some success in reproducing some of these properties in the simulated merger remnants, especially for the fast-rotating

---

mergers with $\mu > 10$.

ellipticals, but the full scope of the rotational properties of nearby ellipticals is hard to model with current disk-disk major galaxy merger simulations, and require better understanding of the assembly history of the elliptical, as well as the role of gas fraction, initial disk orientation, and the supermassive black hole (SMBH) during the merger (Boylan-Kolchin et al., 2005; Robertson et al., 2006; Burkert et al., 2008; Bois et al., 2011; Naab et al., 2014).

Galaxies have also been observed to be more compact at high redshift. Massive galaxies at z$\sim$2 have central stellar mass densities that are rarely found in nearby Universe (van Dokkum et al., 2008; Damjanov et al., 2009). The formation of these ultra-compact galaxies are still not very well understood (Wellons et al., 2015), though we know that they grown in size since then. van Dokkum et al. (2010) showed that massive galaxies in the nearby Universe have grown in mass by a factor of 2 compared the their possible progenitors[3] at $z = 2$, but almost all of the mass growth has happened in the outskirts at 5 kpc$< r <$75 kpc. They explain this by minor mergers through which smaller galaxies deplete their stars into the outskirts of the primary galaxy. (See also Oser et al. 2012.)

1.1.3 Merger-Induced Activity in Galaxies

There is evidence that galaxy mergers enhance star formation and AGN activity in participating galaxies. Many of the nearby starburst galaxies with infrared (IR) lumi-

---

[3] They compare galaxy populations in mass bins with the same number density at different redshifts, arguing that most galaxies stay in the same number density bin over cosmic time.

nosity $> 10^{11}\mathrm{L}_\odot (> 10^{12}\mathrm{L}_\odot)$ known as (ultra)luminous infrared galaxies or (U)LIRGs show signatures of mergers (Sanders & Mirabel, 1996). Galaxy merger simulations suggest that that at early stage of interaction star formation is enhanced in the center of the merging galaxies as a result of gas inflows (Barnes & Hernquist, 1996; Mihos & Hernquist, 1996; Cox et al., 2008). Several groups have observed enhancement in the star formation of mophologically perturbed galaxies and close galaxy pairs, compared to isolated galaxies (Larson & Tinsley, 1978; Nikolic et al., 2004; Patton et al., 2005; Geller et al., 2006), and some have claimed to see this enhancement in the center as is expected by inflows (Smith et al., 2007). There is evidence that starburst happens not only in the center of interacting galaxies but also in large scale structures (Whitmore & Schweizer, 1995; de Grijs et al., 2003). The extra-nuclear merger-induced starburst is believed to be made by shocks. As the neutral interstellar gas in the two disks collide, it heats up. Hot gas over-pressurizes the outer layers of preexisting giant molecular clouds (GMCs), compressing them through radiative shocks. This makes these layers gravitationally unstable, triggering bursts of star formation (Jog & Solomon, 1992; Barnes, 2004). Star formation enhancement seems to be stronger in major galaxy mergers compared to minor ones (Ellison et al., 2008).

Major and minor mergers are also believed to enhance AGN activity in galaxies. The inflow of gas caused by the interaction can reach the supermassive black hole (SMBH) in the center of the galaxy and turn on the AGN. Hopkins et al. (2008) showed that the simple Ansatz that major gas-rich mergers have a fixed probability of causing quasar activity naturally reproduces some of the observable manifestations of quasars at different redshifts, such as clustering and luminosity function. Observation of hosts of the most luminous obscured quasars at z$\sim$1.5 have shown that about half of them show signatures of recent or ongoing merger activity which is much higher than the fraction of $\sim 15\%$ in non-quasars (Glikman et al., 2015; Wylezalek et al., 2016). At lower redshifts, galaxies in close pairs in Sloan Digital Sky Survey (SDSS) are more likely to host AGN than isolated galaxies (Ellison et al., 2011).

The gas in merging gas-rich galaxies heat up with shocks in different modes. Inflows (outflows) into (out of) the central starburst or AGN collide with the gas in lower (larger) orbits and produce shocks. In addition, during collisions with certain geometries, gas in the ISM of the two galaxies can directly collide at high velocities and form shocks Struck (1997). Both outflows and direct collision of gas during the merger may strip off or heat up the gas in the galaxies, removing the fuel for further star formation.

1.1.4 Role of Mergers in Quenching Star Formation

Cosmic star formation has decreased by a factor of ~ 10 since the peak at z$\approx$2 (e.g. Lilly et al. 1996; Madau et al. 1996; Hopkins & Beacom 2006). Star forming galaxies at z$\approx$2 form stars at a much higher rate than their counterparts in the nearby

Universe (Erb et al., 2006). Understanding what quenches the star formation and how gas and star formation rate (SFR) regulate in galaxies over the entire cosmic history are among fundamental questions in modern astronomy. Superwinds from starbursts and AGNs are candidates for suppressing star formation in low and high end of galaxy luminosity(mass) function, respectively (Benson et al., 2003). The outflowing material, strips the gas off the galaxies and remove the fuel for further star formation. In addition, gravitational shock heating of the gas infalling into massive dark matter halos provide another pathway for disconnecting the fuel supply for star formation, and making the giant galaxies quiescent (Birnboim & Dekel, 2011).

Galaxy mergers may play a role in quenching the star formation in galaxies over cosmic time. Starburst and AGN activity induced by galaxy interactions can produce strong outflows. These outflows, along with the the tidal disruptions and striping (Narayanan et al., 2008), and sometimes, collision of gas clouds in the interacting galaxies (Struck, 1997; Amram et al., 1998) remove the cold gas supply, and contribute to quenching of the post-merger remnants. The role of mergers in the quenching process is still a matter of debate.

1.2 The Physics of Galaxy Interactions

During the interaction of an isolated pair of galaxies, gravitational tidal forces play the most important role in the evolution of the galaxies. When an extended object is in the vicinity of another mass, the gravitational force from the secondary mass (perturber) on different parts of the extended primary object varies because the secondary is at slightly different distances to different parts of the primary. As a result, an observer on a frame attached to the center of mass of the primary will see that different parts of the primary experience tidal accelerations with respect to each other. These forces affect the morphology and kinematics of interacting galaxies and can strip them off material, including gas, stars, and dark matter. In this section, we discuss how tidal interactions work, and how they affect the overall shape of the galaxies and the properties of the gas in them.

1.2.1 Tidal Forces

A simplified one-dimensional treatment of the tidal acceleration induced by a point mass M at distance R from an extended object with mass m is

$$a_t \approx \pm \hat{r}\ 2\Delta r G \frac{M}{R^3}, \tag{1.1}$$

where Δr is the distance from the center of extended object, m, where the tidal acceleration is felt, and $\hat{r}$ is the unit vector in the direction of the perturber. Here, we have used an approximation of $\Delta r/R << 1$.[4] According to this simple calculation, tidal force on an extended object depends on the inverse cube of the distance to the

---

[4] For a more detailed three dimensional treatment of the problem refer to Binney & Tremaine (2008)

perturber, so it is relatively a stronger function of distance compared to gravitational force between point masses. It also depends on the mass of the perturber; a more massive perturber at a closer distance induces stronger tidal forces.

The tidal forces affect the interacting galaxies in two different regimes. When the velocity of the interacting galaxies passing by each other is high, the time in which they experience the tidal acceleration is short. Tidal force is weak when the galaxies are far apart, kicks in when they pass by each other, and fades away quickly when they depart. In this case, galaxies experience an "impulsive" tidal force. When galaxies interact in a highly non-circular orbit, they experience an impulsive tidal force. On the other hand, when the galaxies are in a circular orbit, they experience a "static" tidal force. Continuous tidal acceleration on stellar systems can remove the outermost stars, hence putting an upper limit on their size. (See Binney & Tremaine 2008.)

Interacting galaxies of similar mass are usually in non-circular orbits in a ΛDCM Universe. Dark matter cosmological simulations predict that most of dark matter halo mergers in the Universe start from parabolic orbits with eccentricity$\approx$1. They suggest that only a small fraction of orbits have eccentricities smaller than 0.6 (Benson, 2005; Khochfar & Burkert, 2006). Encounters happen as galaxies and dark matter halos they live in move along the cosmic web. Their initial kinetic energy relative to each other is usually very small at far distances, so as they approach each other their orbit has almost zero mechanical energy, corresponding to parabolic orbits. Keplerian parabolic orbit is unbound for point masses, but for galaxies and dark matter halos, the orbits decay rapidly due to tidal interaction and (dynamical) friction after the first close passage. Orbital decay causes the galaxies to coalesce in timescales $<\approx 1$ Gyr, much shorter than the age of the universe. If closely interacting galaxies are to be found in a circular orbit they should have entered this highly bound state (probably by a third object) less than ~ 1 Gyr ago, otherwise one needs to answer why they have not merged earlier. This is also true for elliptical orbits with low eccentricity. Therefore, we assume that observable binary major and minor mergers in the field are in non-circular orbits where impulsive tidal forces are at play.

1.2.2 Tidal Features in Interacting Disks

The impulsive tidal force at the pericenter changes the velocities of particles in the disks, but their positions are almost unchanged.[5] The velocity impulse changes the trajectory of particles and make them occupy new regions of phase space forming the "tidal features". These features grow as galaxies departs after the first passage. The features that grow toward the companion are called "bridges", and the ones that grow in the opposite direction are called "tails" (Toomre & Toomre, 1972).

To form long-lived tidal bridges and tails, interacting galaxies must be either disk-dominated of any size, or be a dwarf interacting with more massive galaxy. Thin tidal

---

[5] This criteria is satisfied when the crossing time for each galaxy is much larger than the time during which the tidal forces are significant. This is called the "impulse approximation" (Binney & Tremaine, 2008).

tails must have high phase-space densities; the spatial density must be high if the tail is to be observable, and the velocity dispersion must be low[6] or otherwise the tail (or bridge) would rapidly disperse. High phase-space density is satisfied either when the tidally affected companion has a much lower mass compared to the perturber (hence, it has less velocity dispersion and high enough mass density), or when the interacting galaxies are dynamically cold as in disk galaxies. The former is the case of tidal streams observed between the Large and Small Magellanic Clouds in the vicinity of our Galaxy.

Strong tidal tails and bridges in a pair of interacting disk galaxies with distinct cores suggests that the galaxies have passed by each other at least once, and they are likely to be on their ways to a second passage. Tidal features are typically not prominent before the first passage.[7] On the other hand, It is less likely to see an interacting pair of galaxies in the time interval after the second passage and before the coalescence , i.e. when the two cores are not distinguishable anymore. It takes a small fraction of the time between the first and the second passages for the galaxies to unify after the second passage. The energy and angular momentum of the orbit decay during the first passage and between the first and second passages. At the second passage galaxies have a much lower orbital angular momentum and pericentric separation compared to the first passage, so they do not separate much after the second passage. They rapidly fall back on each other and merge. So, when we

---

[6] Low velocity dispersion is equivalent of high velocity density in phase-space.

[7] This is not true when the orbit of galaxies are close to circular. But, as discussed above, eccentricity < 0.6 is not likely among similar mass galaxy mergers.

observe a pair of disk galaxies with strong tidal features and distinct cores, it is likely that we are looking at them between the first and the second passage.[8]

The orientation of the disks with respect to the angular momentum of the orbit strongly affects the strength of the tidal features. Toomre & Toomre (1972) showed that “prograde” orbits, in which the orbital angular momentum is aligned with the disk spin, produce far more prominent tidal tails. During a prograde passage, particles in the disk rotate in the same direction as the perturber, so they experience tidal forces pulling (pushing) them in the same direction throughout the encounter. In other words, particles of a prograde disks are in resonance with the changes of tidal acceleration (Mo et al., 2010). On the other hand, in “retrograde” disks, when the disk spin is anti-aligned with the orbital angular momentum, the tidal forces act in opposite directions on the same particles in the disk as they cross the tidal field, so the net tidal force experienced by the disk material is minimized and tidal features are weaker.

When the galaxies collide with an inclination close to 90° with respect to the orbital plane, they are in so-called “polar” orbits. Collisions of disks in polar orbits with small impact parameter (or pericentric distance) may produce tidal features in the form of rings[9] (Theys & Spiegel, 1977). The tidal forces at the time of collision,

---

[8] Note that in some orbits with large pericentric distance, and eccentricity > 1 the galaxies may separate significantly after the second passage. Though, The fraction of time between the second passage and coalescence to the time between the first and second passages is still small, and our argument still holds.

[9] The argument at periapsis, ω of the disk should be close to 90° or (270°) to make rings, so the companion falls through the disk from a direction almost perpendicular to the disk and near the center.

induce radial oscillations in the circular orbits of the rotating material. The frequency of radial oscillations depend on radius of the orbits, so the oscillating particles produce a ring-like density-wave moving outward. (See Chapter 8.5 of Binney & Tremaine 2008 and references therein.) The high gas density in the ring may trigger star formation, consistent with observations of star forming rings similar to the Cartwheel galaxy (Figure 1.1).

To produce significant tidal features from a disk, its size needs to be large enough so that the tidal impulse is able to significantly affect the material in the outskirts. In other words, if the disk is small, or the gravitational potential well is too deep all the way to the outer parts of the disk, the tidal acceleration will not be comparable to the self-gravity of the galaxy, and disk particles will not be much affected. Springel & White (1999) show that under favorable conditions, quantity

$$\mathcal{E} = \frac{{v_{esc}}^2}{{v_{circ}}^2}$$

should be less than 6.5 for the disks to form tidal tails in equal-mass encounters. Here, v_{esc} and v_{circ} are the escape velocity and circular velocity in the disk, respectively, measured at the half mass radius. It is worth noting that this quantity is 2 for Keplerian central potential which was used originally in the simplified simulations of the revolutionary work of Toomre & Toomre (1972). In order to produce strong tidal features in encounters with mass ratio $\mu \neq 1$, the mass of the companion galaxy must

(a)

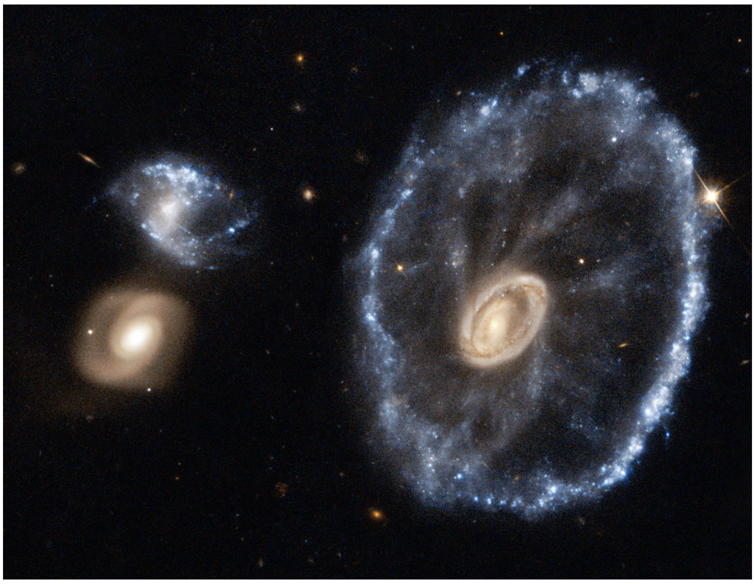

(b)

Figure 1.1: (a) The Mice galaxies (NGC 4676A/B): This system reveals strong tidal features in both galaxies. The width of the image is about 100kpc. Strong tidal tails in both systems indicate comparable masses. Dynamical models of this system suggest that the galaxies have first passed by each other at 170-210 Myr ago. We present a new model of this system using both HI and Hα kinematics in Chapter 3. (b) The Cartwheel galaxy. The radius of the ring is about 45 kpc. The lower left galaxy is likely to be responsible for the ring through a collision that occurred 210-720 Myr ago (Amram et al., 1998). The blue color of the ring indicates that it is the site of star formation. (NASA/ESA/STScI)

be either comparable or bigger. In systems like NGC 4676 (the Mice galaxies) where we find strong tidal tails in both systems, we can argue that galaxies should have similar mass. For the case of the Mice galaxies, stellar mass ratio is ≈1.25 (Wild et al., 2014), confirming this argument (Figure 1.1a).

Barnes (2016) explores a large number of equal mass galaxy mergers with a variety of internal parameters, looking for insights on the effect of the mass profile of disk and dark matter halo on the tidal morphology. He explores halo concentration parameter, disk compactness, and luminous fraction as internal parameters of isolated galaxies. He confirms that galaxies with $\mathcal{E} > 6$ make tidal features that are short-lived and rapidly reaccrete back to the disks. He also suggests that among the explored parameters, luminous mass fraction[10] is the one that can be constrained by detailed modeling of individual systems between the first and the second passages.

1.2.3 Gas in Interacting Galaxies

Galaxies contain both collisionless and collisional particles. Collisionless particles like dark matter and stars[11] only interact via gravitational force. Gas particles, however, are collisional, and experience electromagnetic forces from each other along with the gravitational forces from the rest of the matter. Dissipation heats up the

---

[10] luminous mass fraction = $(\mathrm{M}_{\mathrm{bulge}} + \mathrm{M}_{\mathrm{disk}})/(\mathrm{M}_{\mathrm{halo}} + \mathrm{M}_{\mathrm{bulge}} + \mathrm{M}_{\mathrm{disk}})$

[11] Stars are fundamentally collisional as they are made of baryons, though because of very small collisional cross section compared to their typical number density in galaxies, they have a mean free path, much longer than the size of the galaxy, and so they are very unlikely to collide during encounter of galaxies.

gas, forcing it to radiate in different forms. Gas plays an important role in shaping the galaxy properties during the merger event as it can loose kinetic energy from the encounter through radiation. So far in the section, we have been discussing the effect of tidal forces in producing tidal tails, bridges, and rings. These features are produced in the outskirts of interacting rotating disks for both collisionless and collisional particles. In this section, we briefly review how collisional properties of the gas function during galaxy interactions.

1.2.3.1 Tidal Inflows, Metallicity Gradients, Starbursts, and AGNs

Tidal impulse during the first passage changes circular orbit of stars and gas in the disk. If the tidal impulse is strong enough [12], the originally circular orbits start to cross each other. Orbital crossings produce a bar-like structure in the center of the disk both for the gas and stars. However, collisionless stars cross the orbit of each other with no resistance from other stars, but gas particles dissipate as they cross each other and form a bar that is mis-aligned with the stellar bar. The mis-alignment between the the gaseous and stellar bars exerts tidal torques on the gaseous bar, and drains a large fraction of angular momentum of the gas. In a fraction of the orbital period gas can lose upto 95% of its angular momentum and fall into a dense rotating disk with a radius less than 0.5 kpc (Mihos & Hernquist, 1996; Barnes & Hernquist,

---

[12] Usually in close encounters of prograde disks

1996). This pile up of gas in the central region has been observed in many interacting galaxies in the local Universe (e.g. Yun & Hibbard 2001).

Gas inflow after the first passage and at the time of coalescence reveals itself in the flattening of the metallicity gradient from the center to the outskirts of the interacting pairs. Most isolated spiral galaxies display a strong metallicity gradient: gas in the outskirts have lower metallicity than gas near the center (Henry & Worthey, 1999). Observations have shown that similar galaxies in close pairs systematically have less metallicity in the center (Lee et al., 2004; Kewley et al., 2006a) or display flatter metallicity gradients (Kewley et al., 2010). These observations suggest that because of the interaction, metal poor gas in the outskirts flow toward the center, consistent with predictions by hydrodynamical simulations (Torrey et al., 2012).

High gas surface density in the central region can trigger rapid star formation a.k.a. starburst, or fuel AGN. The starburst can occurs at two times: a weaker burst when the galaxies first pass and tidal torques produce the inflow of gas toward the still separate centers, and a stronger one when the two galaxies violently coalesce, and gas in the tidal tails fall back and feed the core. (See Mihos & Hernquist 1996; Barnes & Hernquist 1996; Cox et al. 2006b, 2008 for simulations, and Hibbard & Mihos 1995; Sanders & Mirabel 1996; Barton et al. 2000; Ellison et al. 2008; Patton et al. 2011 for observations). The inflowing gas can reach to much lower radii and accrete onto and grow the supermassive black hole (SMBH) in the center, triggering AGN activity (Norman & Scoville, 1988; Springel et al., 2005; Hopkins et al., 2006).

Similar to star formation enhancement, merger induced AGN activity is observed both in pairs after first passage (Ellison et al., 2011), and in tidally disturbed merger remnants (Wylezalek et al., 2016). Both simulations and observations suggest that AGN activity lags the onset of starburst by a few million years (Wild et al., 2010; Hopkins & Quataert, 2011).

1.2.3.2 Outflows and Feedback in Mergers

Starburst and AGN enhanced by mergers, produce strong outflowing superwinds, dragging away the gas from the ISM, and hence, regulating the black hole growth and star formation rate (Silk & Rees, 1998; Fabian, 1999; Cox et al., 2006b; Narayanan et al., 2008). It has been argued that feedback by supernova explosions, along with the stellar winds and radiation pressure are effective in heating or removing the gas reservoir in low luminosity (low stellar mass) galaxies with stellar masses $<\approx 10^8 \mathrm{M}_\odot$. However, feedback from rapid star formation is not energetic enough to remove gas from the deep gravitational potential well of most massive galaxies, yet we know that these galaxies are quiescent in the nearby Universe. Strong AGN feedback is believed to be the mechanism that strips off (or heats up) the gas in the most massive galaxies and stops further star formation (Benson et al., 2003). It is also shown that in hydrodynamical simulations, the details of implementing feedback is important for reproducing galaxies with realistic central dark matter distribution and large enough disk angular momentum (Governato et al., 2009, 2012). At this point, the role of feedback from SMBH in determining properties of galaxies is uncertain.

1.2.3.3 Shocked gas in interacting galaxies

During the galactic encounter gas flows of different velocities may collide. Gas in the ISM of individual galaxies may find itself flowing into the ISM of the companion, occasionally at high speeds. This depends on the encounter parameters, particularly the pericentric separations and the orientation of the disks (Struck, 1997). Earlier, we mentioned other processes that produce gas flows in the interacting galaxies. Tidal impulse causes inflow of gas after the first passage. This ignites starburst and AGN, which subsequently produce strong outflows through winds. High velocity collision of inflowing and outflowing with the interstellar medium also produce shocks.

During galactic encounter, high-speed collisions between gas flows produce galaxy-wide shocks. Shocks are pressure-driven disturbances that move faster than the sound speed of the ambient medium (Landau & Lifshitz, 1959). Almost all phenomena that produce shocks in the ISM tend to be enhanced as a result of galactic encounters. Merger-induced starbursts can produce strong stellar winds (Heckman et al., 1990). Fast winds move freely away from the young stars until they reach ISM, then they decelerate by passing through a shock wave. Rapid star formation leads to rapid stellar explosion rate, SNe, which drive shocks into the ISM. AGN activity can produce fast winds and shocks in the same way. Expanding HII regions can drive shocks into the neighboring neutral gas as well.[13] Gas in the ISM of the two interacting galaxies may directly collide with each other at supersonic speeds (Struck, 1997).

In the shock front, large amounts of initial kinetic energy in the colliding gas flows dissipate into heat. Shocks can heat up the interstellar medium from 10^4 to 10^7 K, depending on the speed of the flows, the density of gas particles and their pre-shock ionization state (Draine, 2011). The post-shock gas is ionized, and cools down via radiation. The post-shock gas is also highly turbulent, displaying high velocity dispersion in the nebular emission lines. Velocity dispersion and ratio of flux in optical emission lines depend on shock velocity and the properties of pre-shock medium (Dopita & Sutherland, 1995). Sometimes the shocked gas is hot enough to cool via bremsstrahlung radiation, displaying extended X-ray source (Appleton et al., 2015).

Processes that produce shocks are similar in nature to the processes that supposedly quench star formation in galaxies, i.e. the outflows from starbursts and AGN. Outflows produce shocks as they heat-up and swipe the gas out. Direct collision of ISM of an interacting pair also strips the disks of their gas content in certain collision geometries. Ram pressure on colliding ISMs blow them away, leaving a trail of shock-heated gas between the galaxies (Struck, 1997). This suggests that shocks are directly related to quenching. Better characterization of shocks in interacting galaxies will help us better understand the role of mergers in quenching star formation in

---

[13] For an overview of these processes see Chapters 36 to 39 of Draine (2011)

galaxies.

Modern integral field spectroscopy (IFS) provides a powerful tool to look for shocks throughout the interacting galaxies. It provides spatially and spectrally resolved information that extends to outskirts, and can be used to distinguish different power sources of ionization (Monreal-Ibero et al., 2010a; Rich et al., 2011; Davies et al., 2014; Leslie et al., 2014; Medling et al., 2015). In Chapter 4 of this thesis we use our IFS observations of a sample of 22 galaxy merger systems to explore the effect of encounter parameters on the physical distribution and fraction of ionization by shocks..

1.3 Measuring Encounter Parameters

When we observe an interacting pair of galaxies, we are looking at a very brief snapshot of the collision, because the duration of a galactic collision from first passage to coalescence is of the order of hundreds of million years, much longer than the age of human civilization on earth. We do not have the luxury of watching a galaxy merger as it happen and investigating how properties of galaxies change with time during the process. In many cases, it is not even trivial to determine whether we are looking at a snapshot at an early stage or at a late stage of the process. However, it has been shown that utilizing the morphology and kinematics of the tidal features produced during disk-disk galactic colissions, one can put strong constraints on the encounter parameters (Toomre & Toomre, 1972; Hibbard & Mihos, 1995; Barnes & Hibbard, 2009; Barnes, 2011; Privon et al., 2013; Holincheck et al., 2016). In this section we discuss why these constraints are important, and we review some of the previous attempts to find them.

1.3.1 Motivation

Measuring encounter parameters of interacting galaxies helps to put indirect constraints on different areas of galaxy formation. For instance, measurement of the encounter parameters from tidal morphology and kinematics can be used to put independent constraints on models of star formation in hydrodynamical simulations. As discussed earlier, galaxy mergers can induce starbursts. Hydrodynamical simulations of galaxy mergers indicate that timing, strength and the age of starburst induced by mergers depend on their encounter parameters, such as mass ratio, pericentric separation, and disk orientation (Cox et al., 2006b, 2008; Snyder et al., 2011). On the other hand, the details of the star formation and feedback sub-grid model in these simulations also affect when, where, how much merger-induced star formation occurs (Springel, 2000; Barnes, 2004; Cox et al., 2006b). Measurement of the encounter parameters from morphology and kinematics of tidal tails can be compared with the encounter parameters inferred from star formation history, and if both constraints are strong enough, they can be used to put independent constraints on sub-grid models of star formation in hydrodynamical simulations.

Encounter parameters of the galaxy merger also affect the angular properties of the remnant. We discussed in §1.1.2 that major disk-disk galaxy mergers are candidates for making early-type galaxies (ETGs). But, it has been shown that photometric and rotational properties of most massive ellipticals are not simply reproduced by randomly oriented disk galaxy mergers (Burkert et al., 2008). While multiple mergers may explain the properties of these galaxies (Boylan-Kolchin et al., 2005; Robertson et al., 2006), it has been shown that the initial orientation of disks of merging galaxies along with their gas fraction affect the of angular momentum left in their remnants (Bois et al., 2011; Naab et al., 2014).[14] Initial orientation of disks strongly affect the morphology and kinematics of tidal features in the early stages of the encounter. So, tidal morphology can be used to predicts the rotational properties of the remnant. One can compare these properties with integral field unit (IFU) observations of early-type galaxies (ETGs), putting new constraints on the models (Cappellari et al., 2011; Emsellem et al., 2011; Krajnović et al., 2011; Bois et al., 2011; Naab et al., 2014).

For some of the dark matter cosmological simulations, the distribution of orbital parameters of the dark matter halo mergers have been predicted (e.g. Benson 2005; Khochfar & Burkert 2006). This is done by finding the merged halos in the simulations, and then stepping back in time and calculating the orbital parameters of the halos that were going to merge. If we assume that the galaxies follow the dark matter halos, this distribution should be similar to distribution of orbital parameters

---

[14] In massive galaxies AGN feedback is likely to also significantly affect the angular momentum, yet its effect is not yet well constrained (Narayanan et al., 2008).

in the galaxy mergers. Direct observational measurement of these distributions do not exist. Measuring the encounter parameters for a statistically significant sample of nearby galaxy mergers would make it possible to put a new constraints on our cosmology. This is a tedious task, though ongoing and future IFU galaxy surveys provide resolved kinematics of galaxies, including a significant number of interacting pairs, providing the required kinematic data for approaching this problem in near future. (CALIFA: Sánchez et al. 2012, MaNGA: Bundy et al. 2015, SAMI: Croom et al. 2012, HECTOR)

1.3.2 Modeling the Dynamics of the Tidal Features

Assuming that the galaxies have the same or self-similar internal structure, there are sixteen parameters that can describe the encounter of a pair of interacting galaxies. Barnes & Hibbard (2009) classifies these parameters into three groups. First, are the Keplerian orbital parameters that describe the orbit of two point masses. The galaxies are not point masses, but we can describe their orbits with Keplerian orbital parameters at the beginning of the encounter when they are far enough. These parameters include eccentricity, pericentric distance, and mass ratio (3 parameters). Second are the parameters that describe the initial orientation of the discs, whether they are prograde, retrograde, or polar (2 parameters for each disk, total of 4 parameters).

The third group of parameters are the ones that depend on the time and location of the observer. They include, viewing angle (3 parameters), time at which we observe the system (1 parameter), and the physical and velocity scales and position of the system (5 parameters).

All of these parameters affect the morphology and kinematics of tidal features significantly. According to Equation 1.1 the mass of the companion is proportional to the amount of tidal acceleration that galaxies experience. So, mass ratio affects the shape of the tidal features. Eccentricity and pericentric distance change the velocity and distance of the galaxies at the first pericenter, respectively. Close encounter induces larger tides in both galaxies and fast encounter shortens the time of the tidal impulse. We also mentioned in §1.2.2 that disk orientation affects the strength and morphology of tidal features. These features grow initially with time after the first passage, and they may re-accrete on the disks at later times. Their shape depends on the time and viewing angle of the observer.

The strong dependence of the tidal configuration on the encounter parameters between the first and the second passage have made them a common tool for measuring these parameters. Assuming that the mass profile of the individual galaxies do not affect the tidal feature to a large extent[15], one can look for a snapshot of a disk-disk galaxy merger simulation that from a certain viewpoint, resembles the tidal morphol-

---

[15] This assumption is certainly not completely true. As discussed earlier, it has been shown that when the potential well of the dark matter halo is deep enough, it will not allow long lasting tidal tails to form (Springel & White, 1999). Barnes (2016) showed that the amount of luminous material in bulges and disks of merging galaxies significantly affect the tidal configuration during the merger.

ogy and kinematics of the observed system. This is called “dynamical modeling” of interacting galaxies.

Toomre & Toomre (1972) used only the morphology of tidal features to model the dynamics of a small sample of galaxy mergers, however they were cautious to confirm that the velocity of the center of the two galaxies qualitatively match with the center of mass velocity of their model galaxies. There has been other attempts to model the dynamics of galaxy mergers without using the kinematic information (Borne & Richstone, 1991; Shamir et al., 2013). Recently, Holincheck et al. (2016), as part of the *Galaxy Zoo* project, explored $\approx 10^5$ points in the parameter space of an impressive sample of 62 galaxy mergers, using the judgement of citizen scientists to evaluate the quality of the match between the morphology of the data and the simulation. The optical morphology of galaxies shows the distribution of stars, and is available for a large number of galaxies from photometric all sky surveys like Sloan Digital Sky Survey (SDSS) (York et al., 2000). Large Synoptic Survey Telescope (LSST) (Collaboration et al., 2009), in near future, will provide an even deeper image of the nearby galaxy mergers, revealing fainter tidal tails for larger samples.

Kinematic information over the tidal tails, however, seem to be necessary to break the degeneracies in encounter parameters. Borne & Richstone (1991) matched their model of NGC 7252 to the morphology and rotation curves along the major and minor axis of the inner gas disk. Later HI observations by Hibbard & van Gorkom (1996a) showed that their model provide the wrong sign for velocity gradient along the tails (Hibbard et al., 1994; Hibbard & Mihos, 1995). The uncertainties of the encounter parameters provided by Holincheck et al. (2016) are quite large which is partly because of using only the morphological constriants and no line of sight velocity information.

In order to measure the line of sight velocity, different kinematics tracers may be used. Cold neutral gas emitting the HI 21 cm emission line is a great candidate for measuring kinematics in tidal tails. The HI gas is usually more extended than stars in disk galaxies. As a result of interaction, usually larger fraction of cold gas is left in tidal tails and bridges compared to stars (Hibbard et al., 1994). However, measuring kinematics of cold gas in nearby merging galaxies like the Mice galaxies is relatively expensive. One needs high enough spatial resolution to be able to capture the velocity gradient across the tails. This is only possible with large interferometers such as Jansky Very Large Array (JVLA) in wide configuration (Hibbard & van Gorkom, 1996a). The other challenge with HI velocity field is that if the interaction geometry involves direct collision of ISM of the two disks[16], it is hard to model the details of dissipation in the model. (e.g. see Condon et al. 1993).

Kinematics of stars are ideal if one is to model the interaction with collisionless particles. In many cases, using collisionless N-body simulations is necessary to make exploration of large parts of the encounter parameter space possible, because treating the physics of dissipation in the gas makes the simulations computationally more

---

[16] in retrograde and polar close encounters

expensive. As stars are also collisionless, their phase space distribution is most similar to collisionless particles in N-body simulations, especially in polar and retrograde close encounters where gas suffers a lot of dissipation. Stars, however, are not as extended as cold gas in most spirals, and the tidal features they make in interaction are weaker. In addition, measuring the kinematics of stars requires spectroscopy with high signal to noise continuum level, so one can detect and measure the stellar absorption lines. As stellar tidal tails are usually faint, measuring their stellar velocity requires long exposure times.

Another option for measuring kinematics is looking for nebular emission lines from star forming regions also known as HII region. Disk galaxies usually host star forming regions. As discussed earlier star formation is enhanced not only in the center of interacting galaxies but also in the outskirts due to tidal shock heating of neutral gas that over-pressurize the molecular clouds, making them gravitationally unstable and forming stars (Jog & Solomon, 1992; Barnes, 2004). Merger-induced star formation has been detected in faint tidal tails of nearby interacting galaxies (Whitmore & Schweizer, 1995; de Grijs et al., 2003; Hibbard et al., 2005). The Hα emission from the star forming regions is relatively easy to measure as it requires less exposure time compared to stellar kinematics. Though, Hα displays the same dissipations that one finds in HI gas, and may not be a good choice in retrograde and polar orbits. In addition, Hα may originate from gas ionized from sources different from normal star formation. Shock-heating and hard X-ray from AGN can also ionize the gas. These extreme processes affect the velocity of ionized gas in a way that can not be described by gravitational forces any more. Tidal features in simulations are gravitational effects, and do not reproduce the kinematics of shock-heated gas. One must be careful to separate Hα of star forming regions from that of other sources of ionization if they are to use Hα -derived velocity for dynamical modeling. In Chapter 3 we measure the Hα kinematics of the Mice galaxies. We separate HII regions from shock-heated gas using properties of emission lines. We compare dynamical model of the Mice galaxies using our Hα and archival HI kinematics and show that Hα can be used instead of HI for this purpose.

1.3.3 Attempts to Measure Initial Conditions of Interacting Disks

Toomre & Toomre (1972) presented models of four systems of galaxy mergers for the first time: Arp 295, M 51 (the Whirlpool galaxy), NGC 4676 (the Mice galaxies), and NGC 4038/9 (The Antenna galaxy). Their simple model consisted of a central point mass and test particles of the disk in circular orbits. Though, they were successful in reproducing overall optical morphology of the tidal tails. All but Arp 295 have been revisited several times in future works using more complicated mass models for individual galaxies, but the overall findings of Toomre & Toomre (1972) have been confirmed.

There has been many attempts to model galaxy mergers with strong tidal features in nearby Universe. Barnes & Hibbard (2009) provide a good summary of the systems that had been modeled before 2009. (See Table 2 in Barnes & Hibbard 2009) Early works were more focused on matching the optical morphology. Later with the emergence of HI interferometric observations and Fabry-Perot Hα velocity maps, kinematics gained a more substantial role. Though, the application of kinematic information has been different in different works. Some only qualitatively check the consistency of their models with the velocity or rotation curves near the center of light (e,g. Borne & Richstone 1991). Others have made a more quantitative approach using 1D or 2D kinematic information (e.g. Duc et al. 2000). The most successful models confirm the similarity of the model and data by over-plotting their model on the data, or by plotting them aside on the same scale and orientation (e.g. Hibbard & Mihos 1995).

Barnes & Hibbard (2009) developed a software package named "Identikit" in which they combine test particle techniques with self-consistent simulations for rapid exploration of encounter parameter space in equal mass mergers. Their model consists of massive particles reproducing the potential of halo, disk, and bulge, along with massless test particles in circular orbits representing the disks. It provides an interactive interface in which the user can change parameters like viewing angle, disk orientation, time since pericenter, and pericentric separation, and view the effect on the morphology and kinematics of the tidal feature in the model over-plotted on data. Their representation of morphology and kinematics is similar to Hibbard & Mihos (1995). Privon et al. (2013) used Identikit to put constraints on the encounter parameters of four merger systems, NGC 5257/58, NGC 4676 (the Mice), NGC 5194/95 (Antenna), and NGC 2623. They followed up their Identikit best-fit models with fully self-consistent simulations to confirm that the self gravity of the disk particles do not significantly affect the large scale tidal features and the rate of orbital decay.

The uniqueness of encounter parameters that lead to a model similar to data is an important concern. The 16 encounter parameters mentioned here are all physically motivated. On the other hand, one may be skeptical of a model with so many free parameters.[17] However, one should remember that the nature of model and data is important. For example, models of stellar absorption lines have up to ~ 90 abundance parameters, yet few argue that the answer is unique. In case of dynamical modeling of galaxy mergers, tidal features break many of degeneracies, when they are strong enough. The most confident (and maybe the least smart) way to show that a set of encounter parameters leading to a good match is unique, is to visually scan the whole parameter space and reject all other possible models. This is obviously not possible unless through a citizen science project similar to *Galaxy Zoo: Mergers* (Holincheck et al., 2016), or by automating dynamical modeling.

There have been some attempts to automate the process of dynamical modeling.

---

[17] John von Neumann says: “with four parameters I can fit an elephant and with five I can make him wiggle his trunk” (Dyson 2004, p297). Barnes & Hibbard (2009) continue: “John von Neumann could presumably fit a whole herd of elephants with the parameters used to describe a single galactic encounter.”

In all of them, the subjective comparison between the simulation particles ($\mathcal{P}$) and observed data ($\mathcal{D}$) is replaced by an objective criterion $\mathcal{F}(\mathcal{P},\mathcal{D})$ measuring the goodness of the fit. In some of these methods "genetic algorithms" have been used to efficiently search a subset of the huge parameter space and find the best model (Wahde, 1998; Theis & Harfst, 2000; Smith et al., 2010). In most of previous works $\mathcal{F}(\mathcal{P},\mathcal{D})$ is obtained from comparison between images of the model and data smoothed with the same smoothing kernel. Barnes (2011) provides a new quantity called "score" as the measure of the goodness of the fit. Score is calculated after the user puts phase space boxes on tidal features of the merging system. The software package calculates the score based on the number of model particles that populate these phase-space boxes. He also combines test-particles techniques with self-consistent simulations to reduce the time required to explore various disk spins. In Chapter 2, we use this software package to develop a new automated pipeline for modeling equal-mass galaxy merges. We use bootstrap sampling of the phase-space boxes to find the uncertainty of the measured parameters. We test our pipeline against an independent set of hydrodynamical simulations with know initial conditions to find the systematics of measured encounter parameters.

1.4 Summary

In this thesis we study the encounter parameters of interacting galaxy pairs and investigate the properties of star forming and shocked gas in galaxies at different merger stages.

In Chapter 2 we develop a new automated method for modeling the dynamics of galaxy mergers between the first and the second passages. We test the validity of the measured encounter parameters by applying our method on an independent set of hydrodynamical galaxy merger simulations that incorporates the more complicated physics of gas and stars. In Chapter 2 we are planning to address these questions: Is it possible to automate the dynamical modeling of galaxy mergers? Visual matching is subjective and does not provide well-defined error bars. How can we calculate the uncertainties of the measured encounter parameters? Are test particle simulations successful in reproducing tidal features of galaxy mergers?

In Chapter 3 we investigate the effect of using different kinematic tracers on modeling the dynamics of the Mice galaxies (NGC 4676). We measure the Hα kinematics of this system using optical IFU observations with spectral resolution R$\approx$ 4000. We fit multiple velocity components to emission lines, and separate the emission from shocked and star forming gas. In this Chapter we hope to find the answer to these questions: Can we separate Hα emission from star forming regions and Hα emission from shock-heated gas? Does measuring the fraction of Hα from shocked gas improve measurements of star formation rate for the Mice? Do HI and star forming Hα velocity maps agree? Are the results of dynamical modeling of the Mice galaxies consistent when we use HI and Hα kinematics? Can we use our dynamical model to put independent constraints on models of merger induced star formation in hydrodynamical simulations?

In Chapter 4 we observe a sample of 22 galaxy mergers, consisting of 19 relatively early stage pairs, and 3 coalesced mergers, using SparsePak IFU on the WIYN telescope at KPNO. The separate pairs have characteristics similar to that of the Mice galaxies: strong tidal features and separate nuclei. They have mass (light) ratios between 1:1 to 1:8. We treat the emission lines with the same method as in Chapter 3. With Hα velocity maps we try to put new constraints on the encounter parameters of the equal mass systems. For the rest of them, we investigate the spatial distribution of shocked components and discuss possible sources of shocks. We try to address these questions in Chapter 4: Can we learn about the distribution of encounter parameters from modeling the systems in this Chapter? What is the dominant process that ionize gas at merger stages covered by our sample? Can we learn about possible role of mergers in quenching star formation in galaxies?

Chapter 2

Modeling the Initial Conditions of Interacting Galaxy Pairs Using Identikit

We develop and test an automated technique to model the dynamics of interacting galaxy pairs. We use Identikit (Barnes & Hibbard 2009; Barnes 2011) as a tool for modeling and matching the morphology and kinematics of the interacting pairs of equal-mass galaxies. In order to reduce the effect of subjective human judgement, we automate the selection of phase-space regions used to match simulations to data, and we explore how selection of these regions affects the random uncertainties of parameters in the best-fit model. In this work, we use an independent set of GADGET SPH simulations as input data to determine the systematic bias in the measured encounter parameters based on the known initial conditions of these simulations. We test both cold gas and young stellar components in the GADGET simulations to explore the effect of choosing HI vs. Hα as the line of sight velocity tracer. We find that we can group the results into tests with good, fair, and poor convergence based on the distribution of parameters of models close to the best-fit model. For tests with good and fair convergence, we rule out large fractions of parameter space and recover merger stage, eccentricity, pericentric distance, viewing angle, and initial disk orientations within 3σ of the correct value. All of tests on prograde-prograde systems have either good or fair convergence. The results of tests on edge-on disks are less biased than face-on tests. Retrograde and polar systems do not converge and may require constraints from regions other than the tidal tails and bridges.

2.1 Introduction

The merger of galaxies and their associated dark matter halos is a fundamental process in galaxy evolution and cosmology. Galaxies and the dark matter halos they live in grow in time through mergers and accretion from the cosmic web. Over the past 8 billion years massive galaxies have transformed from star-forming disk galaxies into inactive bulge-dominated ones (e.g. Bell et al. 2004; Faber et al. 2007). Galaxy mergers may be an important process that drives the assembly of galaxies, rapid star formation at early times, and the formation of bulge-dominated galaxies (e.g. Toomre

& Toomre 1972; Mihos & Hernquist 1996; Barnes & Hernquist 1996).

Direct measurements of the initial orbital conditions of colliding galaxies are useful constraints for cosmology and galaxy evolution. Cosmological dark matter simulations predict hierarchical gravitational growth of structure with time. Numerical simulations predict the distribution of orbital parameters of dark matter halo mergers (e.g. Benson 2005; and Khochfar & Burkert 2006). If galaxies follow the dark matter halos, direct measurement of orbital parameters in galaxy mergers will put constraints on these simulations. In addition, idealized and cosmological zoom-in galaxy merger simulations have shown that merger induced star-formation history may depend on the initial orbital parameters of the interacting pair. (e.g. Cox et al. 2008; Snyder et al. 2011).

Moreover, integral field spectroscopy of nearby elliptical galaxies have shown that early-type galaxies in local universe can be categorized into fast and slow rotators (Cappellari et al. 2011; Krajnović et al. 2011; Emsellem et al. 2011). Recent results have shown that initial orbital parameters of major galaxy mergers can affect the rotational properties of their bulge-dominated remnants (e.g. see Hopkins et al. 2009, Bois et al. 2011, Naab et al. 2014). Measuring these orbital parameters in early-stage mergers will make it possible to predict the kinematic properties of the merger remnant.

Constraining the initial conditions of a pair of interacting galaxies can be accomplished by finding a simulation reproducing both the morphology and kinematics of the data. (e.g. Toomre & Toomre 1972; White 1978; Barnes 1988). While some efforts have been made to model interacting galaxies by matching only the morphology (Toomre & Toomre 1972; Shamir et al. 2013), line of sight velocity data is required to find unique dynamical models for many interacting systems (Barnes & Hibbard 2009). For example, the best-fit dynamical model for NGC 7252 (Borne & Richstone 1991) changed significantly when high quality HI kinematics data became available (Hibbard et al. 1994; Hibbard & Mihos 1995).

Barnes & Hibbard (2009) provides a review of the dynamical modeling of the interacting disk galaxies which have made use of kinematic information. These attempts have used different amounts of kinematic data; some have tried to match 2D kinematics obtained from HI or Hα maps (e.g. Hibbard & Mihos 1995; Duc et al. 2000; Struck et al. 2005), while others have only used 1D kinematics from long-slit spectroscopy (e.g. Mihos et al. 1993; Díaz et al. 2000; Scharwächter et al. (2004)). Most of these attempts rely on human expert judgment about the model that best matches the data. There has been some attempts to automate the matching process using genetic algorithms (e.g. Theis & Kohle 2001; Wahde & Donner 2001;Theis & Spinneker 2003). These algorithms have not yet matured enough to replace visual matching.

More kinematics information for modeling the dynamics of galaxy mergers will become available in near future with optical IFU and radio surveys providing large amounts of 2D line of sight velocity data for nearby galaxies. CALIFA (Sánchez et al.

2012), SAMI (Croom et al. (2012)), and MaNGA (Bundy et al. 2015) are ongoing surveys of optical 2D spectroscopy of nearby galaxies including large numbers of interacting galaxy pairs. In addition, Australian SKA Pathfinder (Johnston et al. 2008) and MeerKAT (Booth et al. (2009)) will perform high resolution HI surveys of nearby universe. Thus, we need to develop robust tools to classify interacting galaxies based on this data.

Identikit is a tool for modeling major galaxy mergers (Barnes & Hibbard 2009; Barnes 2011). It combines self-consistent and test particle techniques in order to utilize fast exploration of the parameter space of a disk-disk encounter. With Identikit 1 (Barnes & Hibbard 2009), the user can interactively change parameters like viewing direction and the orientation of the two disks until the best visual match between model and data is found. This interactive interface has been used for dynamical modeling of some major galaxy mergers (Privon et al. 2013). The visual match, though, is subjective and depends on user's judgment about the most similar model. It requires a great deal of human-expert time spent on exploring the parameter space and looking for the best match. More importantly, the uncertainty in the initial conditions measured with Identikit 1 is not determined. Identikit 2, however, defines a quantity called "score" that provides an informal measure for the quality of the match. As a result, we can automatically search the parameter space and find the model with the maximum score, i.e. the best-fit model.

In this Chapter, we developed an automated routine based on Identikit 2. Our goal is to test the random and systematic uncertainties of modeling a major galaxy merger system using our method. In order to measure the systematics of Identikit modeling, we used GADGET SPH simulations (Cox et al. 2006b; Cox et al. 2008) as input data. Because the initial conditions of the GADGET simulations are known, we can measure the biases in the parameters of the best-fit model. We test both cold gas and young stars in the the GADGET simulations to compare the effect of using HI vs. Hα as the kinematics tracer. Through a statistical approach, we also measure the random uncertainty of the best-fit model. In §2.2 and §2.3 we describe the methodology and the hydrodynamical simulations we use in this work. In §2.4 and §2.5 we present the results and discussion, respectively.

2.2 Method

2.2.1 Identikit

Identikit (Barnes & Hibbard 2009 and Barnes 2011) matches simulated disk-disk galaxy encounters to the observed morphology and kinematics of disk-disk galaxy mergers. Assuming a particular mass model for the isolated galaxies (see §2.3.2), there are 3 groups of parameters describing the encounter of two disk galaxies. First are the orbit parameters, including eccentricity, pericentric distance, and mass ratio. Second are the parameters that describe the initial angular momenta of disks. The last group contains the parameters that depend on the observer's time and location.The

Parameter Class	Parameter	Range Tested
orbital parameters	eccentricity(1)	[0.80-1.10]
	pericentric distance(1)	[0.03125-1.0000]$\times R_{vir}$
	mass ratio (1)	1
observer dependent parameters	time since pericenter(1)	from first pass to second pass
	viewing angle(2)	found through maximizing score in Identikit 2
	position(2)	set by locking the centers
	length scaling $\mathcal{L}$(1)	set by viewing angle and locking the centers
	velocity offset(1)	0
	velocity scaling $\mathcal{V}$(1)	[-0.500-+0.500]*
initial orientation of disks	(4)	found through maximizing score in Identikit 2

Table 2.1: List of Identikit parameters for a system of interacting galaxies. Barnes (2011) categorized these parameter into 3 classes. The number of degrees of freedom in each parameter is shown in the parentheses. As diskussed in the text, we test 4 of these parameters, eccentricity, pericentric distance, time since pericenter, and velocity scaling. For every Identikit model and for each value of velocity scaling Identikit 2 finds the best viewing angle and the best initial disk orientations by maximizing score. The rest of the parameters can by estimated from direct observations, independent of modeling. * The velocity scaling $\mathcal{V}$ relates the dimensionless velocity in Identikit to the physical velocity. If V_{range} is the velocity range in the Identikit velocity panels (top right and bottom left panels in Figure 2.1), the physical scale of unit velocity in Identikit, V_{phy}, is $V_{range}/(4 \times 10^{\mathcal{V}})$.

third group includes the viewing direction and the time of the merger as well as the parameters transforming the model to the physical scales of the real system (i.e. length/velocity scaling, and length/velocity offset). All of these make up dynamical parameters involved in a disk-disk galaxy interaction. We list these parameters in Table 2.1.

The isolated galaxies consist of massive self-consistent and massless test particles with no dissipative (gaseous) component. Each galaxy contains 81,920 massive particles and 262,144 massless test particles.The massive particles are distributed in a spherically symmetric fashion to represent the potential of a massive dark matter halo, a disk, and a bulge. The massless test particles, on the other hand, are distributed in disks with circular orbits. The motion of test particles is governed by the gravitational potential produced by massive particles. However, because they are massless, one may simulate test particles for multiple disks with different orientations simultaneously, without having them affect each other. As a result, one can calculate the trajectories of all possible disk particles in a single simulation run. In one run, the user obtains the morphology and kinematics of merger systems with disks of all different initial orientations. When comparing simulations to data, at each time step of the simulation, the user can turn on a particular disk and turn off the rest. Thus, Identikit quickly explores the parameter space in search for the best model.

Identikit can model the large scale morphology and kinematics of the tidal tails with a unique set of initial conditions. Early simulations of disk-disk galaxy mergers show that the shape and size of the tidal tails are sensitive to the initial conditions of the encounter (Toomre & Toomre 1972; Hibbard & Mihos 1995). These features move ballistically after the first passage and carry a memory of the initial conditions, and it's been shown that there is little difference in the shape of tidal features in test-particle vs. self-consistent simulations of interacting galaxy pairs (Dubinski et al. 1999). On the other hand, self-gravitating features (e.g. the spiral arms, stellar clusters) should not be matched when using a test-particle model like Identikit.

While Identikit 1 (Barnes & Hibbard 2009) identifies the best model interactively and qualitatively, Identikit 2 (Barnes 2011) introduces a score that quantifies the agreement between the model and the data. The score is calculated using user-input boxes which indicate regions of phase space and are extended in X, Y (morphology), and V (line of sight velocity) directions. As is shown in Figure 2.1, boxes are put on the tidal tails and bridges of the merger system. Identikit 2 calculates the scores based on the number of test particles populating these boxes. The score is assumed to be higher for the models that better reproduce the chosen phase-space boxes. Identikit 2 then scans viewing directions and initial disk orientations, calculating the score for each direction/orientation. The best orientation and viewing angles are the ones that give maximum score for a particular set of parameters.

The primary advantage of Identikit's test particle technique is rapid scanning of the multidimensional parameter space. Moreover, Identikit 2 quantifies the quality of the match, which is a unique feature. While visual matching is time consuming and

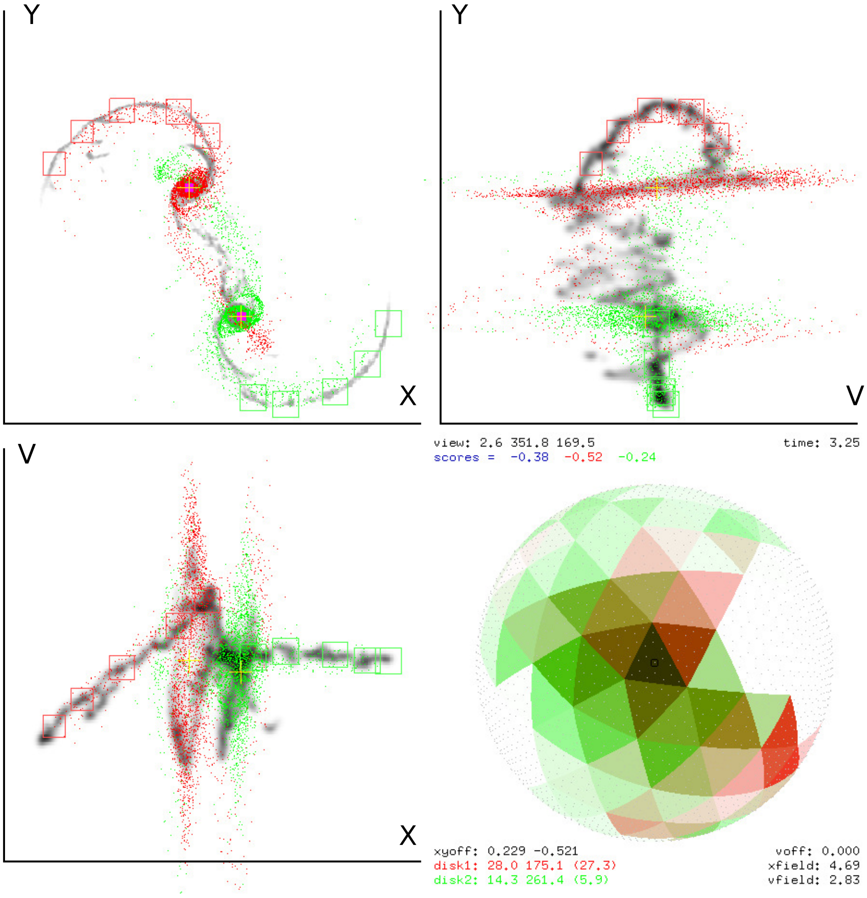

Figure 2.1: Identikit model fit to a GADGET simulated data. The top left panels show the morphology, the bottom left and top right panels show the LOS velocity-position. The GADGET cold gas is shaded grey, and the best-fit Identikit galaxy models are the red and green points. Identikit uses the phase-space regions selected on the tidal tails (red and green boxes) to calculate the quality of the fit for each disk as functions of different viewing directions. Identikit calculates these functions at 320 viewing angles. The bottom right panel shows these functions as green and red shades on a spherical lattice. The best viewing direction is where the product of these functions are maximum.

subjective, providing a quantity (score) for the goodness of the fit is quantitative and requires less human expert time. However, massless test particles cannot reproduce self-gravitating features (e.g. spiral arms), and one cannot expect the dissipative features in gaseous components to be recovered. Tidal features are the key to recover a reasonable model. In some interacting galaxies such as retrograde ones, the tidal features are weak, and therefore they are more difficult to model. Besides, score does not have an absolute significance like χ^2. It is only useful for comparing quality of fit with the same set of boxes and cannot be used independently to determine the likelihood of the fit.

We create a library of Identikit models consisting of different time steps of simulations of galaxy mergers with varying orbital parameters. Each member of this library is an individual frame with four fixed encounter parameters which we call external parameters (time, eccentricity, pericentric distance, and mass ratio). The user can study each member of the library in an interactive interface and explore other parameters of interest which include viewing direction, initial orientation of disks, length and velocity offsets, and length and velocity scalings. We call these internal parameters. Identikit 2 measures the score after the user locks the centers of model galaxies on the sky positions of the centers of the observed interacting galaxies. This constrains the position (length offset) and makes the viewing angle determine the length scaling $\mathcal{L}$ due to projection effect. So, locking the centers constrains two of the internal parameters. Identikit explores the viewing direction and the initial orientation of disks and finds the configuration that maximizes the score. So, for each member of the Identikit library at a particular velocity scaling and velocity offset, Identikit calculates a score.

In this work, merger systems consisting of two separate galaxies with distinct cores and strong tidal tails are examined. Identikit 2 can only be used to model separate galaxies. Additionally, by selecting galaxies which have not yet coalesced, we can independently estimate the mass ratio based on the measured light ratio. In this paper, we only study equal mass galaxy mergers. Additionally, tidal features are strongest during the time range between the first and the second passage. So, we restrict the current study to this time range. It may be possible to estimate a prior value for the velocity offset $\mathcal{V}$ by measuring the light-(mass-)weighted average (systemic) velocity of the merger system. Locking the centers constrains position and length scaling. As a result, ignoring the freedom in choosing the mass model in isolated galaxies, we have six more encounter parameters to explore: eccentricity, pericentric distance, time (between the first and second passage), viewing angle, orientation of disks, and velocity scaling.

Of the remaining internal parameters, viewing angle and orientation of disks are determined when we maximize score for each member of the library; however, velocity scaling is a free parameter. We can find the best score for each member of Identikit library with a fixed velocity scaling. So, we calculate score for models with a grid of parameter values for eccentricity, pericentric distance, time since pericenter, and velocity scaling. Initial orientation of disks and viewing angle (and therefore length scaling $\mathcal{L}$) are determined independently when we calculate the score for each of these models. Table 2.1 shows the list of all parameters involved in Identikit and the range of the four parameters that are systematically explored in this work.

For an interacting system (i.e. a GADGET simulation in this work), one can make the map of scores of Identikit models with varying encounter parameters. In order to make such a map, we select a set of boxes on tides and bridges of the interacting system. Keeping the selected boxes fixed in place, we match all models in the Identikit library. For each member we change the velocity scaling as a free parameter and record how the score changes. Eventually, we obtain a score for all Identikit models with different eccentricity, pericentric distance, time, and velocity scaling. This makes an 4+1 dimensional scalar field. The model with the maximum score is the best-fit model. However, we still need to know how significant is the maximum score we found.

We perform a statistical evaluation to measure the uncertainty of the score for each Identikit model. We select the same number of boxes on the same tides and bridges but at slightly randomized positions. With the new set of boxes we calculate scores for all Identikit models again obtaining a new 4+1 dimensional score map. The new score map will have slightly different scores at each point in the parameter space. We repeat to make multiple score maps, each by moving the boxes around the tides and bridges of the interacting system. We calculate the average and the standard deviation of the scores at each point in parameter space. Figure 2.3 shows a 2+1 dimensional slice of an average score map. Each cross represents an Identikit model with a particular set of parameters. The cyan box in Figure 2.3 shows the best-fit model with the highest average score, and the red circle shows the input GADGET parameters. The contours show the models with scores that are within 1, 2, 3, and 4 standard deviation of the scores of the best-fit model. We calculate the uncertainty in the best-fit parameters from these contours.

2.2.2 Box Selection

Even though Identikit 2 reduces the human subjective influence in finding the best match, it still depends on selection of box positions. If we move the boxes in X, Y , or V directions, or change their size or number, we select different regions of phase space. As a result, test particles populate them differently, leading to different scores. In Identikit one positions these boxes manually using an interactive interface. In order to explore the effect of box-selection and also to reduce the human interference, we developed a simple semi-automated routine for box selection. In this routine, boxes are selected akin prescribed user-selection in Identikit. Figure 2.2 describes our semi-automated routine.

Our automated box selection routine places the boxes on the tidal features and the bridges of the merger system. The algorithm attempts to place the boxes in the same style as they are placed manually in Barnes (2011). In this routine, first the

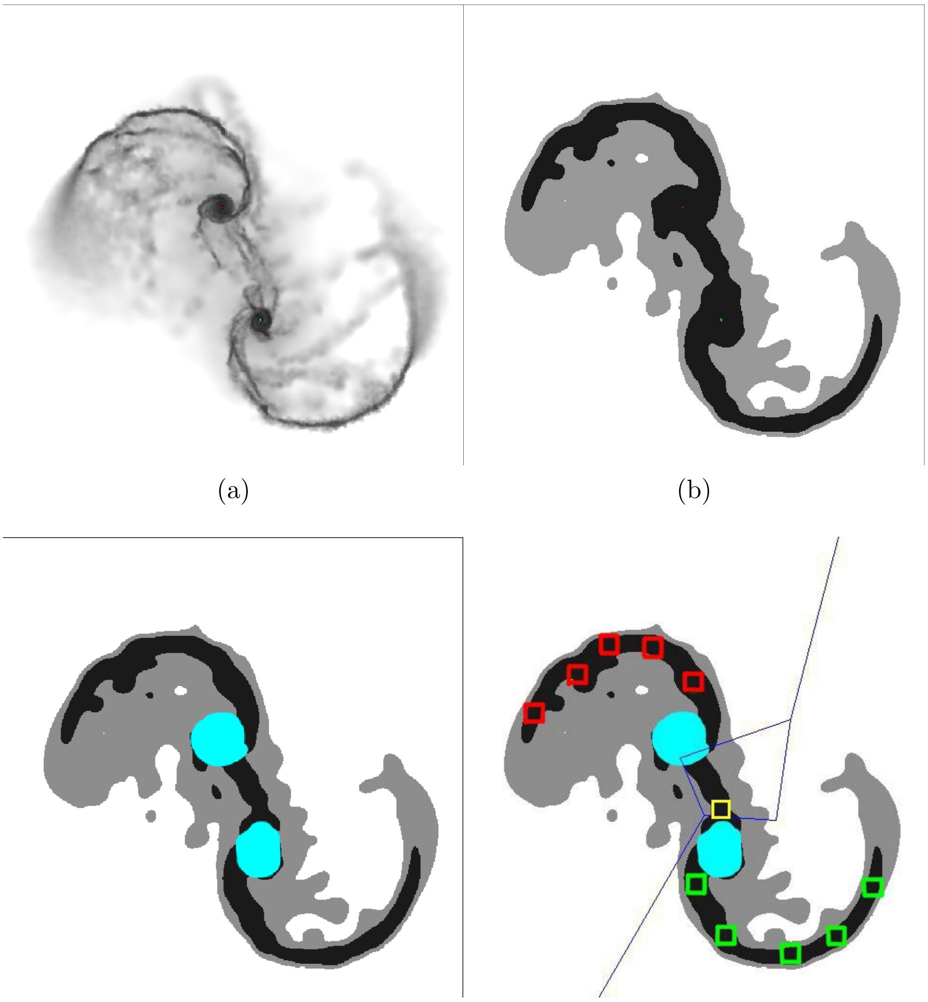

(a) (b)

(c) (d)

Figure 2.2: Semi-automated box selection procedure: (a) Cold gas in a GADGET galaxy merger simulation (the fiducial model in test 1, see Table 2.3.2). (b) segmentation map for two surface brightness levels. (c) The centers of the two galaxies are masked by the user to avoid selecting boxes in these regions. (d) We select 11 random points (boxes) in the remaining black region. The blue lines divide the regions for disk 1- (red), disk 2- (green), and the overlap (yellow) boxes.

segmentation maps of the system with different surface brightness levels are made. The surface brightness levels are manually adjusted to include faint tidal features in the segmentation map. In the next step, the user manually masks the central regions of the galaxies within the segmentation map, where he/she wants to avoid putting boxes. As explained earlier, Identikit reproduces the large scale tidal tails of the interacting galaxies but not the self-gravitating details. Boxes must not cover the centers of the galaxies. Finally, a user-defined number of boxes are randomly placed in the remaining regions of the segmentation map (Figure 2.2). The velocity of these boxes are determined by calculating the mass-(light-)averaged velocity of the cold gas (stars) inside the box. While there is still human influence in this routine (i.e. adjusting the surface brightness limit for segmentation map and masking the centers of galaxies), it is more automated than the original process in Identikit 2 and can be used for exploring the random effects of box selection. It should be mentioned that this routine only selects boxes of the same size, but Barnes (2011) often uses varying box sizes.

We have chosen the size of the boxes to be comparable to the spatial resolution of the data available. Here, we assume that the GADGET simulated galaxies are at the same distance as typical nearby major merger systems (e.g. the Mice galaxies). The HI data of nearby interacting galaxies have been obtained using VLA D and C arrays (e.g. Hibbard & van Gorkom 1996b). The typical angular resolution of these observations is $\sim$ 20" $-$ 30" which is equivalent to $\sim 8 - 12$ kpc. For GADGET

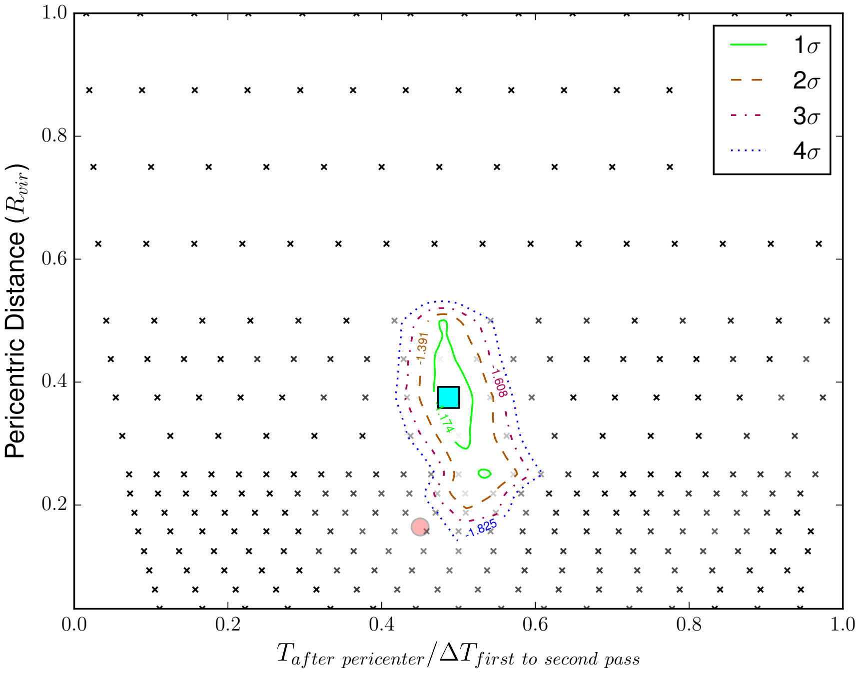

Figure 2.3: The average score map of Identikit models matching Sbc201a (test 01). Each cross represents an Identikit model for which the score is calculated several times by moving the boxes (see §2.2.2). The average and standard deviation of the scores are calculated. The model with the highest average score is shown with the cyan box. The counters enclose the models with scores within 1, 2, 3, and 4 times the standard deviation of the best-fit model. The crosses are also color coded with light gray showing higher scores and dark gray showing lower scores. Notice that this figure shows a 2D slice of the score map showing scores for models with varying time and pericentric distance but fixed eccentricity (=1.0) and velocity scaling (-0.1). The red circle shows the known correct answer for the GADGET simulation.

simulations of cold gas, we select the size of the boxes to be $\sim 6 - 8$ kpc. The optical Hα kinematics data obtained by many current instruments usually have a higher resolution. For instance, the diameter of the fibers in SparsePak on the WIYN telescope is $\sim$ 6", equivalent to $\sim$ 3 kpc on a system like the Mice (Bershady et al. 2004). So, when testing the young stars in our simulations, we selected the boxes to be $\sim$ 3 kpc.

The number of boxes also affect the scores because we select different phase space regions to be populated. For each test on GADGET simulations described in §2.3, the number of boxes is fixed. We did some testing on the number of boxes needed for each run, and came up with about 10 boxes being the most efficient number of boxes for Identikit score calculation. Wo we kept the number 10 in all tests.

2.2.3 Calculating Uncertainties in Best-Fit Parameters

The uncertainty of the best-fit model is not given by Identikit itself. The results of our initial tests with Identikit showed that positioning the boxes is the largest source of uncertainty in the calculated scores. In order to get a measure of the uncertainty of the scores, we move the boxes over the tidal tails and bridges of the data galaxy multiple times. More precisely, we use the semi-automated routine 10-100 times. Given each set of boxes, we measure scores for all Identikit models. The average

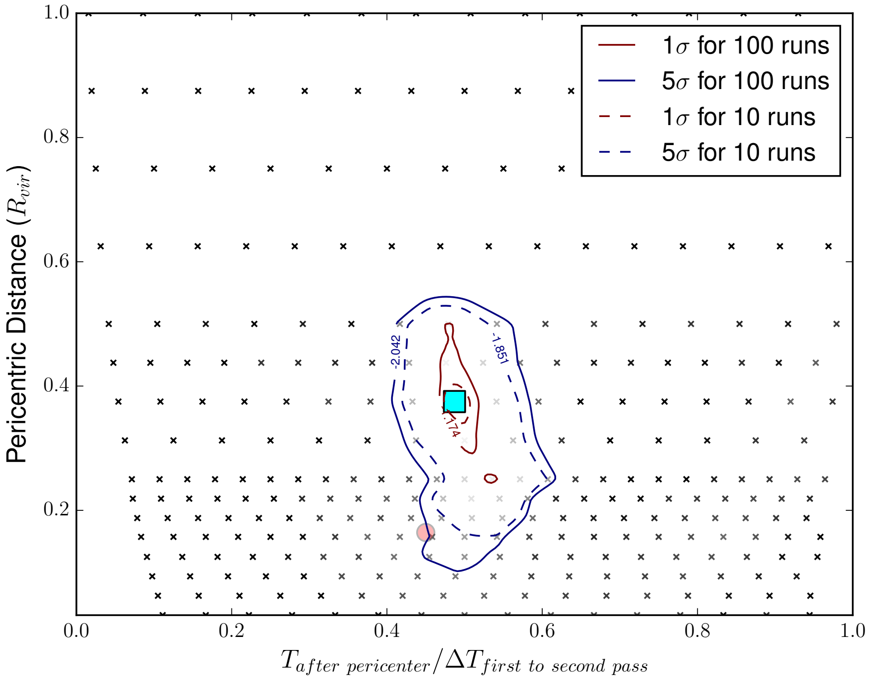

Figure 2.4: The score map with 1σ and 5σ contours obtained via matching the Identikit to the cold gaseous component of the fiducial GADGET simulation. The solid contours are calculated by 100 runs and the dashed contours are calculated by 10 runs. The 1 σ and 5σ contours do not change much by increasing the number of runs by 1 order of magnitude. We see the similar trend for tests on young stars. Throughout this work we calculate scores 10 times for all tests.

and standard deviation of scores at each point in the parameter space is calculated. The model with the maximum average score is the best-fit model, and the models for which the average score is within 1, 2, 3, and 4 standard deviations from that of the best fit model are within 1σ, 2σ, 3σ , and 4σ contours in Figure 2.3, where σ is the standard deviation of scores at the best-fit model.

Because calculating the score for a full grid of models is a computationally expensive, we need to restrict the number of times in which we move the box positions. To determine this number, we track how the 1σ and 5σ level contours change as we increase the number of realization of box positions (runs). We find at what approximate number these contours stop changing significantly with more runs. As can be seen in Figure 2.4, the contours do not change much after 10 runs in these tests. So, we we run all tests 10 times in this work.

2.3 Hydrodynamical Simulations Vs. Identikit

In addition to the random uncertainties described above, we can estimate the systematic biases in the best-fit model using an independent set of hydrodynamical simulations. We use the snapshots of the independent simulated systems as mocked data. Once we find the best-fit model, we can compare its parameters with the correct merger parameters of the simulation.

2.3.1 GADGET Simulations

We use smoothed particle hydrodynamical (SPH) GADGET-2 simulations of equal-mass disk-disk galaxy merger as input data (Cox et al. 2006b and Cox et al. 2008). The isolated galaxies are Sbc type galaxies with stellar and cold gaseous disk components and stellar bulge component, embedded in a massive dark matter halo. Each simulation follows a galaxy merger in a box of $\sim (200\text{kpc})^3$. The spatial resolution is 100 pc, and the particle mass is $\sim 1.0 - 7.1 \times 10^5 M_\odot$. Each galaxy is made of 1,000,000 dark matter particles, 300,000 each of stellar disk and collisional gas, and 100,000 bulge particles, so there is a total 3.4 million particles in each simulation. The snapshots are available in 0.05 Gyr time steps. The simulations include radiative cooling, a density-dependent star formation recipe that reproduce KennicuttSchmidt relation (Kennicutt 1998), and a model to incorporate the effect of supernovae feedback and stellar winds. Even though feedback from active galactic nuclei (Di Matteo et al. 2008) is not included, these simulations capture more physical processes than simple test-particle Identikit models, and they are more realistic.

The mass models of isolated galaxies in GADGET simulations are different from Identikit models. Cox et al. (2006b) and Barnes & Hibbard (2009) describe the mass models of the GADGET simulations and Identikit, respectively. The halo concentration parameter is different between the two models ($c = 11$ in GADGET simulations and $c = 4$ in Identikit). The length scale that is used to match the two simulations is the scale radius of the NFW profile (Navarro et al. 1996). The stellar and gaseous disk scale length in the GADGET simulations are 4 kpc and 12 kpc respectively, which are 0.24 and 0.72 of the scale radius of the halo. In Identikit, isolated galaxies have a disk scale length that is 1/3 of the halo scale radius. We expect to see biases in the initial conditions of the matched simulations as a result of different mass models. However, in real world, the mass models of the interacting galaxies also differ from that of Identikit, and testing Identikit against a simulation with a different mass model helps us better understand the sensitivity of its results on the selected mass model for Identikit.

2.3.2 Model Details

We test Identikit against GADGET simulations described in Table 2.3.2. These models are selected to test the capability of Identikit in modeling systems with varying time since pericenter, viewing angles, eccentricity, pericentric distance, and initial disk orientations. We obtained these simulation via private communication with T.J. Cox, and the distribution of their initial parameters was not designed for the purpose of our tests. The fiducial GADGET simulation used in tests 1-6 is an equal-mass galaxy merger with parabolic orbit. The pericentric distance is equal to 11 kpc. In this simulation, both of the galaxies are prograde. In test 01 and test 02 we look at cold gas and young stars in a face-on snapshot midway between the first and the second passage. In most of other tests, all other parameters but one is similar to tests 01 and 02. We investigate the isolated effect of varying each parameter on the systematic and random uncertainties of the best-fit. We examine cold gas (tests 01, 05, 07, 10, 12, and 14) vs. young stars (tests 02, 06, 08, 11, 13, and 15), merger stage (tests 03 and 04), viewing angle (tests 05 and 06), eccentricity (tests 07, 08, and 09), pericentric distance (test 09), and disk orientation (tests 10-15).

Sim ID	Test ID	component (gas/ young stars)	pericentric distance	eccentricity	prograde vs. retrograde	(i_1, ω_1) (i_2, ω_2)	view (to orbital angular momentum)	time * $\Delta T / T_{\text{first to second pass}}$	number of boxes
Sbc201a	01 (fiducial)	cold gas	$11kpc = 0.1643\ R_{vir}$	1.0	prograde -prograde	$(0, 0)$ $(30, 60)$	face-on	0.45	10
	02	young stars	”	”	”	”	”	”	10
	03	cold gas	”	”	”	”	”	0.25	10
	04	cold gas	”	”	”	”	”	0.75	10
	05	cold gas	”	”	”	”	edge-on	0.45	10
	06	young stars	”	”	”	”	”	”	10
Sbc212	07	cold gas	$11kpc = 0.1643\ R_{vir}$	0.9	prograde -prograde	$(0, 0)$ $(30, 60)$	face-on	0.50	10
	08	young stars	” ”	”	”	”	”	”	10
Sbc214	09	cold gas	$44kpc = 0.6572\ R_{vir}$	0.8	prograde -prograde	$(0, 0)$ $(30, 60)$	face-on	0.50	10

Continued on next page

Table 2.1 – *Continued from previous page*

Sim ID	Test ID	component (gas/ young stars)	pericentric distance	eccentricity	prograde vs. retrograde	(i_1, ω_1) (i_2, ω_2)	view (to orbital angular momentum)	time * $\Delta T / T_{\text{first}}$ to second pass	number of boxes
Sbc207	10	cold gas	$11kpc$ $= 0.1643$ R_{vir}	1.0	polar -prograde	$(270, 0)$ $(30, 60)$	face-on	0.50	10
	11	young stars	”	”	”	”	”	”	10
Sbc203	12	cold gas	$11kpc$ $= 0.1643$ R_{vir}	1.0	retrograde -retrograde	$(180, 0)$ $(210, 60)$	face-on	0.50	10
	13	young stars	”	”	”	”	”	”	10
Sbc202	14	cold gas	$11kpc$ $= 0.1643$ R_{vir}	1.0	retrograde -prograde	$(180, 0)$ $(30, 60)$	face-on	0.50	10
	15	young stars	”	”	”	”	”	”	10

We can put a prior constraints on some of the encounter parameters by selecting interacting galaxies at certain stages of the encounter. Identikit 2 can only model merger systems with separate galaxies with distinct cores. In these systems we can estimate the merger mass ratio by measuring its light ratio. In addition, we are looking for galaxy merger systems that have strong tidal features which are the most pronounced after the first passage. We select test GADGET simulations at times long enough after their first pass and before their second pass, such that they have separate nuclei and strong tidal tails.

The hydrodynamical simulations have separate gaseous and stellar components, with distinguishable young and old stellar populations. For Identikit modeling, line of sight velocity information is required. This informations can be obtained from cold gas (e.g. HI 21 cm emission), ionized HII regions (e.g. Hα emission), molecular clouds (i.e. CO emission), or stars (absorption). Cold neutral gas is usually more extended than the stellar population in galaxies. Resultingly, it shows more pronounced tidal features in galaxy mergers, and so it is expected to be easier to model with Identikit. However, obtaining high resolution HI data is observationally more expensive than Hα emission line maps. In this work, we compare the result of Identikit modeling using cold gas (representing HI emission), vs. young stars (representing Hα emission from HII regions).

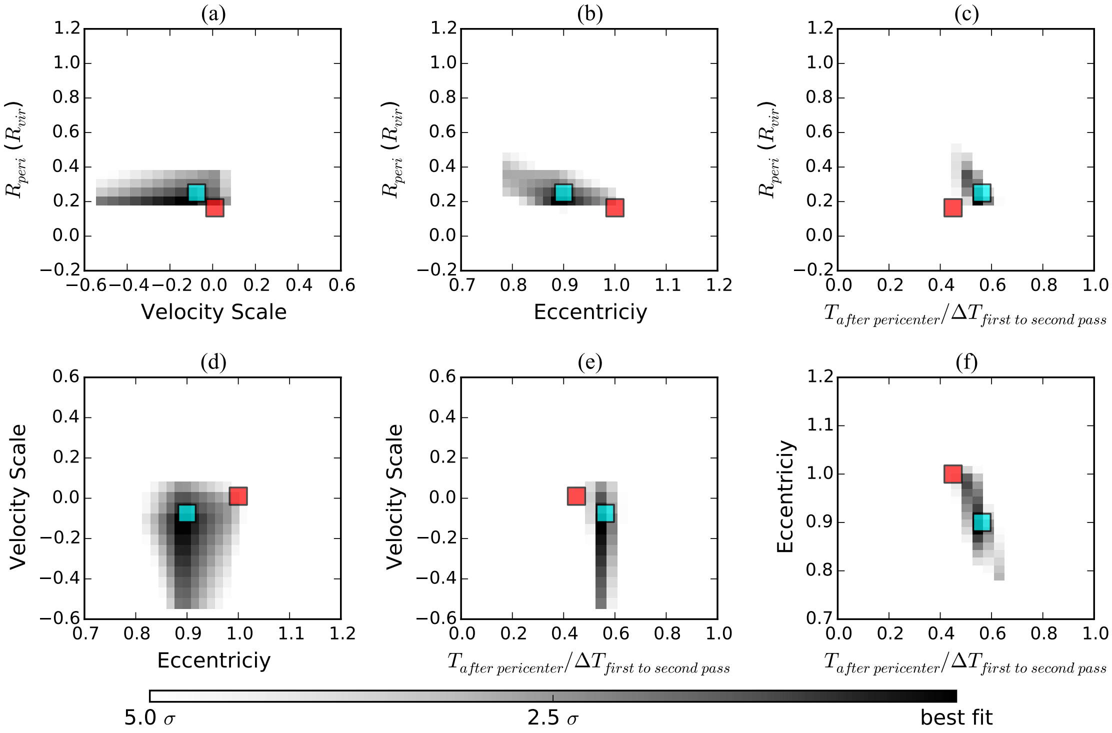

Figure 2.5: The average score maps of Identikit models matching to our fiducial GADGET simulation (Sbc201a, test 01). These are 2+1-D slices of the score map for varying (a) velocity scaling and pericentric separation, (b) eccentricity and pericentric separation, (c) time and pericentric separation, (d) eccentricity and velocity scaling, (e) time and velocity scaling, and (f) time and eccentricity. These slices are taken at the best fit point which is shown by the cyan square. The color scale goes from best-fit (black) to 8σ from best fit (white). The red squares show the correct encounter parameters of the GADGET simulation.

2.4 Results

The primary output of the routine we described in §2.2 is a score map for each test in Table 2.3.2. The score maps are 4+1-dimensional spaces (eccentricity, pericentric distance , time, velocity scale + score). As described in §2.2.1, each point in the score map refers to a member of the Identikit model library with a particular velocity scaling $\mathcal{V}$. The viewing angle, orientation of disks, and length scaling $\mathcal{L}$ is set by calculating the score for each Identikit model. The uncertainty of the scores at every point in the score map is obtained by measuring the scores 10-100 times, each with a new randomly selected set of boxes (§2.2.2), and calculating the average and standard deviation of scores at each point. The best matched Identikit model is expected to be that with the highest average score. This model is called the best-fit model and its parameters are the best-fit parameters. Models with average scores within n standard deviations of that of the best-fit model are considered to be within n σ of best-fit model. In order to visualize the variation of scores in the 4+1-D score map, we can look at its 2+1 dimensional slices at the position of best-fit model and see the shape of the region with high score in different directions. As there are 6 ways to choose 2 parameters out of 4, we show six 2+1-D score maps in Figure 2.5. The extent of the n-σ contours in each of these four directions determines the uncertainty of the corresponding parameter.

In order to measure the uncertainty of the parameters of the best-fit model determined inside Identikit and not explicitly tested in the grid of models (i.e. viewing

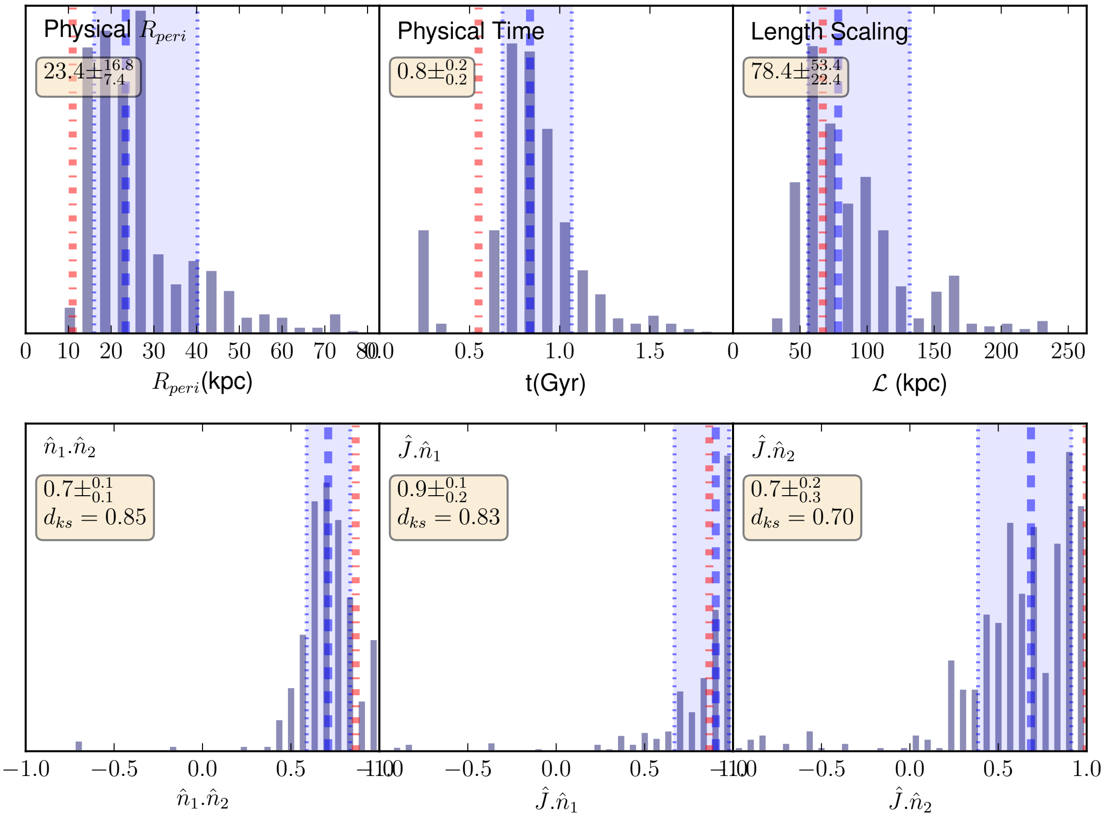

Figure 2.6: The distribution of parameters in models within 1σ contours in Figure 2.3. The blue dashed vertical line shows the median of the distribution and the red dot-dashed vertical line shows the correct value of the parameter in the GADGET simulations. The shaded areas show the interval between the 16 and 84 percentiles. The median and the limits of the shaded area are given in each panel. On the lower plots the KS test value against a cosine distribution is written. This test is considered as a good convergence because the average of $d_{KS} > 0.75$. Tests with $0.75 > d_{KS} > 0.30$ are grouped as fairly converged, and tests with $0.30 > d_{KS}$ are poorly converged.

angle, orientation of disks, length scaling $\mathcal{L}$, and physical time and physical R_{peri} which depend on $\mathcal{L}$), we study the distribution of model parameters with scores within the 1σ contour in Figure 2.3. Figure 2.6 shows these distributions for test 01. Here the distribution of physical pericentric distance ($\mathcal{L} \times R_{peri}/R_{vir}$), physical time ($\mathcal{L}/\mathcal{V} \times T_{simulation}$), length scaling $\mathcal{L}$, $\hat{n}_1.\hat{n}_2$ (dot product of orientation of the 2 disks), and $\hat{n}_i.\hat{J}$ (dot product of the orientation of disk i and system's orbital angular momentum) are shown. The latter is a quantitive measure for the system being prograde vs. retrograde. When $\hat{n}_i.\hat{J} = 1$ we have a prograde disk, when $\hat{n}_i.\hat{J} = -1$ we have a retrograde disk, and when $\hat{n}_i.\hat{J} = 0$ we have a polar disk. The correct parameter from GADGET simulation is shown with a dot-dashed red vertical line so one can easily see the bias in the distribution. We use rose plots to show the distribution of angles in models within 1σ and 3σ contours. Figure 2.7a shows the rose plots for test 01. It includes the distribution of altitude (θ) and azimuth (ϕ) of the viewing direction, along with the inclination (i) and argument to periapsis (ω) of each disk. The correct angles are shown with red dot-dashed radial lines.

In some of the tests the 1 σ distribution of initial orientation of disks converges into a narrow range of angles (Figure 2.7a). In these tests the models close to the best-fit model find close initial disk orientations, and we may infer that these models are small variations of the best-fit model. However, the 1σ distribution of initial orientation of disks are wider for some tests, and in some cases these distributions are almost flat (Figure 2.7b). A wide or flat distribution indicates that the models

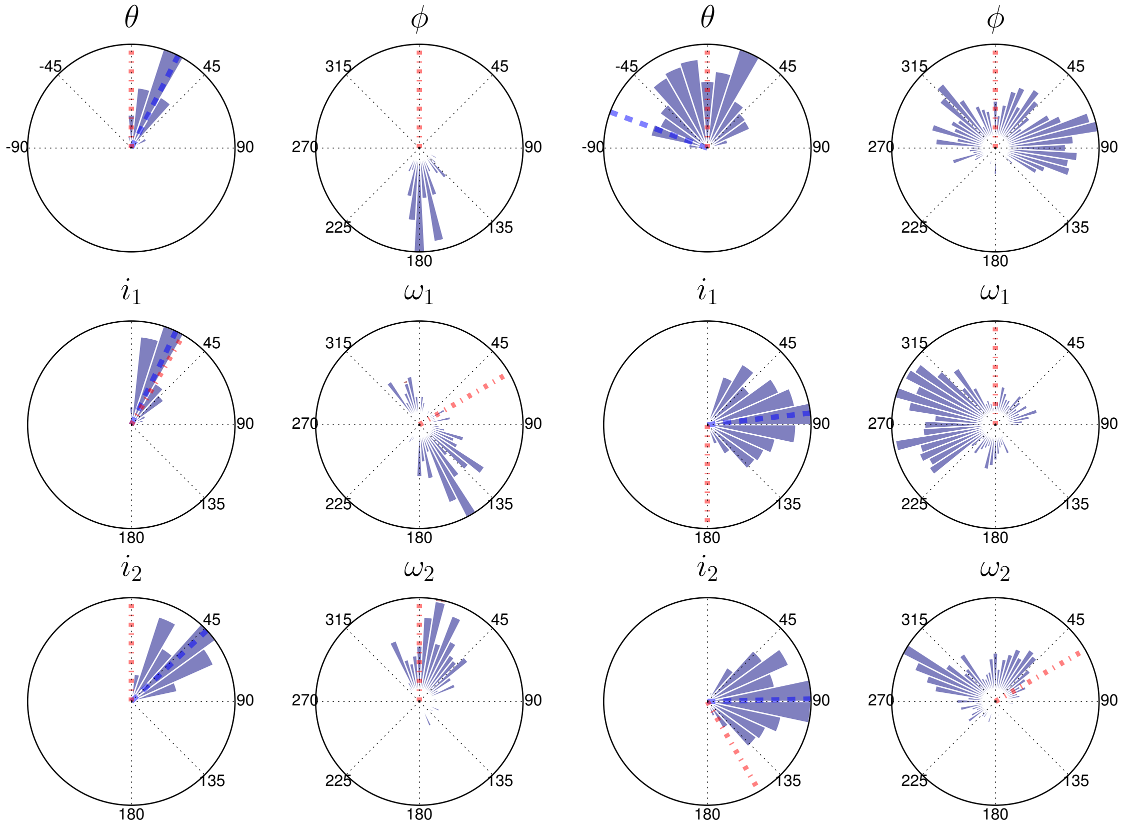

(a)

(b)

Figure 2.7: The distribution of the angles in models within 1σ (a) for test 01 which converges well and (b) for test 12 which does not converge. θ and ϕ are viewing angles, and i_d and ω_d are inclinations and argument to periapsis of disk d. Blue radial dashed lines show the median and the red radial dot-dashed lines show the correct angles. Note that in (a) i_1 is close to 0 which corresponds to the northern pole of the coordinate system. So, the difference between the correct ω_1 (red dot-dashed radial line) and the measured peak represents a small angular separation, and the distribution of disk 1 orientations is close to the correct value. In (b) the flat distribution of histograms indicate that the orientation of disks and viewing angles of the best models are random and one cannot rely on the answer for other parameters. We quantify convergence by performing a KS test on the distribution of $\hat{n}_i.\hat{J}$. The KS test value for (a) and (b) in this figure are 0.79 and 0.21, respectively. Among the 15 tests in this work we found 4 good, 9 fair, and 2 poor convergences.

with similarly high scores have very different initial disk orientations, and there is a significant degeneracy in the best-fit model. In the most extreme case, when all disk orientations are equally likely we would find a cosine distribution in $\hat{n}_1.\hat{n}_2$ and $\hat{n}_i.\hat{J}$ histograms.

We categorize the results of our tests into three groups based on the distribution of $\hat{n}_i.\hat{J}$ for models within 1σ of the best-fit model. Tests with relatively narrow peak in $\hat{n}_i.\hat{J}$ distribution are "well-converged". Tests in which the peak is considerably broader are "fairly-converged". Finally, "poor" convergence is when we have an almost flat distribution in $\hat{n}_i.\hat{J}$. In order to quantify this categorization, we perform a KS test of the distribution of $\hat{n}_i.\hat{J}$ against a cosine distribution. A large KS test value means that the distribution is not a cosine function, and a small value means it is similar to a cosine function. When the KS test value (d_{KS}) is bigger than 0.75, we label it as good convergence. When it is less that 0.30 we take the result as a poor convergence, and when it is between 0.30 and 0.75 we consider it a fair convergence. Note that KS test value limits are somewhat arbitrarily selected and can be changed to include more or less tests in good and fair groups. However, as can be seen in the best-fit vs. correct parameter plots later in this section, our selection of good, fair, and poor convergence is correlated with the accuracy of the results.

Four out of 15 tests in Table 2.3.2 have good convergence, nine have fair convergence, and two are poorly converged. All of the tests on prograde-prograde systems have good or fair convergence. Tests on edge-on systems resulted in good convergence as well. Tests on retrograde and polar systems have either poor convergence or are on the lower end of d_{KS} range for fair convergence. The reason for poor convergence is either because Identikit can not find a configuration that populates the boxes, or it is because the boxes are not restrictive enough on orientation of disks and models with different orientations give similarly good scores. We will diskuss this in §2.5.

2.4.1 The Fiducial Test

Figures 2.5 and 2.6 show the score map and distribution of parameters for test 01. This is a test on cold gaseous components of the the fiducial GADGET simulation (Sbc201a). The face-on snapshot is near the middle of the first and the second passages. Eccentricity and pericentric distance of the orbit is 1.0 and 11 kpc, respectively, and both galaxies are prograde (one of them is completely prograde and the other one is tilted by 30 degrees). We identify this test as a good converging test because the average of KS test values for $\hat{n}_i.\hat{J}$ and $\hat{n}_1.\hat{n}_2$ distributions against cosine function is bigger that 0.75.

As can be seen from Figure 2.5, our method rules out a significant fraction of parameter space in test 01. The fractional time since pericenter is well constrained. Fractional time since pericenter is the fraction of current time since pericenter to the total time between the first pass and the second pass. In this work, we chose most of the GADGET models in the mid-way between the first pass and the second pass (i.e. fractional time ≈ 0.5). In this particular test the correct fractional time is 0.45. The obtained fractional time from Figure 2.5 is 0.56 $\pm^{0.02}_{0.07}$. This time is dimensionless, and in order to find the physical time since pericenter we need to scale it using the length and velocity scalings ($\mathcal{L}/\mathcal{V}$). The velocity scaling is one of the free parameters in our tests. However, as described in §2.2.1, when we lock the centers of the galaxies length scaling is determined by the viewing angle. Any bias in the measured viewing angle leads to a bias in length scaling. The distribution of length scalings of the models within 1σ contour are shown on the top-right panel of Figure 2.6. One can see the length scaling is slightly overestimated within the uncertainty. Velocity scaling of models within the 1σ contour is also slightly underestimated (see Figures 2.5a, 2.5d, and 2.5e). Physical time is scaled by $\mathcal{L}/\mathcal{V}$, so the distribution of physical time since pericenter for these models overestimated. (See top-middle panel of Figure 2.6.) The measured physical time since pericenter is $0.8\pm^{0.2}_{0.2}$ Gyrs, which is within 1.5σ of the correct answer (0.55 Gyrs). The orientation of disks with respect to orbital angular momentum is shown in $\hat{n_i}.\hat{J}$ panels in Figure 2.6. For both disks the distribution correctly indicates prograde disk orientation. The correct answer is also recovered for viewing angles θ and ϕ in Figure 2.7a. Pericentric separation is also well constrained. The score maps of Figure 2.5 show a that models with R_{peri} close to the correct value give a higher score. Figure 2.5 shows the dimensionless R_{peri} which is the fraction of R_{peri} to the virial radius of isolated halos. The measured value is 0.25 R_{vir} $\pm^{0.09}_{0.06}$ R_{vir} which is slightly larger than the correct value of 0.16 R_{vir}. The physical pericentric separation is obtained by multiplying this value by the length scaling parameter $\mathcal{L}$

which is also slightly overestimated. As a result, the physical pericentric separation is almost twice the correct value ($23.4\pm^{16.8}_{7.4}$kpc vs. 11.0 kpc). Eccentricity is not as well constrained. The black regions on the score maps of Figure 2.5 is broad in the direction of eccentricity ($0.90\pm^{0.15}_{0.05}$). This range includes the correct value of 1.0, but the uncertainty is large given the total range of eccentricities explored is 0.3 (from 0.80 to 1.10)

We present the result of other tests by examining the parameters adjusted in the GADGET simulations in Table 2.3.2.

2.4.2 Time Since Pericenter

In tests 03 and 04 (see Table 2.3.2) we use the exact same GADGET model used in test 01, but observed at earlier and later fractional times respectively. Fractional time is the time since the first passage divided by the total time between the first and the second passages, so it is a measure of the merger stage. Test 03 is well converged with average $d_{KS} = 0.90$. In this test, the correct fractional time is 0.25, which is equivalent to 0.30 Gyr after the first pass. The obtained fractional time for this model is $0.30\pm^{0.06}_{0.10}$ and the measured physical time since pericenter is $0.34\pm^{0.11}_{0.22}$ Gyr. Test 04 is well converged. In this test, the correct fractional time is 0.75, which is equivalent to 0.85 Gyr after pericenter. The best-fit fractional time is $0.86\pm^{0.01}_{0.01}$ and the obtained best-fit physical time is $1.26\pm^{0.28}_{0.21}$ Gyr. Fractional and physical time is biased especially in the late stage test (test 04); however, it is encouraging that we recover the time within 10% of the correct value.

In the rest of the tests we use snapshots of the GADGET simulations that are near the middle of the first and the second passages (fractional time ≈ 0.5). Figure 2.8 shows the best-fit vs. correct values of fractional time and physical time since pericenter. In this figure we use different marker sizes, line thicknesses, and color darknesses for tests with different convergences to emphasize good and fair tests. We do the same for all best-fit vs. correct plots in this work. We only study tests with good and fair convergence. Parameters in tests with poor convergence usually have large uncertainties and are not reliable measurements. They are plotted, however, for the sake of comparison. The tests with good and fair convergence are following the black line with a scatter of ≈ 0.2 in fractional time, and the best-fit fractional times are mostly within 1 σ of the correct value.

The physical time, which is obtained with a combination of length and velocity scalings ($\mathcal{L}/\mathcal{V}$), is more clearly biased toward later times in tests with fair convergence. The average bias in these tests is about 0.3 Gyr. In tests with good convergence, however, there is less bias. The bias seem to be stronger in tests on later stages, and it is about 0.2 Gyr. Test on edge-on systems (with both good and fair convergences) do not show significant bias. (see Figure 2.8b). These systematics can be corrected when we apply our method on real data.

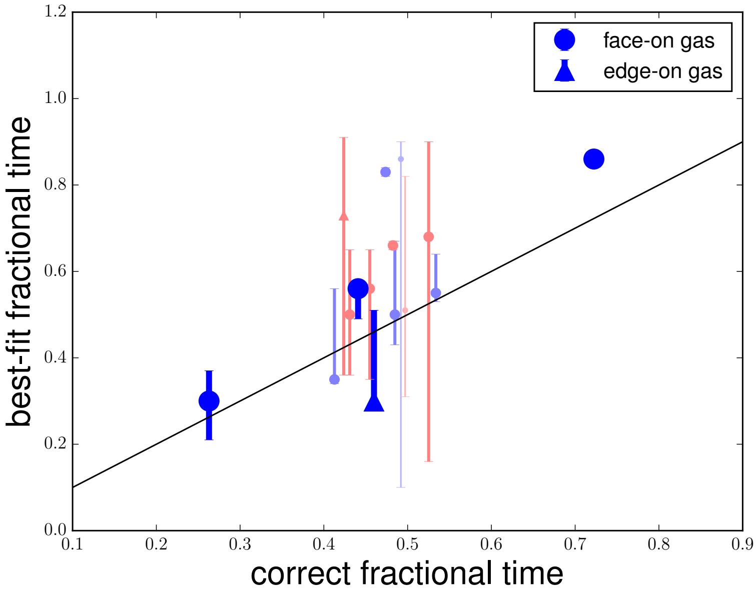

(a)

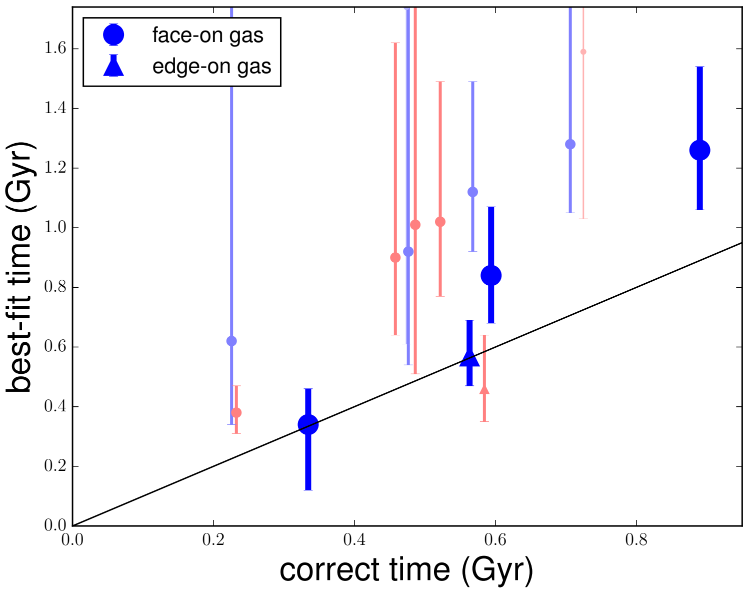

(b)

Figure 2.8: Correct vs. best-fit values of (a) fractional time and (b) physical time since pericenter for all the tests in this work. The blue markers are test on cold gaseous component, and red markers are tests on young stars. The face-on tests are shown with circles and the edge-on tests are shown with triangles. Tests with good, fair, and poor convergence are shown with big, medium and small markers, respectively.

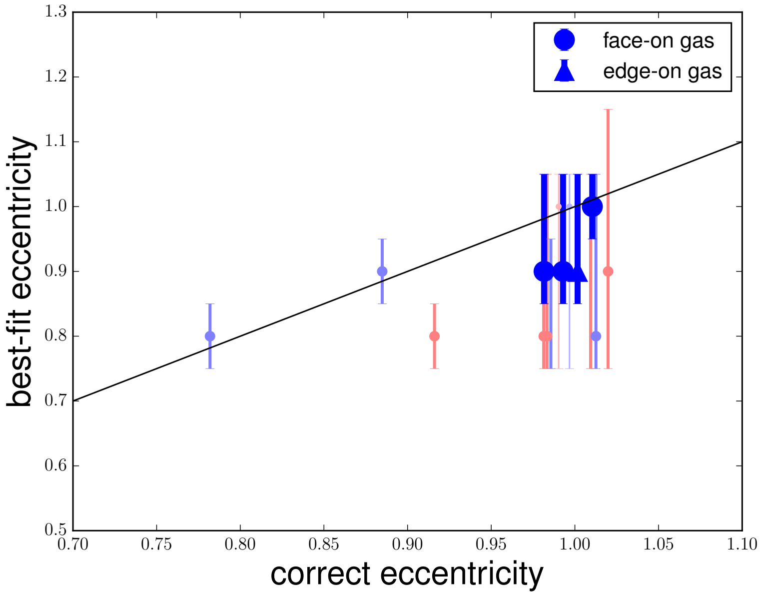

Figure 2.9: Correct vs. best-fit values of eccentricity for all of the tests in this work. Symbols and colors are as in Figure 2.8. The correct values have been artificially scattered a little to make the points and error bars visible.

2.4.3 Eccentricity

Most of the GADGET simulations we used in this work have eccentricity=1.0 (i.e. parabolic orbit). This corresponds to Keplerian orbits with zero energy, which is preferred if galaxies and dark matter halos they live in start approaching each other from stationary and gravitationally unbound origins. In most of the good and fair tests with eccentricity equal to 1.0, we underestimate the eccentricity of the orbit. In Figure 2.9 which shows the measured eccentricity vs. correct eccentricity all of parabolic tests with good convergence cover the black line. Their correct eccentricity is artificially slightly randomized to improve visibility.

All of the tests on elliptical orbits result in fair convergence. In these tests, we recover the elliptical nature of the orbit, though the eccentricity is underestimated in test 08. In test 07 on cold gas with correct eccentricity of 0.9, the measured eccentricity is $0.90\pm^{0.05}_{0.05}$. Test 08 on the young stars of the same simulation result in a slightly better eccentricity ($0.80\pm^{0.05}_{0.05}$). In test 09 in which the correct eccentricity is 0.8 and the pericentric distance is larger than other tests, we also obtain an elliptical orbit correct eccentricity ($e = 0.80\pm^{0.05}_{0.05}$). The fact that we found elliptical orbits for all of these tests suggest that we can not put strong constraint on eccentricity. When we measure elliptical orbit for a real system using our method, it is hard to say if the orbit is really elliptical or it is parabolic, but underestimated. However, it seems that when we measure parabolic orbit for a real system the constraint is reliable. Further investigation is required to understand the behavior of measured eccentricity.

2.4.4 Pericentric Separation

Figure 2.10 shows the best-fit vs. correct answer for both the dimensionless (R_{peri}/R_{vir}) and physical pericentric distance. Identikit measures the pericentric separation in units of the virial radius of isolated galaxies which is the dimensionless pericentric distance. In order to find the physical pericentric distance one has to scale dimensionless pericentric distance with the length scaling, $\mathcal{L}$. All but one of the GADGET simulations we tested have the same input R_{peri} (11 kpc).

Fractional pericentric distance is within 1.5σ of the correct value in all of well-converged tests (Figure 2.10a). When scaled with the length scaling $\mathcal{L}$ to obtain the

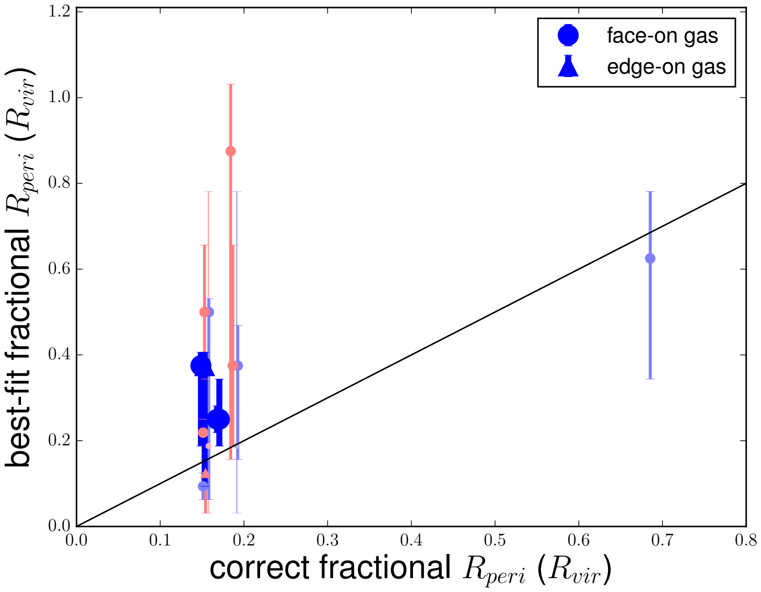

(a)

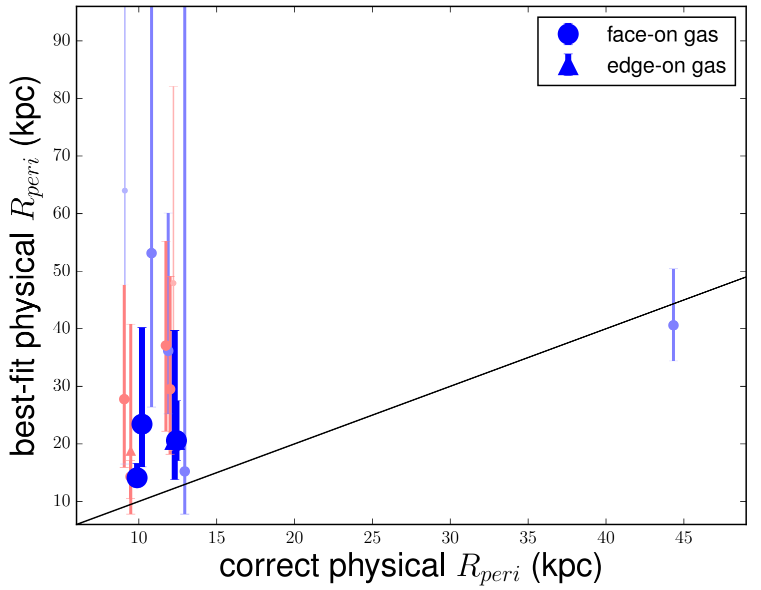

(b)

Figure 2.10: Correct vs. best-fit values of (a) dimensionless and (b) physical pericentric distance. Symbols and colors are as in Figure 2.8. The correct values have been artificially scattered a little to make the points and error bars visible.

physical pericentric distance, all move to slightly above the black line within 2σ (Figure 2.10b). Most of fairly converged tests on cold gas (blue points in Figure 2.10a) have correct pericentric separation within the error bars. Though their physical Physical R_{peri} is highly overestimated. The opposite is true for fairly converged tests on young stars, they have larger fractional pericentric distance, but their physical R_{peri}s is mostly within 2σ of the correct value. It is worth noting that the results of edge-on tests are closer to correct pericentric distance both in good and fair convergences.

2.4.5 Viewing Angle

Figure 2.11 shows the correct vs. measured altitude in viewing angle. Most of the tests are face-on (Correct $\theta = 0°$). Good and fair tests are scattered in the range from $-30°$ to $+10°$ degrees. It can be seen that there is no major difference between tests on gas and young stars when it comes to best-fit viewing direction of face-on systems.

Two of the tests (05 and 06) are on edge-on systems (Correct $\theta = 90$). Both tests converge and the answers for θ of the viewing angle are within 10° and 20° for the cold gas and young star tests, respectively. We can see in Figures 2.8 and 2.10 that edge-on tests result in better best-fit physical time and pericentric distance than most of face-on tests. This suggests that in edge-on systems we have better constraints to model mergers stage and R_{peri}. In a merger of edge-on disks, the velocity difference in tidal streams are more visible in the line of sight direction. The better visibility of

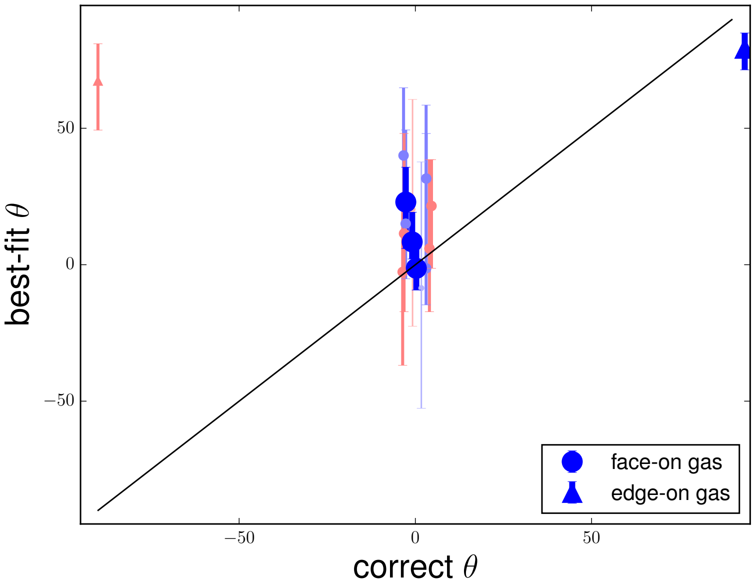

Figure 2.11: Correct vs. best-fit values of altitude of viewing angle. Symbols and colors are as in Figure 2.8. The correct values have been artificially scattered a little to make the points and error bars visible. The error bar of the test on the edge-on cold gas system is too small to be visible.

velocity variations puts a stronger constraint on length and velocity scalings which results in better constraints on dependent parameters.

2.4.6 Initial Orientation of disks

Figure 2.12 shows the correct vs. obtained values for orientation of disks. We use $\hat{n_i}.\hat{J}$ to show the orientation of disks with respect to the orbital angular momentum of the galaxy merger. $\hat{n_i}$ is the unit vector of the orientation of disk i and $\hat{J}$ is the unit vector of angular momentum of the orbit. So, when $\hat{n_i}.\hat{J} = 1$ we have a prograde disk, when $\hat{n_i}.\hat{J} = -1$ we have a retrograde disk, and when $\hat{n_i}.\hat{J} = 0$ we have a polar disk. Values in between these reflect systems that are more or less prograde, polar, or retrograde. We also use $\hat{n_1}.\hat{n_2}$ to show the orientation of disks with respect to each other.

Nine out of 15 tests are on prograde-prograde galaxy mergers. Four of them resulted in good convergence. All the rest are fairly converged. The measured $\hat{n_i}.\hat{J}$ and $\hat{n_1}.\hat{n_2}$ for all of these tests are within 0.3 of the correct answer (≈ 1.0), with the exception of test 10.

The remaining six tests are on prograde-polar (tests 10, 11), retrograde-retrograde (tests 12, 13), and prograde-retrograde (tests 14, 15) orbits. All but two of them (tests 11 and 12) result in fair convergence. Tests 10 and 14 have fair convergence, though they are also on the lower end of the range of d_{KS} for fair convergence. Tests 13 and 15, however result in a reasonable convergence. The orientation of disks are within 0.3

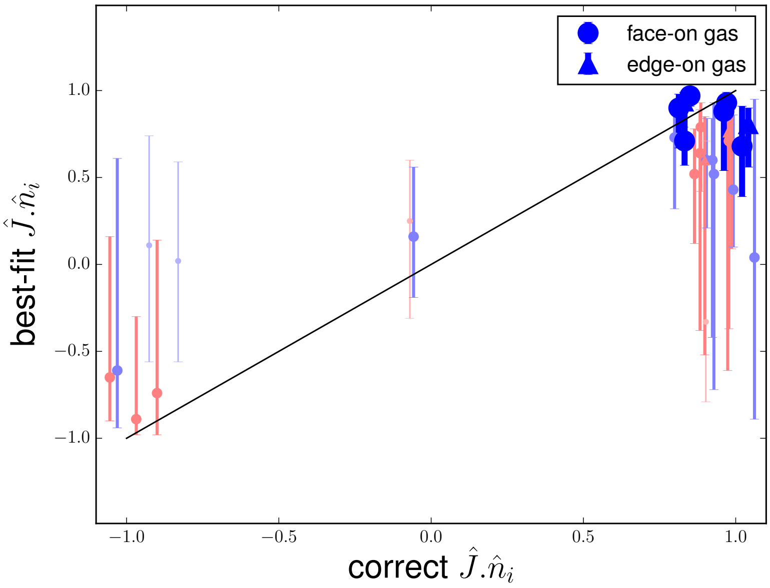

(a)

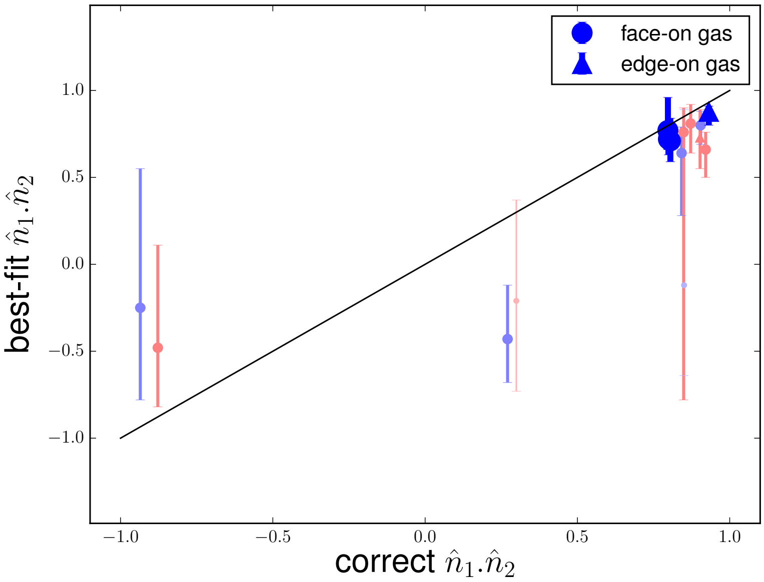

(b)

Figure 2.12: Correct vs. best-fit values of (a) $\hat{n}_i.\hat{J}$, and (b) $\hat{n_1}.\hat{n_2}$. Symbols and colors are as in Figure 2.8. The correct values have been artificially scattered a little to make the points and error bars visible.

in $\hat{n_i}.\hat{J}$ of the correct value in Figure 2.12a These tests are both on young stars. Tests on cold gas in retrograde or polar orbits are not successful, because direct collision between gas particles produce dissipation that can not be modeled by collisionless test particles in Identikit. In general, we expected poorer match for retrograde systems as the tidal features are less pronounced. However, in the original Identikit paper (Barnes & Hibbard 2009) some artificial merger models with retrograde disks were successfully reproduced by visual matching in the interactive interface of Identikit. We will diskuss these systems in §2.5.

Test ID	component explored	number of matching runs	convergence quality (KS test value)	best-fit pericentric distance	best-fit eccentricity	best-fit time $\Delta T/T_{\text{first to second pass}}$*
01	cold gas	10	good (0.79)	$23.4 kpc$ $(\pm^{16.8}_{7.4} kpc)$ $= 0.25\ R_{vir}$ $(\pm^{0.09}_{0.06} R_{vir})$	0.90 $(\pm^{0.15}_{0.05})$	0.56 $(\pm^{0.02}_{0.07})$ $= 0.84$ $(\pm^{0.23}_{0.15} Gyr)$
02	young stars	10	fair (0.63)	$27.8 kpc$ $(\pm^{19.8}_{11.9} kpc)$ $= 0.38\ R_{vir}$ $(\pm^{0.28}_{0.19} R_{vir})$	0.90 $(\pm^{0.25}_{0.15})$	0.56 $(\pm^{0.08}_{0.21})$ $= 1.02$ $(\pm^{0.47}_{0.25} Gyr)$
03	cold gas	10	good (0.90)	$20.6 kpc$ $(\pm^{6.9}_{3.4} kpc)$ $= 0.38\ R_{vir}$ $(\pm^{0.03}_{0.19} R_{vir})$	0.90 $(\pm^{0.15}_{0.05})$	0.30 $(\pm^{0.06}_{0.10})$ $= 0.34$ $(\pm^{0.11}_{0.22} Gyr)$
04	cold gas	10	good (0.91)	$14.1 kpc$ $(\pm^{2.5}_{1.4} kpc)$ $= 0.25\ R_{vir}$ $(\pm^{0.03}_{0.03} R_{vir})$	1.00 $(\pm^{0.05}_{0.05})$	0.86 $(\pm^{0.01}_{0.01})$ $= 1.26$ $(\pm^{0.28}_{0.21} Gyr)$
05	cold gas	10	good (0.88)	$20.7 kpc$ $(\pm^{19.0}_{7.0} kpc)$ $= 0.38\ R_{vir}$ $(\pm^{0.03}_{0.28} R_{vir})$	0.90 $(\pm^{0.15}_{0.05})$	0.30 $(\pm^{0.21}_{0.01})$ $= 0.57$ $(\pm^{0.12}_{0.10} Gyr)$
06	young stars	10	fair (0.60)	$18.8 kpc$ $(\pm^{22.0}_{11.1} kpc)$	1.00 $(\pm^{0.05}_{0.25})$	0.73 $(\pm^{0.18}_{0.37})$

Continued on next page

Table 2.1 – *Continued from previous page*

Test ID	component explored	number of matching runs	convergence quality (KS test value)	best-fit pericentric distance	best-fit eccentricity	best-fit time $\Delta T/T_{\text{first to second pass}}$*
				$= 0.12\ R_{vir}$ $(\pm^{0.22}_{0.09} R_{vir})$		$= 0.46$ $(\pm^{0.18}_{0.11} Gyr)$
07	cold gas	10	fair (0.51)	$15.2 kpc$ $(\pm^{109.9}_{7.5} kpc)$ $= 0.09\ R_{vir}$ $(\pm^{0.03}_{0.03} R_{vir})$	0.90 $(\pm^{0.05}_{0.05})$	0.83 $(\pm^{0.01}_{0.01})$ $= 0.62$ $(\pm^{2.16}_{0.28} Gyr)$
08	young stars	10	fair (0.70)	$14.3 kpc$ $(\pm^{2.8}_{3.8} kpc)$ $= 0.22\ R_{vir}$ $(\pm^{0.03}_{0.03} R_{vir})$	≤ 0.80 $(\pm^{0.05}_{---})$	0.66 $(\pm^{0.01}_{0.01})$ $= 0.38$ $(\pm^{0.09}_{0.07} Gyr)$
09	cold gas	10	fair (0.68)	$40.6 kpc$ $(\pm^{9.8}_{6.2} kpc)$ $= 0.62\ R_{vir}$ $(\pm^{0.16}_{0.28} R_{vir})$	≤ 0.80 $(\pm^{0.05}_{---})$	0.55 $(\pm^{0.09}_{0.02})$ $= 1.12$ $(\pm^{0.37}_{0.20} Gyr)$
10	cold gas	10	fair (0.40)	$53.1 kpc$ $(\pm^{76.3}_{26.7} kpc)$ $= 0.50\ R_{vir}$ $(\pm^{0.03}_{0.44} R_{vir})$	≤ 0.80 $(\pm^{0.25}_{---})$	0.50 $(\pm^{0.17}_{0.07})$ $= 1.28$ $(\pm^{2.05}_{0.23} Gyr)$
11	young stars	10	poor (0.28)	$47.9 kpc$ $(\pm^{34.2}_{29.0} kpc)$ $= 0.19\ R_{vir}$	1.00 $(\pm^{0.05}_{0.25})$	0.51 $(\pm^{0.31}_{0.20})$ $= 1.59$

Continued on next page

Table 2.1 – *Continued from previous page*

Test ID	component explored	number of matching runs	convergence quality (KS test value)	best-fit pericentric distance	best-fit eccentricity	best-fit time $\Delta T/T_{\text{first to second pass}}{}^{*}$
				$(\pm^{0.59}_{0.16} R_{vir})$		$(\pm^{0.78}_{0.56} Gyr)$
12	cold gas	10	poor (0.21)	$64.0 kpc$ $(\pm^{54.2}_{47.5} kpc)$ $= 0.19\ R_{vir}$ $(\pm^{0.59}_{0.16} R_{vir})$	1.00 $(\pm^{0.05}_{0.25})$	0.86 $(\pm^{0.04}_{0.76})$ $= 1.74$ $(\pm^{3.36}_{1.12} Gyr)$
13	young stars	10	fair (0.55)	$37.1 kpc$ $(\pm^{18.2}_{14.9} kpc)$ $= 0.88\ R_{vir}$ $(\pm^{0.16}_{0.72} R_{vir})$	≤ 0.80 $(\pm^{0.25}_{---})$	0.68 $(\pm^{0.22}_{0.52})$ $= 1.01$ $(\pm^{1.26}_{0.49} Gyr)$
14	cold gas	10	fair (0.46)	$36.2 kpc$ $(\pm^{23.9}_{11.0} kpc)$ $= 0.38\ R_{vir}$ $(\pm^{0.09}_{0.22} R_{vir})$	0.90 $(\pm^{0.05}_{0.15})$	0.35 $(\pm^{0.22}_{0.01})$ $= 0.92$ $(\pm^{1.02}_{0.38} Gyr)$
15	young stars	10	fair (0.56)	$29.5 kpc$ $(\pm^{19.6}_{11.3} kpc)$ $= 0.50\ R_{vir}$ $(\pm^{0.16}_{0.37} R_{vir})$	≤ 0.80 $(\pm^{0.25}_{---})$	0.50 $(\pm^{0.15}_{0.14})$ $= 0.90$ $(\pm^{0.72}_{0.26} Gyr)$

2.5 Discussion

Our method results in good and fair convergence for all of the prograde-prograde tests; nevertheless all but two of the retrograde and polar tests have poor (or poor fair) convergence. In the converging tests, we can rule out a large fraction of the parameter space, albeit with systematic offsets from the input parameters.

2.5.1 Parameters in Converged Tests

The random uncertainties are obtained by calculating how the scores are affected when we move the boxes around on tidal tails. In our early work on Identikit, we noticed that box positioning had the biggest effect on scores. Nevertheless, there may be other sources of random error (e.g. error from noise in the data) that we did not take into account in our calculations. The uncertainties we measured are lower limits to the real uncertainties.

Time since pericenter (both physical and fractional) is the best constrained parameter in tests with good and fair convergence. This is an important parameter as it tells us whether the interacting galaxies are in early or late merger stage. We selected most of the snapshots to be in the midway between the first and the second pass. In a couple of tests we recovered the time of an early and a late stage galaxy merger (see Figure 2.8). In tests of edge-on systems we recovered the correct merger time to 1σ level. Though, there is an average bias of ~ 0.3 Gyrs toward later physical times in tests on face-on systems. This bias could be due to the different mass models of the two simulations. The difference in the luminous to dark matter scale length affects the development of tidal features and the bridges. A more extended tidal feature may start to fall back into a galaxy earlier, making it look like a model with shorter tidal feature at a later time. Alternatively, this bias may be originating from the different nature of particles in GADGET simulations vs. Identikit. If the later is the main cause of the bias, we can correct for it when this method is applied on real data. With more tests on a variety of mass models we can track the cause of this bias more precisely.

Pericentric distance, viewing angle, and initial orientation of disks are other parameters that are relatively well constrained. The tested GADGET simulations had limited range for these parameters, because we did not make them ourselves. Ten out of 13 good and fair converged tests have parabolic orbit, and for most of them the eccentricity is underestimated. We recovered the elliptical nature of tests with eccentricity $e < 1$, but we can not constrain the eccentricity, as in these tests only by looking at the results it is not possible to distinguish between underestimated parabolic orbits and true elliptical ones. In all of the good and fair tests the measured viewing angle is within 30° of the correct value (See Figure 2.11). Fractional pericentric distance is within 1.5σ of the correct value in all of tests on cold gas with good and fair convergence; though, there is an average bias of $\sim 30\%$ toward larger physical R_{peri} in face-on tests. For tests on young stars, generally, the constraint on pericentric distance is less strong. The pericentric separation is hard to model, even when visual matching is utilized and the sophisticated patterns recognizable to human brain are matched. The cause of the bias may also be the different mass models of the two simulations or because of using test-particles in Identikit. The initial disk orientations are also well constrained in most of well- and fairly-converged tests. In these tests the measured $\hat{n_i}.\hat{J}$s and $\hat{n_1}.\hat{n_2}$s are within 0.3 of the correct value.

Cold gas and young stars reveal different results. In simulations that we test both cold gas and young stars the measured values for pericentric distance and disk orientations are significantly different from each other. All of the four good convergences are for tests in cold gas. However, tests on young stars gave better results for the elliptical orbit and in retrograde and polar disk orientations. This suggests that even though HI data is a better component for dynamical modeling of prograde disk interactions, Hα kinematics is favorable for modeling polar and retrograde orbits. In general, young stars are harder to model because they are less extended than cold gas, and the tidal features are not as strong. (The disk scale length R_d for cold gas is 3 times the R_d for stars in GADGET simulations). As young stars are a small portion of the total stellar population we expect that using data from all of the stars will improve the results. Nevertheless, measuring the kinematics of stars is more challenging in faint tidal features. In real data, young stars are traced by HII regions radiating Hα, a relatively easy-to-measure emission line. With optical and near infrared imaging we can measure the morphology of the total stellar population.

2.5.2 Poor-Convergence, Retrograde and Polar Tests

In poor converging tests, Identikit results in random orientation of disks even in the models that are close to the best-fit model. So, when we plot the distribution of orientations in these models it looks similar to a uniform distribution (Figure 2.7b). Uniform distribution of orientations leads to a cosine distribution in $\hat{n}_i.\hat{J}$. In order to quantify convergence we perform a KS test on the distribution of $\hat{n}_i.\hat{J}$ against a cosine distribution. Small KS test value means that the distribution is similar to a cosine function and there is no convergence. On the other hand, from a large KS test value we infer that the best models converged to a small range of possible orientations. A peculiar non-converging distribution (e.g. a distribution that has peaks near -1 and +1) can also give large KS test value against a cosine function, but we checked the results visually to make sure that there is no significant contamination from this type of non-converging distributions. In this work the KS test values of 0.75 and 0.30 are used as dividing values between good (> 0.75), fair(> 0.30, < 0.75), and poor(< 0.30) convergence.

The random orientation of disks can be the result of two scenarios. In some cases, when Identikit does not find a good combination of orientation of disks and viewing angle, it gives score of -99.00 and arbitrary orientations for disks. Alternatively, one may place the boxes in certain regions, so that many disk orientations and viewing angles populate them equally well and result in good scores. Resultingly, the distribution of orientations will look similar to a uniform distribution. For retrograde

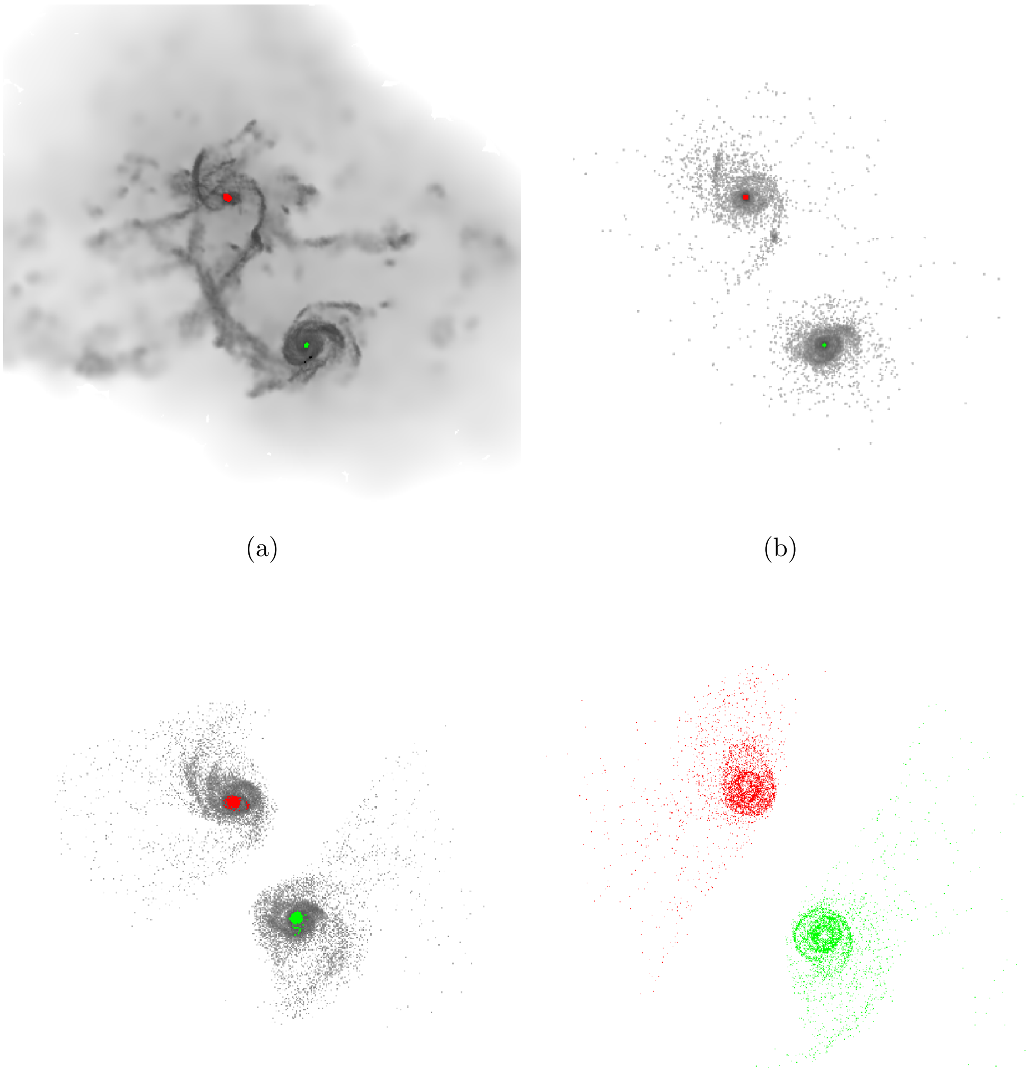

(a) (b)

(c) (d)

Figure 2.13: (a), (b), and (c) are cold gas, young stars, and old stars in GADGET simulations of the retrograde-retrograde test (tests 12 and 13). Gas dissipation reshapes the gaseous tidal tails in a way that Identikit cannot reproduce. Young stellar population have less surface brightness in the outer parts of the tidal features than old stellar population. (d) shows the Identikit model with the same initial parameters. The tidal features in the correct Identikit model is a better visual match to the old stellar population (c), which is the majority of total stellar population.

and polar tests in this work it is likely that the second scenario is causing the non-convergence.

In most of the retrograde systems the tidal features are less pronounced and closer to the center of the system. When the system has weak tidal features our automated box selection routine selects boxes close to the centers of the galaxies. The indicated phase space regions (boxes) can be populated with many configurations because of being close to the center of the galaxies. Models with poor match to data will obtain average scores that are as good as that of models with good match. So, the best-fit model and the models close in score to the best-fit model will have a mix of parameters from well and poorly matched models, and this will make the distribution of orientations similar to that of a non-converging test.

For one of retrograde tests, we changed the size of the boxes and tried to place them manually in places that are most similar to the choices in Barnes 2011. This attempt also failed. However, if we visually compare models with similar scores, we can distinguish a good match from a poor one. This means that Identikit algorithm does not capture all of the information one can possibly extract from visual matching.

Retrograde mergers have other difficulties that make their modeling more complicated. There is a significant difference in the shape and position of the tidal features when we study different components of the retrograde GADGET simulation. The gas is dissipative, and when gaseous arms collide, their position, velocity, and shape starts to offset from those of the collisionless stars. Because Identikit does not have a gaseous component, it does not reproduce these differences (Figure 2.13). Test particles better represent the collisionless stars. However, we are only testing young stars, which are a small fraction of all stars in these GADGET simulations. They are not extended as much as the total stellar population, and they have less similarity to Identikit models. One solution may be to match Identikit models to the total stellar population (Figure 2.13). However, measuring the stellar kinematics requires high signal to noise spectroscopy which is hard to obtain in faint tidal features. We plan to test total stellar population in morphology and young stars in kinematics simultaneously to see if we can obtain better results.

We think that changing the number of massive or test particles in Identikit simulations will not improve the convergence to a great extent. The features we try to match are large scale tails and bridges which are not significantly affected by the resolution of the simulations. Besides, more test particles improves the scores of all models, including models with poor match. The higher score would be due to more test particles populating the user selected phase space boxes. The scores for all models will become higher; however, what matters is the difference in scores, and higher scores in the whole score map will not improve a poor convergence.

2.6 Summary

In this Chapter we have developed an automated method for modeling pairs of interacting galaxies using Identikit. Our method measures the initial conditions of major galaxy mergers and provides the uncertainty for each measurement. We tested this method using an independent set of hydrodynamical simulations of encountering galaxies. We performed the tests on galaxy merger models with various encounter parameters in eccentricity, pericentric separation, time since pericenter, viewing angle, and initial orientation of disks. We also tested both cold gas and young stars in order to check the result of using different velocity tracers for kinematics data. We found that:

1. We can group test results into good, fair, and poor convergence, based on the distribution of initial disk orientations in models within 1 σ of the best fit model.
2. For most of the good and fair converged tests we recover the time since pericenter, pericentric distance, viewing angle, and initial disk orientations, within 30% of the explored range from the correct value. For some parameters there are systematic offsets that can be corrected for measurements of real data
3. The tests performed on the edge-on systems result in less biased initial conditions compared to the tests on face-on systems.
4. We do not find worse convergence in the retrograde or polar tests. This may be due to the fact that we only use the tidal features to find the best match,

and tidal features are not as strong in retrograde and polar systems or when we only study the young stars. The using of rotation curves as additional constraint on the system, and looking at the total stellar populations may improve these results. Besides, stripping or dissipation of cold gas may limit our tidal-tail finder.

Based on these results, our automated method can be used to find the initial conditions of prograde major galaxy mergers observed with both HI and Hα emission lines. However, we need to improve our modeling tool for retrograde and polar systems.

Chapter 3

Modeling the Dynamics of the Mice Galaxies: HI vs. Hα Kinematics

In this Chapter we explore the effect of using different kinematic tracers (HI and Hα) on measuring the encounter parameters of the Mice major galaxy merger (NGC 4676A/B). We observed the Mice using the SparsePak Integral Field Unit (IFU) on the WYIN telescope, and compared the Hα velocity map with JVLA HI observations. The relatively high spectral resolution of our data (R $\approx$ 5000) allows us to resolve more than one kinematic components in Hα emission line of some of the fibers. We separate the Hα emission of the star forming regions from that of shock-heated regions based on the [N II]/Hα line ratio and the velocity dispersion of the components. We

show that the kinematics of star-forming regions agree with that of the cold gas (HI), particularly in the tidal tails of the system. We measure the encounter parameters of the Mice by matching the morphology and kinematics of the tidal tails of the Mice with a galaxy merger simulation. We use an automated modeling method based on the Identikit software package. In our method, we quantify the goodness of the match and the uncertainty of the resulting encounter parameters. Most of the measured initial conditions using Hα and HI kinematics are consistent within the measurement uncertainty, and qualitatively agree with the results of previous works based 0n visual matching techniques. For example, measure $210\pm^{50}_{40}$ Myrs, and $180\pm^{50}_{40}$ Myrs For the time since pericenter, when modeling Hα and HI kinematics, respectively. This confirms that in some cases, Hα kinematics can be used instead of HI kinematics for measuring the initial conditions of galaxy mergers, and our automated modeling method is applicable on some merging systems.

3.1 Introduction

Galaxy mergers are key processes in the formation and evolution of galaxies. They are one of the major contributors to the mass assembly of galaxies, they induce starbursts in galaxies, and they are likely to be responsible for the transformation of the morphology and kinematics of disk-dominated, rotation-supported galaxies to bulge-dominated, dispersion supported ones (Toomre & Toomre 1972, Barnes &

Hernquist 1996, Mihos & Hernquist 1996).

Measuring the encounter parameters of galaxy mergers (including their initial conditions, orbital parameters, and observer-dependent parameters) via dynamical modeling puts new constraints on our understanding of galaxy evolution and cosmology. For example, isolated hydrodynamical disc-disc galaxy mergers have shown that the initial conditions such as pericentric separation and initial orientation of discs affects the timing and amount of merger induced star formation (Cox et al. 2008, Snyder et al. 2011). Dynamical modeling constrains these parameters independent of the measured star formation history in the system,so one can use them as independent tools for testing models of merger-induced star-formation (See §3.5.1). In addition, we have learned that the initial orientation of interacting discs correlates with whether the remnant will be a fast or a slow rotator. (Bois et al. 2011; Naab et al. 2014) Besides, we can put constraints on cosmological dark matter simulations by measuring the orbital parameters of galaxy mergers (e.g. eccentricity) for a statistical sample. Distribution of orbital parameters of galaxy mergers can be compared with that of dark matter halo mergers in these simulations (e.g. see Benson 2005, Khochfar & Burkert 2006).

During interactions, galaxies often experience strong tidal forces when they pass by each other, producing strong tidal features in discs. These features are usually strongest after the first pericenter, though their shape and strength is a complex function of the initial parameters of the orbit and the individual galaxies (Dubinski et al. 1995, Springel & White 1999, Barnes 2016). The sensitivity of the shape and velocity of these features to the initial conditions make them strong tools for modeling the dynamics of galaxy mergers and measuring their initial conditions (Barnes & Hibbard, 2009).

Dynamical modeling of galaxy mergers is possible by finding the most similar simulation to the morphology and kinematics the data. Tidal features play a key role in this process as they are large scale structures and it is easier to reproduce them than it is to reproduce small self-gravitating features like stellar clusters (Dubinski et al., 1999). Here,"most similar" is a vague term. Most previous attempts to model galaxy mergers have used qualitative, subjective matching criteria obtained by visual inspection of the model and data (Toomre & Toomre 1972; Barnes & Hibbard 2009). In Chapter 2 we developed an automated method based on Identikit 2 (Barnes 2011). In this method we use collisionless massless particles to reproduce tidal features. Our method is not only less subjective than the visual matching techniques, but also provides well-defined error-bars for the measured initial conditions.

For modeling a galaxy merger, we need to know the velocity of tidal features. There have been some attempts to model merger systems without using velocity information, only trying to match the morphology of the model with data (Borne & Richstone 1991, Shamir et al. 2013, Holincheck et al. 2016). However, there is more degeneracy in the possible solutions when one does not have data on the velocity gradient across the tidal tails and bridges (Hibbard et al. 1994, Hibbard & Mihos

1995, Barnes 2011).

In order to obtain the velocity of tidal tails we can use different velocity tracers. Velocities of stars are usually ideal to match with test-particle and collisionless self-consistent simulations. We can assume that stars had enough time to redistribute as collisionless particles, if the stellar population is formed long before the dynamical time. Nonetheless, measuring the velocity of stars in the faint tidal tails and bridges requires a high signal to noise ratio in the continuum of spectra. Another option is to measure the velocity of cold neutral hydrogen gas (21 cm HI emission). Neutral hydrogen is usually more extended than stars in disc galaxies, and produces stronger tidal features when discs interact in prograde orbits which can be useful for dynamical modeling. However, one should keep in mind that cold gas is dissipative. Dissipative structures are produced in chaotic processes, and it is hard to reproduce them even in hydrodynamical simulations that include gaseous components. It is impossible to reproduce them with collisionless test particles of Identikit. (Mortazavi et al., 2016). The third option is to measure the velocity star forming regions using line emission (e.g. Hα). Galaxy mergers induce star formation in gas-rich disc galaxies, and one often finds H II regions in the tidal tails and bridges (Jog & Solomon, 1992; de Grijs et al., 2003). Measuring Hα emission is a lot less expensive than measuring the velocity of stars or the cold gas (HI). Nonetheless, gas dissipation also affect these regions. Besides, before using Hα as velocity tracer, we must make sure that the ionized gas resides with the bulk of baryonic matter and is not displaced in position or velocity through a non-dynamical phenomenon such as shock-driven gas by supernovae (SNe) or active galactic nuclei (AGN).

In this work we explore the effect of using different kinematic tracers on the measured encounter parameters. IFU galaxy surveys like SAMI (Croom et al. 2012), CALIFA (Sánchez et al. 2012), and MaNGA (Bundy et al. 2015) measure the resolved Hα kinematics of a relatively large number of galaxies, including major mergers. Consistency between modeling Hα kinematics and modeling the more extended HI emission shows that our method can be applied on the data from these large surveys. As a result, we will have dynamical models of statistically significant samples, and we can measure the distribution of orbital parameters of major galaxy mergers in the nearby Universe.

In this chapter, we focus on modeling one of the most famous galaxy merger systems, NGC 4676 (a.k.a. Arp 242, the Mice). NGC 4676 is an early stage galaxy merger at redshift z=0.02205. It has a very distinctive morphology consisting of two strong tidal tails in the north and south of the system resembling two playing Mice. The straight tail in the northern galaxy indicates that this galaxy is almost edge-on. The southern disc seems to be slightly tilted, though still close to an edge-on view. In this work, we model the Mice using the kinematics of two different components: cold gas (HI), and star-forming regions (Hα). In §2 we describe reduction and analysis of the SparsePak IFU data for obtaining the Hα kinematics of the Mice. In §3 we briefly mention the characteristics of the HI data. In §4 we describe the method we use for modeling the initial conditions of the Mice using both Hα and HI line-of-sight velocity maps, and we present the modeling results. In §5 we discuss these results, comparing them to some previous measurements in the literature and demonstrating some of the implications of the measurements.

3.2 SparsePak IFU Data

3.2.1 Hα and [N II]Observations

We observed the Mice using the the SparsePak Integral Field Unit (IFU) on the WIYN telescope at Kitt Peak National Observatory (KPNO)(Bershady et al. 2004) in March 2008. Our goal was to measure the kinematics of Hα emission line. We do not require a uniform coverage of velocity information over the system. Often, just the velocity of a few fibers in the a particular tail is enough to break the degeneracy in the merger parameter space. SparsePak is especially suitable for this purpose as it has a relatively large field of view ($\sim 1'$), at the expense of missing areas between the sparsely placed fibers. We observed the Mice with 4 SparsePak pointings. Figure 3.1 shows the layout of the fiber positions on the Mice.

For SparsePak observations we used the bench spectrograph and the 860 lines/mm grating blazed at 30.9° in order 2, obtaining a dispersion of 0.69 Å/pixel (FWHM) in the wavelength range of 6050-7000Å. We obtain a velocity resolution of ~ 31 km s^{-1}. Our spectral coverage is less than current and ongoing galaxy surveys such as

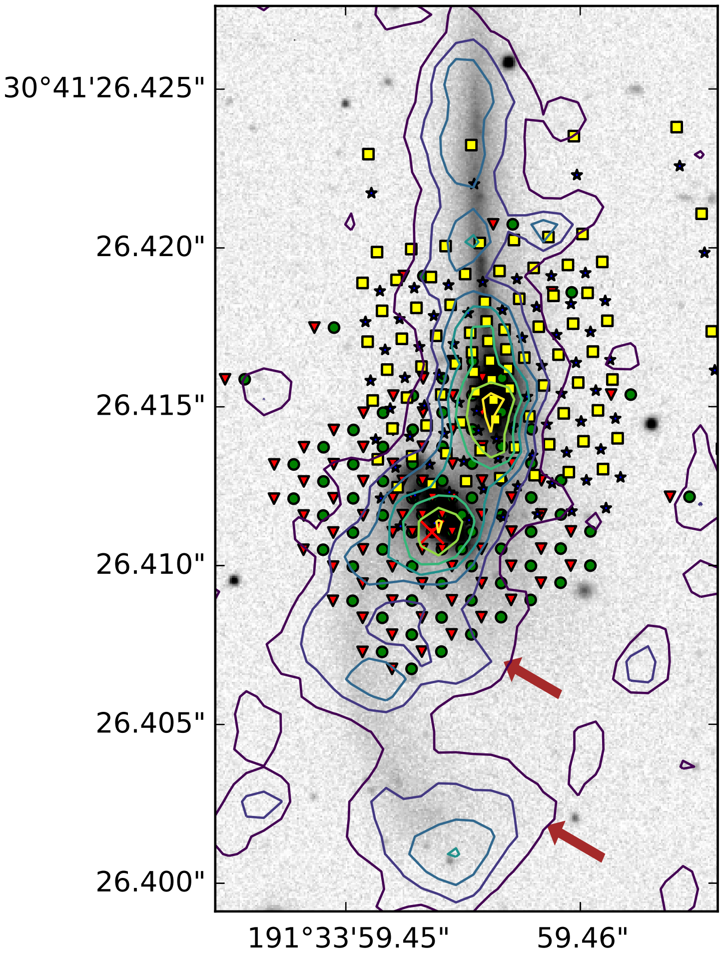

Figure 3.1: The HI surface density contours are plotted over the SDSS r-band image. Sky positions of the fibers in four SparsePak pointings are shown separately, with green circles, red triangles, blue stars, and yellow squares. The red cross indicates the fiber for which the spectrum is shown in Figure 3.2. The centers of the two galaxies and the northern tail match in r-band image and HI map. The southern tail, however, seem to be generating two self-gravitation clouds of cold gas (indicated by the brown arrows). These self-gravitating features can not be reproduced with test-particles in Identikit. We use the morphology of the r-band image along with the kinematics of the HI gas.

CALIFA, and MaNGA, But our spectral resolution is higher. In the red band, the dispersion of CALIFA, and MaNGA surveys are 2.0 Å/pixel and 0.83Å/pixel, respectively. Higher spectral resolution enables us to resolve multiple emission line components, usually appearing in the central regions of galaxies where multiple gaseous components overlap.

3.2.2 Data Reduction

We fit 1 component and 2 component triple Gaussian curves on top of a line with free slope as the background (continuum) over the wavelength range 6665-6755 $\AA$ where Hα and [N II]emission lines reside for the Mice system. The triple Gaussians are three Gaussian curves with centers separated by the wavelength difference between [N II][λ6548], Hα [λ6563], and [N II][λ6584]. The signal to noise of the continuum is not high enough to fit the stellar model properly. However, in our analysis we take the underlying Hα absorption into account. We use an F-test to decide which fit to emission lines is favored by our data. Two component fits are usually preferred in the central regions where the signal to noise is higher and pieces of the system with different kinematics are likely to overlap. Figure 3.4b shows fibers in which double components fits were favored. In each of these fibers, narrow and broad components are determined by their velocity dispersion. In some of the very central fibers even a 2 component fit is not enough to properly model the shape of the emission line. Figure 3.2 shows an example of a fiber where a 3 component model looks more appropriate.

This fiber is marked with the red cross in Figure 3.1. In Figure 3.2b we compare the CALIFA spectrum of the exact same location on the Mice. The multiple components are clearly washed out due to lower spectral resolution.

3.2.3 Shocked vs. Star Forming Regions

Hα emission originates from ionized gas regardless of how the gas was ionized. In the HII regions, atomic hydrogen is photo-ionized by the UV emission from O/B stars. Photoionization does not significantly affect the overall kinematics of the gas relative to the stars and the neutral gas they reside in. Because of this, we expect the velocity obtained from Hα emission from photo-ionized sources to be relatively similar to the dynamical velocity of the bulk of the baryons. This would be an ideal kinematic tracer for modeling the dynamics of the galaxy merger. On the other hand, high speed stellar winds, SN remnants, and feedback from Active Galactic Nuclei (AGN) produce shocks and heat up the interstellar gas. Shock-heated gas also emit Hα , but unlike photo-ionized gas, it often acquires a different velocity through a non-dynamical process. The kinematics obtained from this Hα emission can significantly disagree from that of the bulk of the baryons. Therefore, it is important to distinguish emission from the photo-ionized and shocked regions.

To separate the star-forming and shocked regions, one usually looks at the Baldwin, Phillips & Terlevich (BPT) diagram which uses [O III]λ5007 / Hβ, [N II]λ6583/Hα , [S II]$\lambda\lambda$6716, 6731/Hα , and [O I]λ6300/Hα flux ratios (Baldwin et al. 1981, Kewley

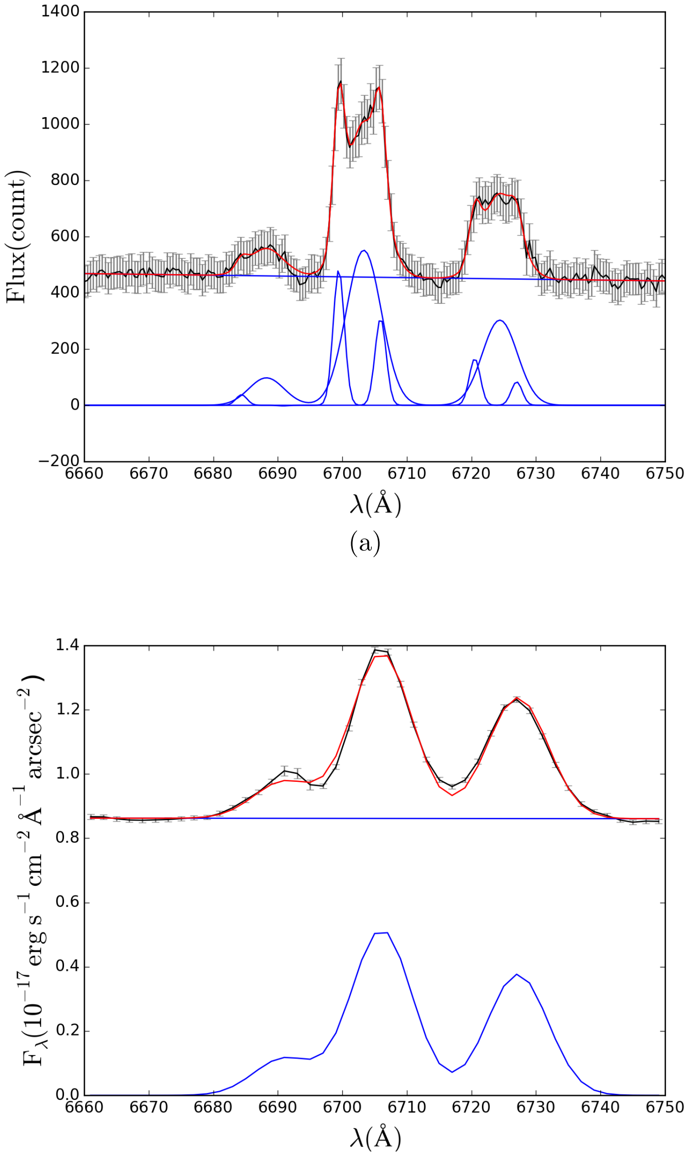

(a)

(b)

Figure 3.2: (a) An example of the SparsePak spectrum in one of the central fibers (indicated with the red cross in Figure 3.1). The black points with error bars show the spectrum data points. The solid blue curves show the fitted triple Gaussians (three components) and the the fitted background line. The red solid line shows the sum of fitted functions. One can visually confirm that more that one or even two components are visible in the emission lines. In this work, we test whether two components are resolved in each fiber. (b) CALIFA spectrum from the exact same sky position. The points and solid lines are the same as (a). The lower spectral resolution of CALIFA instrument washes out the multiple components.

et al. 2006b). Our SparsePak observations, however, were limited to wavelength range of 6050-7000Åand did not include Hβ and [O III] emission lines. Our SparsePak data requires a different method to separate the emission from shocked gas and normal star-forming regions.

The shocked regions tend to have both higher [N II]/Hα and usually exhibit higher velocity dispersion. Rich et al. (2011) showed that the histogram of velocity dispersion of emission line components of their high spectral resolution IFU data of some galaxy mergers reveals a bi-modality. They conclude that components with $\sigma < 90$ km/s are emitted from HII and turbulent star forming regions, and components with $\sigma > 90$ km/s are emitted from low velocity shocks. Combining their result with traditional BPT diagrams, we used a plot of [N II]/Hα vs. the velocity dispersion to separate the shocked regions from normal star forming ones.

Figure 3.3 shows the plot of [N II]/Hα vs. velocity dispersion for all kinematic components with S/N>3. From visual inspection, we find that the data points are generally grouped into three groups. Group 1 has low [N II]/Hα and low velocity dispersion, group 2 has high [N II]/Hα and high velocity dispersion, and group 3 has low [N II]/Hα and high velocity dispersion. The dividing lines used are shown in the figure. In Figure 3.3 we also show in dashed blue lines, $\sigma = 90$ km/s (limit of shocks in Rich et al. 2011) and [N II]/H$\alpha = -0.2$ (limit of composite galaxies in standard BPT diagrams; Kewley et al. 2006b). In our spectral analysis we did not fit the stellar model to the spectra, and we used a line with free slope to model the

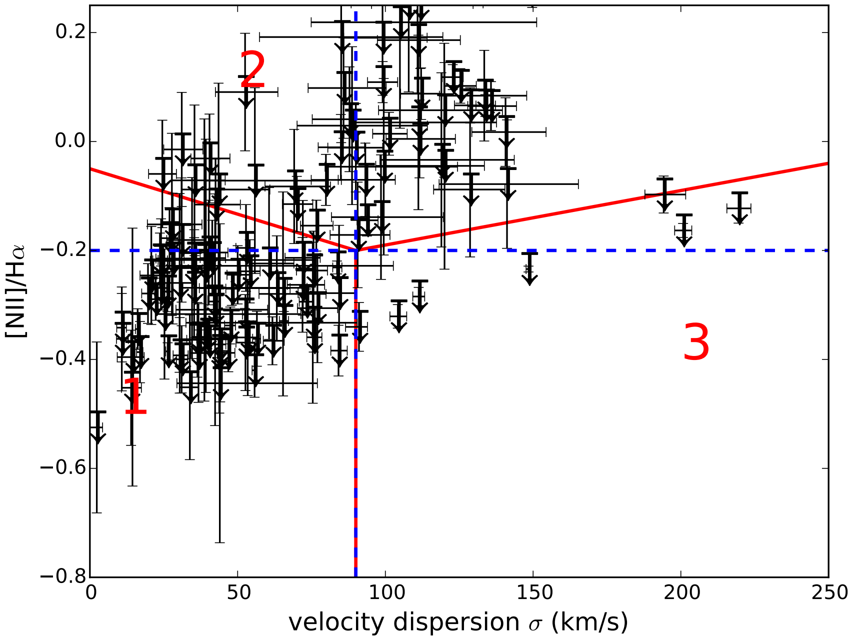

Figure 3.3: Plot of [N II]/Hα vs. velocity dispersion for all components with S/N>3. The downward arrows indicates that the value of [N II]/Hα is an upper limit. We did not take the underlying Hα absorption into account. (See text.) Data points are visually classified into 3 groups. Group 1 (lower left) are taken as components emitted from normal star-forming regions. Group 2 (top) have higher [N II]/Hα and velocity dispersion than group 1. They are likely to be emitted from shock-heated gas. Group 3 (lower right) have large velocity dispersion and lower [N II]/Hα than group 2 suggesting projection of multiple unresolved components. The vertical and horizontal dashed blue lines show respectively the limits of $\sigma = 90$ km/s and [N II]/H$\alpha = -0.2$ for shocked regions in the literature. (See text)

continuum around Hα -[N II]triplet. We did not take the underlying Hα absorption feature of the stellar continuum into account. This means that The Hα equivalent width (EW) is underestimated in our analysis, and [N II]/Hα is overestimated. As a result, the data points in Figure 3.3 are upper limits.

Group 1 components are taken to be the components originating from normal star forming regions. We use these components to make the Hα velocity map for dynamical modeling. (See Figure 3.4a). Most of the components in this group are both below and to the left of the horizontal and vertical dashed blue lines, respectively. The rest, are within the error-bar distance to these lines. The smooth rotation seen in circles in Figure 3.4a confirms the choice of these components as the velocity of star forming regions.

Group 2 components are emitting from the shocked regions. The spatial position of these components are shown in Figure 3.4c. They lie on the two sides, above and below the discs near the cores of both galaxies, which is consistent with the bi-cones of shocked material in Wild et al. (2014). This suggests that the process producing the shock-ionized gas is happening in the core of the galaxies, which can be merger induced central star-burst or AGN. Wild et al. (2014) argue based on the distribution of [O III]/Hα ratio and the X-ray observations, that NGC 4676A do not have an AGN and source of ionization is fast outflowing shocks. In NGC 4676B they do not rule out the possibility of an AGN being the source of bi-conal structure. The agreement of the spatial distribution of regions with high [N II]/Hα between our data and CALIFA analysis, for which stellar model is taken into account, suggests that the underlying Hα absorption does not significantly change our measurements of [N II]/Hα .

Figure 3.4d shows the spatial distribution of group 3 components. They are in the central regions and, their high velocity dispersion can be explained by projection of more than 2 components that are not resolved.

Using these groups, we can estimate the fraction of total Hα flux emitted from shocked gas. To do so, we divide the sum of the Hα flux from group 2 components to the total Hα flux. Group 3 components can be both unresolved group 1 and 2 components. We use [N II]/Hα $= -0.2$ limit to separate them for the purpose of this estimate. We obtain a fraction of 23% of Hα flux being emitted from shock-heated gas.

3.3 JVLA HI data

The kinematics of cold gas are available from radio interferometric observations of HI 21 cm emission line performed by Hibbard & van Gorkom (1996a). The observations took place in May of 1991 and May of 1992 using the D and C configurations of then Very Large Array (VLA), respectively. The HI data has a spatial resolution of 20" ($\approx$ 9 kpc) and velocity resolution of 43.1 km/s. The total HI mass is in the system is $7.5 \times 10^9 M_\odot$ (Hibbard & van Gorkom 1996a and Wild et al. 2014) [There is a discrepancy between the two, even though Wild et al. is citing Hibbard's paper!!!].

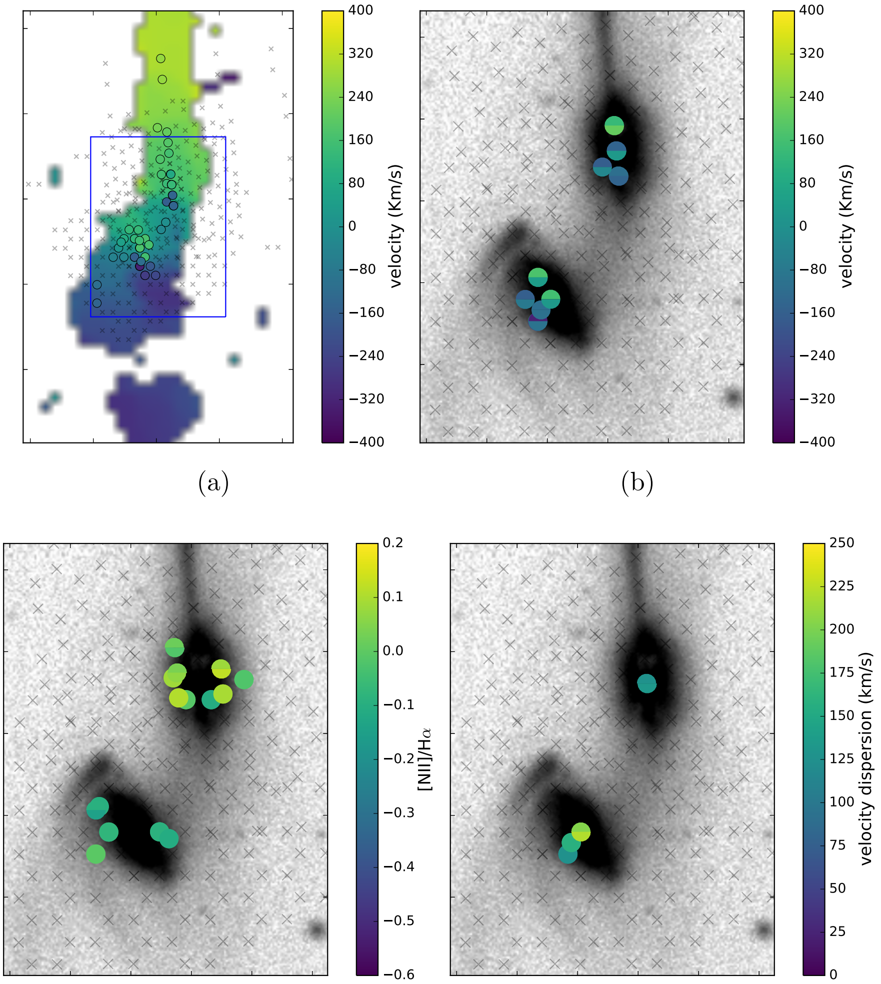

(a) (b)

(c) (d)

Figure 3.4: (a) Velocity of components in group 1 of Figure 3.3, which have low velocity dispersion and low [N II]/Hα , is over-plotted on the HI Velocity map. There is an excellent agreement in the overall velocity gradient and the velocity of tidal tails. The blue box shows the zoom-in area of the other panels. (b) The fibers in which two component fit is preferred by the F-test over one component fit. The velocity of the two components are shown by the color map. The upper half of the circles show the velocity of the narrow components, and their lower half show the velocity of the broad components. (c) The fibers with components in group 2 of Figure 3.3. The spatial distribution of this fibers is consistent with the bi-cone shocked structure seen in Wild et al. (2014), and suggests a central process is responsible for shocks. (d) The fibers with components in group 3 of Figure 3.3. These components have large velocity dispersion and low [N II]/Hα . The color of points show their velocity dispersion. They are in the central regions where multiple gaseous component are projected in the same line of sight. Note that the broad component in the spectrum of Figure 3.2 belongs to this group.

In the Mice, there is a couple of self-gravitating blobs in the southern tail which do not have counterparts in the optical r-band image. (They are indicated by the brown arrows in Figure 3.1.) After a few trials, similar to Privon et al. (2013), we decided to use the morphology of the r-band SDSS image along with the velocity of the HI gas.

3.3.1 Kinematics of Hα vs. H I

We use the kinematics of the Hα emission from normal star-forming regions for modeling the dynamics of the Mice. Figure 3.4a shows the Hα velocity map the mice galaxies over-plotted on the H I velocity map. In this color plots the striking agreement between the two velocity maps is evident. This agreement is especially important in the tidal tails which play the most important role in dynamical modeling, as we try to find the model that best matches the morphology and kinematics of the tidal features.

3.4 Dynamical Modeling

For dynamical modeling of the Mice, we use the automated pipeline that we developed based on Identikit (Barnes & Hibbard 2009; Barnes 2011). Identikit is a software package for modeling the initial condition of major galaxy mergers. It uses a precompiled library of N body simulations of galaxy mergers with different initial conditions. The discs are modeled by test particles. This facilitates the run of multiple discs at the same time, and improves the pace of search in the parameter space. Interactive visual matching with Identikit was used by Privon et al. (2013) to model the mice along with 3 other systems.

The isolated galaxies consist of collisionless massive and massless test particles. massive particles are distributed in spherically symmetric fashion representing the masses of the dark matter halo, the disk, and the bulge. In these models, the luminous mass fraction, $f_L = (M_d + M_b)/(M_h + M_d + M_b)$ is 0.2 and the concentration parameter of the halo mass profile, c_h is 4. The discs are represented by test particles that are initially in circular orbits. The scale length of the disc , a_d, is 1/3 of the scale radius of the dark matter halo, a_h. Barnes (2016) explored the effect of different structure parameters in the isolated galaxies on the morphology of tidal features. In this work we keep working on a single mass model for the sake of simplicity.

In this work we use an automated matching feature that is introduced in Identikit II (Barnes, 2011). In Identikit II, the similarity between model and data is quantified with an informal measure called score. The user places small boxes in the same position as the tidal tails and bridges of the system, extended in two spatial directions and one velocity direction (LOSV). Identikit calculates the scores based on the number of disc test particles residing in these phase space boxes. The models that better reproduce the tidal features in the data will place more particles in these boxes, and they will gain a better score.

In Chapter 2 we describe the method that we have developed for automated searching of parameter space and measuring the initial conditions with robust uncertainties. In this method we first put the boxes on tidal features of the galaxy merger using a semi-automated technique. The boxes are placed randomly in regions that are far enough from the center of galaxies. Boxes near the center of the galaxies, where test particles have higher number density, are always populated, and they do not put strong constraint on the initial conditions of the merger. So, we put the boxes over the ends of the tidal tails to enforce the similarity in the overall shape and the velocity gradient. We ignore self-gravitating features like stellar clusters or blobs of gas, because test particles in Identikit cannot reproduce these features. In cases where no velocity information is available (e.g. the absence of Hα in the southern tail of the Mice), we put boxes that are only extended in spatial directions, and do not put constraint on velocity. The size of the boxes are selected to match the spatial resolution of the observation. In case of the HI data The boxes are 8 kpc wide, almost matching the spatial resolution of JVLA observation of Hibbard & van Gorkom (1996a). When modeling the Hα kinematics, the size of the boxes where set to be close to the size of SparsePak fibers (4 kpc). However, in places where the error in Hα velocity measurement was larger that the extent of the box in velocity direction, we increased the size of the box proportionally.

Table 3.1 shows the range of encounter parameters we explored in this work. We produced a library of Identikit models with a variety of eccentricity, pericentric separation, time since first pass, velocity scaling and velocity offset. For future references we call these five parameters ”external parameters”. Calculating the score for each of these models, Identikit constrains viewing angle, initial orientation of discs, length scaling and position offset. We call these parameters “internal parameters”. By calculating the score for all library members, we obtain a 5 dimensional score map for external parameters. Each point of this score map corresponds to a set of calculated internal parameters. The model with the maximum score is the best-fit model and the corresponding external and internal parameters are the measured best-fit encounter parameters

The uncertainty of the best-fit parameters are calculated using a Monte Carlo statistical technique. Score, by itself, does not provide statistical probability, as fit goodness measures like χ^2. So, in order to measure the uncertainty of the scores we re-do the random box positioning procedure described above several times and calculate the score each time. This process randomly moves the position of boxes on the tidal tails and bridges of the system. The variation in the scores for each model measures the error of the score, which eventually, translates into the uncertainty of the measured best-fit parameters. The models with scores that are within 1, 2, or 3 standard deviation from the best score, respectively determine the extent of 1σ, 2σ, or 3σ separation in the parameter space from the best-fit model.

In Chapter 2 we showed that when applying our modeling method on young stars of an edge-on prograde merger simulation (similar to Hα data of the Mice) the average

Parameter Class	Parameter	Range Tested
orbital parameters	eccentricity	[0.80-1.10]
	pericentric distance	[0.03125-1.0000]$\times R_{vir}$
	mass ratio	1
observer dependent parameters	time since pericenter	from first pass to second pass
	viewing angle	viewed from 320 evenly distributed
	position	directions over a sphere
	length scaling $\mathcal{L}$	set by viewing angle and locking the centers
	velocity offset	[-0.1,0.1]
	velocity scaling $\mathcal{V}$	[-0.500-+0.500]*
initial orientation of discs		1280 evenly distributed orientation

Table 3.1: Range of encounter parameters explored. * The velocity scaling $\mathcal{V}$ relates the dimensionless velocity in Identikit to the physical velocity.

bias is not significant in eccentricity, R_{peri}, and merger stage ($< 1\sigma$). When testing the cold gas of the same simulation the measured R_{peri} was almost twice the correct value.

3.4.1 Summary of Results

In Figure 3.5 one can see the 3 slices of the 5 dimensional score map through the best fit parameters, across eccentricity, pericentric separation, and Merger stage. In these plots the best-fit model can be compared with the model preferred by Privon et al. (2013). The best fit eccentricity is $0.90\pm^{0.05}_{0.05}$ in HI modeling. In Hα modeling, however, the best fit eccentricity is 0.80 which is the limit of the range explored. So, we report the eccentricity measure to be $< 0.80\pm^{0.25}_{\_\_\_}$. The best-fit pericentric separation is $16.8\pm^{11.4}_{7.3}$ kpc for Hα modeling, and is $19.9\pm^{10.4}_{13.7}$ kpc for HI modeling. The merger stage measured as the time since pericenter divided by the time from first passage to second passage, is $0.21\pm^{0.10}_{0.11}$ and $0.13\pm^{0.30}_{0.03}$ for Hα and HI modelings, respectively. The best-fit time since pericenter is $210\pm^{50}_{40}$ Myrs for Hα and $180\pm^{50}_{40}$ Myrs for HI. The best viewing polar angles (θ) relative to the orbital plane is $-77°$ and $-70°$ for Hα and HI modelings, respectively. Figure 3.5 shows the general consistency between the two models and the model of Privon et al. (2013). We discuss some of the details in §3.5.

	fractional $R_{peri}(R_{vir})$	physical R_{peri} (kpc)	e	merger stage $\Delta T/T_{\text{first to second pass}}$ *	physical time (Myr)	(θ, ϕ)
Hα	$0.44\pm^{0.34}_{0.30}$	$16.8\pm^{11.4}_{7.3}$	$< 0.80\pm^{0.25}_{---}$	$0.21\pm^{0.10}_{0.11}$	$210\pm^{50}_{40}$	$(-77°, 0°)^*$
HI	$0.22\pm^{0.25}_{0.19}$	$19.9\pm^{10.4}_{13.7}$	$0.90\pm^{0.05}_{0.05}$	$0.13\pm^{0.30}_{0.03}$	$180\pm^{50}_{40}$	$(-70°, -50°)^*$

Table 3.2: Measured parameters from modeling Hα and HI. * The error of measurement of viewing angle is about 20°. This value depends on the resolution of search in viewing angle in Identikit (viewdepth parameter = 3 in Identikit; see Barnes 2011), and also the width of distribution of viewing angles in models with high score.

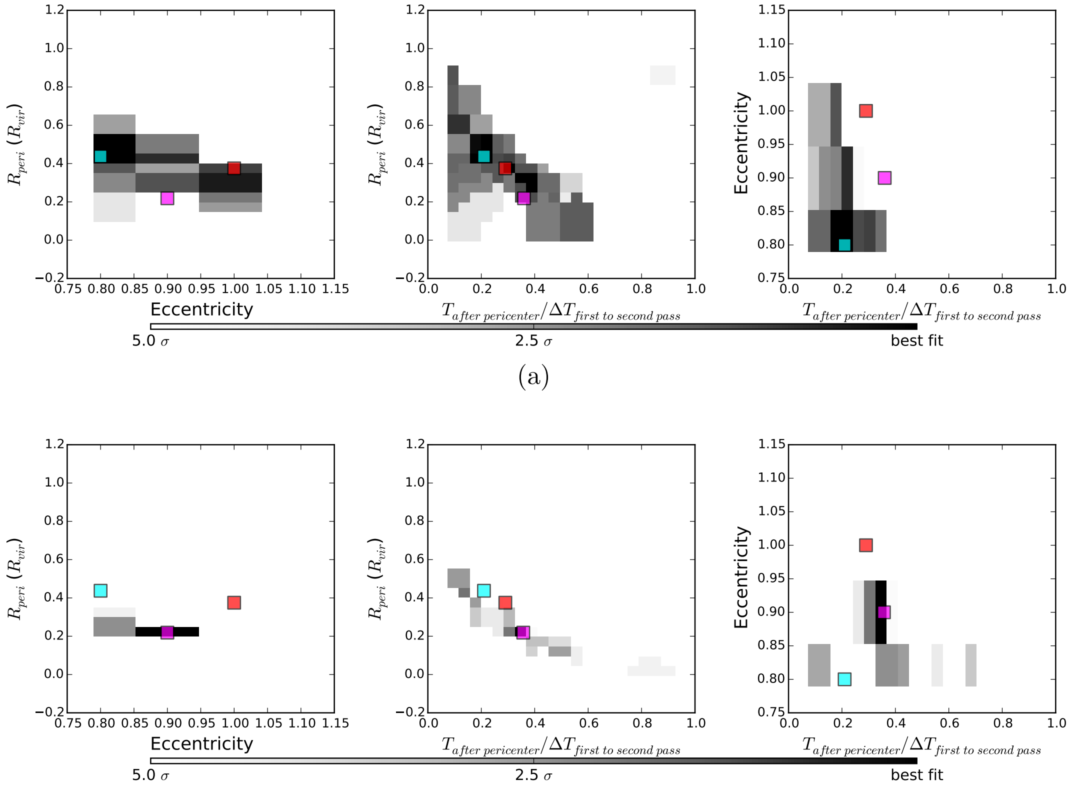

(a)

(b)

Figure 3.5: (a) The average score map for modeling Hα kinematics of the Mice galaxy merger. score map is 5-dimensional parameter space. Here we are showing 3 slices of the score map, through the best-fit parameter, across eccentricity, pericentric separation, and time since pericenter. The dark areas show better score. The gray color is scaled with the standard deviation of scores in the best-fit model. The best fit model, which as the maximum average score, is indicated with the cyan box. The red box shows the parameters of Privon et al. (2013) which used visual matching to HI kinematics. The magenta box shows the best-fit parameters of the HI model. (b) The average score map for modeling HI kinematics of the Mice. Colored squares are the same as (a)

3.5 Discussion

The peculiar morphology of the Mice has made it a curious case for dynamical modeling. There has been several attempts to model the initial conditions of this system. The measured parameters in some of these attempts are shown in Table 3.3. In all but one of these dynamical models the mass ratio is presumed to be 1. This assumption is because of the stellar mass(light) ratio (1.5:1, from Wild et al. 2014) and the strong tidal tails in both galaxies (Toomre & Toomre 1972; Barnes 2016). Similar to the previous models we adopted equal mass merger models in this work.

Holincheck et al. (2016) uses judgement of citizen scientists (Galaxy Zoo, Lintott et al. 2010) to match only the morphology of a relatively large sample of merger systems. lack of kinematic information in this analysis contributes to the large error-bars in the measured parameters.

Time since first pericenter is similar in most of these models. Among the measurements mentioned in this work, the lowest value is 120 Myr for Toomre & Toomre (1972). The largest is 430 ±190 Myr for Holincheck et al. (2016), and the median is 175 Myr for Privon et al. (2013). Our measurements from HI and Hα modeling are both consistent with the median of these models. This suggests that the measurement for time since pericenter is the most robust measurement among other encounter parameters.

In both of our models the Mice is measured to be at a relatively early stage. merger stage is about 1/5 and 1/8 of time from the first passage to the second passage for

dynamical model	μ	e	R_{peri} (kpc)	physical time since pericenter (Myrs)	kinematics
Toomre & Toomre (1972)[1]	1.0	0.6	...	120	Hα only centers
Mihos et al. (1993)[2]	1.0	0.6	23	180	Hα long slit
Barnes (2004)[3]	1.0	1.0	8.9	170	HI map*
Privon et al. (2013)[2]	1.0	1.0	14.8	175	HI map*
Holincheck et al. (2016)[1]	0.59±0.52	0.70±0.27	15.9±5.0	430±190	no velocity used

Table 3.3: Previous dynamical models of the Mice. * From Hibbard & van Gorkom (1996a). [1] Test particles with central potential. [2] Collisionless self consistent simulations. [3] Hydro simulations including gas and star formation.

Hα and HI modeling, respectively. Taking the error-bars into account, these are consistent with Privon et al. (2013) ($\approx 1/4$). Our Hα and HI models predict that the second passage will occur in $800\pm^{700}_{200}$ Myrs and $1200\pm^{100}_{900}$ Myrs, respectively, while in the Privon et al. (2013) model it will happen in ≈ 400 Myrs.

[This paragraph needs improvements] Both of our models prefer elliptical orbits, which is more consistent with Toomre & Toomre (1972) and Holincheck et al. (2016). Nonetheless, in Chapter 2, we showed that our method underestimates the eccentricity by 0.1 in some tests with parabolic orbits.

Physical pericentric distance in our Hα and HI models are $16.8\pm^{11.4}_{7.3}$ kpc and $19.9\pm^{10.4}_{13.7}$ kpc which are consistent with all previous measurements. R_{peri} is hard to constrain, as its effect on morphology is correlated with disc scale-length and halo scale-radius. Besides, in Chapter 2 we showed that our method overestimates R_{peri} in most of the tests on GADGET simulations, suggesting that the correct value of R_{peri} for the Mice is lower than our measurements in this work.

[Our measured parameters are more different than Barnes (2004) with the new results, I am not sure if I should keep this paragraph] In order to predict what the remnant of the Mice will look like we used a GADGET simulation from Cox et al. 2006b which has similar encounter parameters as that of Barnes (2004). The isolated galaxies are identical Sbc-type consisting of dark matter, stars, and gas particles. The disc scale length is $\approx 1/4$ of the halo scale radius. The simulations model radiative cooling, density-dependent star formation that reproduces Kennicutt-Schmidt relation (Kennicutt, 1998), and the effect of supernovae feedback and stellar winds. Feedback from active galactic nuclei is not included. In this model the remnant is an elliptical galaxy with a relatively large ellipticity (≈ 0.8 for stars). We calculated the λ parameter to be (≈ 0.27) which lays in the boundary of fast-rotator vs slow-rotator division by the ATLAS3D criterion. (Emsellem et al. 2011; see Figure 19 in Lotz et al. 2008)

The strong tidal tails and the edge-on view of the Mice makes it an straightforward case for testing a galaxy merger model. However, one may ask how common the encounter parameters of the Mice are among other galaxy mergers. While the answer to this question requires modeling a larger sample of mergers, we can compare our measured values with the distribution of orbital parameters of dark matter halo mergers in cosmological simulations. The measured eccentricity of the Mice ($e = 0.90$ $e = 0.80$ for Hα and HI models, respectively), seems to be lower than the most frequent eccentricity ($e = 1.0$) among dark matter halo mergers (e.g. see Figure 11 of Benson 2005 and Figure 6 of Khochfar & Burkert 2006). Parabolic ($e = 1$) orbits have zero total mechanical energy, and are expected if the protogalaxies are initially at rest, and far from each other. The pericentric separation measurements for the Mice ($0.44\pm^{0.34}_{0.30}$ R$_{vir}$ and $0.22\pm^{0.25}_{0.19}$ R$_{vir}$ for Hα and HI, respectively) are both uncertain. Their ranges covered by their uncertainty both fall into the most common values in the distribution of R$_{\rm peri}$s of in dark matter halo mergers of the Millennium cosmological simulation (see Figure 4 of Khochfar & Burkert 2006).

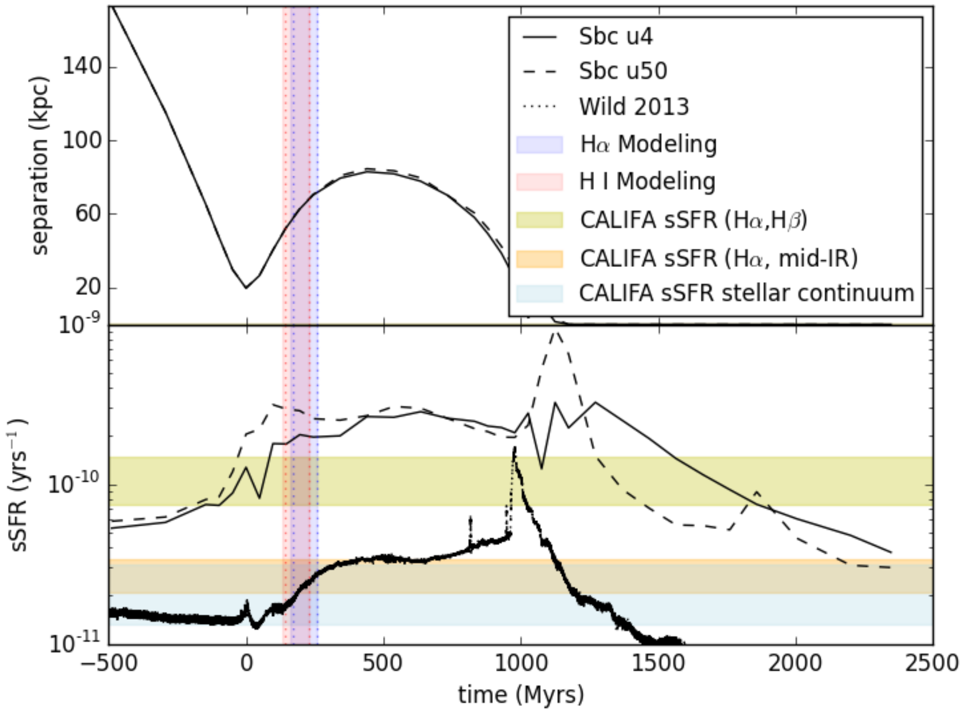

Figure 3.6: Top shows the separation between the nuclei of the two galaxies in the GADGET SPH simulation of galaxy merger described in the text. This simulation has similar initial conditions as that of the Mice galaxy merger. The observed merger stage for HI and Hα modelings are shown with the blue and red vertical shaded areas. Below shows the specific star formation rate as the function of time in the GADGET simulations with two different feedback recipes. (See Cox et al. 2006b) along with star formation in the model used in (Wild et al., 2014) . Three different measurements of specific star formation rate are shown as horizontal shaded areas (Wild et al. 2014).

3.5.1 Star Formation in Hydrodynamical Simulations

Hydrodynamical simulations have shown that the merger induced star formation rate (SFR) is affected by the encounter parameters. Cox et al. (2008) show that mergers with larger pericentric distance induce starbursts at later times. Moreover, the relative inclination of the discs with respect to orbital plane correlates with the total amount of merger induced star formations (also see Snyder et al. 2011). The star formation in these simulations also depends on presumptions about sub-grid physics, the physical processes that happen in scales smaller than simulations resolution. Even the most recent simulations of galaxy formation do not yet resolve particles at scales smaller than stars. To implement star formation, most current simulations assume a density threshold above which stars are formed. The exact value of this threshold is different in different simulations and partly depends on the resolution of the hydrodynamical simulation (cite alyson brooks), but they are usually calibrated to reproduce the Kennicutt-Schmit relationship between gas mass surface density and star formation rate Kennicutt (1998). However, Barnes (2004) showed that one needs to go beyond a simple density threshold recipe for star formation in order to find extended star formation as is observed in the northern tail of the Mice. He proposes a shock-induced star formation recipe that makes a more realistic distribution of star formation. In addition to the freedom in the star formation recipe, the model for feedback from SNe, stellar winds, and AGN adds to the complications of star formation model in hydrodynamical simulations (Cox et al., 2006b; Oppenheimer et al., 2010). Finding independent constraints on star formation history in galaxy mergers enhances our understanding of the sub-grid physics in hydrodynamical simulations.

Our estimate of the merger stage and other encounter parameters of the Mice is independent of star formation rate and only depends on the dynamics of tidal features. As a result, by looking at a "Mice-like" simulation of a galaxy merger with the same encounter parameters and at the same time step that we measured in this work, we can put an independent constraint on the model of merger induced star formation. This provides a powerful tool for adjusting the degrees of freedom in the recipes for star formation in the hydrodynamical simulations.

Figure 3.6 shows specific star formation history of a couple of simulations which have encounter parameters similar to that of the Mice. It also shows a few measurements of the specific star formation rate in the Mice. For one of these simulations, the star formation from two different feedback recipes are shown. These models are relatively old, and we only show them to demonstrate how the tool of dynamical modeling can be utilized for better understanding of star formation.

Unfortunately, the measurements of the SFR in the Mice is uncertain and depends on the observed star formation indicator. In Figure 3.6, we compare three SFR measurements from Wild et al. (2014). The SFR derived from ionized gas recombination lines (Hα and Hβ) is significantly higher than the one derived from modeling the stellar continuum. While the difference may be an indicator of very recent star formation, in §3.2.3 we showed that about 25% of the line emission arises from sources other than photoionization. In addition large amounts of dust attenuation, particularly at the centers of the galaxies, introduce large uncertainties in star formation rate measurements. The edge-on view of the discs may play a role in worsening this problem. Figure 3.6 demonstrates how improvement in the measurements of star formation and dynamical merger stage can constrain the recipe for star formation in hydrodynamical simulations.

summary

In this Chapter we modeled the initial conditions of the Mice galaxy merger system, utilizing an automated method based on Identikit software package. We observed the Mice with the SparsePak IFU on the WIYN telescope at KPNO, considered one- and two-component emission lines, and separated the emission from photo-ionized regions and shocked regions using a plot of [N II]/Hα vs. velocity dispersion.

We used the kinematics of both photo-ionized gas (Hα) and cold gas (HI) to compare the effect of using different kinematic tracers. We found similar results for the two kinematic tracers, both qualitatively consistent with previous models for the Mice. This work suggests that this method of dynamical modeling is applicable to some other major galaxy merger systems using both HI and Hα velocity information in the tails and bridges. Though, one should be aware that in some mergers systems gas does not follow stars on large scales due to processes like ram pressure striping. (See Chapter 4.) We can use data from IFU surveys (e.g. MaNGA, SAMI, etc.) and high resolution HI surveys (e.g. MeerKAT) to model the dynamics of major galaxy mergers.

We also demonstrated how dynamical measurement of merger stage can put independent constraints on the models of star formation rate in hydrodynamical simulations of galaxies. This was not possible for the Mice system, mostly because of the uncertainty star formation rate measurements.

Chapter 4

Dynamics and Shocks from Hα Emission of Nearby Galaxy Mergers

In this Chapter, we examine the dynamical properties of interacting galaxies, and properties of shocked gas produced as a result of interaction, using integral field unit (IFU) observations of Hα emission line. We observed 22 galaxy mergers using the SparsePak IFU at Kitt Peak National Observatory (KPNO) between March of 2008 and May of 2013.[1] Our sample consists of major and minor galaxy mergers with mass ratios $1 < \mu < 8$. Our goal is to obtain the velocity maps from the Hα emission lines over the entire luminous parts of the galaxies including the faint tidal tails,

---

[1] Observations in March 2008 was part of a different project by my advisor Dr. Jennifer Lotz before we started this project. She kindly provided the data for our analysis.

and to find extended shocks and outflows. We fit multiple kinematic components to the Hα and [N II]emission lines, develop an MCMC code to robustly measure the error of fit parameters, use the F-test to determine the best number of kinematic components for each fiber, and use [N II]/Hα and velocity dispersion properties to separate emission from star forming (HII) regions and emission from shock-heated gas. We use the Hα emission from HII regions to produce the velocity maps suitable for dynamical modeling. We used the method described in Chapter 2 to model the dynamics of galaxy pairs with mass ratio, $\mu \approx 1$. We also estimate fraction of shocked Hα emission, and examine the spatial distribution of shocks, looking for indications for the source of shocks. We find that shocked gas fraction in these merger systems correlates with the projected separation and light (mass) ratio. Close pairs have on average higher shock fraction than wide pairs. Coalesced mergers have the highest average shocked gas fraction. Also, pairs with more equal light ratio (i.e. stellar mass ratio) have higher shocked gas fractions. We put the first ever constraints on encounter parameters of one of the systems. Along with the Mice (modeled in Chapter 3) and few other systems in our sample with available dynamical models from the literature, we examined physical trends between shock fraction and encounter parameters. In our limited sample, we find that the orbital pericentric separation is correlated with shock fraction consistent with shocks being produced as a result the tidal impulse, or direct collision of ISMs at the first passage.

4.1 Motivation

Hα observations of a large sample of tidally interacting galaxies may be used to improve our understanding of the physical processes during the merger in several ways. In Chapter 3 we showed that Hα kinematics can be used to model the dynamics of the Mice galaxy merger. If we want to find the encounter parameters of a large sample of mergers, the easiest kinematic tracer to measure velocity of tidal tails is the Hα emission line. Additionally, Hα and [N II] emission lines contain valuable information indicating the source of ionization. We can use the velocity dispersion of emission lines and the [N II]/Hα ratio to separate emission of shock-heated gas from photo-ionized gas. We can measure what fraction of Hα flux is emitted from shock-ionized gas, and where the shocks are spatially located. Combining measurements of encounter parameters from dynamical modeling and shock detection provides a tool for investigating the physics of gas during galaxy interaction.

4.1.1 Shocked Gas and Merger Sequence

Hydrodynamical models of close encounters between 2 galaxies predict shocks (e.g. Barnes 2004). These shocks are often observed in the real Universe (Monreal-Ibero et al., 2010b; Rich et al., 2011). After the first passage, the inflowing gas may collide with the gas at lower radius, and at high enough velocities it may induce shocks. The gas that reaches the core triggers starburst and/or AGN, which creates strong outflowing winds. The outflows produce shocks as they blow into the gas clouds in the ISM. Moreover, collision of galaxies with certain geometries can result in fast encounter on gaseous clouds in the ISM of the two disks. This can also produce widespread shocks.

The chain of events behind all of the processes above generally begins after the first passage. The timeline of shock production after the first passage depends on the mode of shock production. Some processes that produce shocks are immediate, like the collision of gas clouds in a head-on encounter (e.g. in UGC 12918). Some will take a few to tens of Myrs to reach shock production. Central starburst or AGN-driven shocks produced by galactic superwinds are of this sort. We can put observational constraints on these processes, by inspecting the effect of merger stage on the amount of shocked gas.

Rich et al. (2015) uses a sample of 17 (U)LIRGS to show the relation of shock fraction and merger stage. They bin galaxies (mergers) based on their separation. They have 4 groups: isolated galaxies, wide pairs with separation between 10-100 kpc, close pairs with separation$<$10 kpc, and coalesced mergers. They removed unambiguous AGN hosts from their sample, and find that an increasing fraction of Hα is shocked by increasingly turbulence from isolated galaxies to late stage mergers.

However, projected separation of interacting galaxies does not necessarily represent the merger stage. An interacting pair of galaxies just after the first passage are as close to each other as a pair near coalescence. Also, two galaxies at large separation appear to be a close pair from certain viewing angles. In order to better constrain the merger stage, and other possible encounter parameters affecting shocks, we need a dynamical model of the merger system.

4.1.2 Dynamical Modeling

Dynamical modeling constrains merger stage and other encounter parameters (e.g. pericentric distance, eccentricity, etc.) by finding simulations that best reproduce the large scale structures such as tidal tails and bridges. Simulations that are used for this purpose are usually collisionless N-body simulations, because incorporating gas physics extensively increases the computational demands. One needs to run the simulations at least several times (often hundreds or even thousands of times) to find a good match between the model and data. Resultingly, less expensive collisionless simulations are preferred for dynamical modeling of disk galaxies. Collisionless stars, therefore, are the ideal component to match with these simulations. However, kinematics of stars are hard to measure in the faint tidal tails, as they requires high continuum S/N (See discussion in Chapter 1).

Another option is the cold neutral gas. Cold gas is usually more extended in the disks of isolated galaxies, and during disk interactions produce stronger tidal features. However, detecting cold gas using HI 21 cm emission line with high enough resolution requires long exposure times on large interferometers like JVLA, which is expensive. Hα emission, on the other hand, is relatively easy to measure for star forming galaxies even in low surface brightness regions. Galaxy mergers often induce star formation not only in the center, but also in the long tidal features (Jog & Solomon, 1992; Hattori et al., 2004; Whitmore & Schweizer, 1995; de Grijs et al., 2003). Star forming regions are often found in tidal tails and bridges. In Chapter 3, we showed that by proper separation of Hα emission due to star formation and other ionization sources we obtain very similar Hα and HI velocity maps for the Mice galaxy mergers (NGC 4676; see Figure 3.4a.)

In normal star forming regions, UV emission from young and hot stars photo-ionize the surrounding ISM, making Hα emitting sites known as HII regions. On the other hand, starbursts and supernovae (SNe) produce winds that can heat up the Interstellar medium (ISM) with shocks and produce Hα emission at velocities different from the bulk of the baryons in their vicinity (Sharp & Bland-Hawthorn, 2010). Moreover, colliding gaseous clouds of merging galaxies induce shocks in the ISM (Soto & Martin, 2012). Galaxy mergers can also trigger on enhance active galactic nuclei (AGNs) (Ellison et al., 2011) which produce outflows and spreads shocks (Wild et al., 2014). Shock excitation results in motion of the ionized gas that is not gained only by gravitational forces. Tidal features are only produced by gravity. We need to separate photo-ionized gas and shocked gas to get a robust measurement of the velocity map, proper for modeling tidal features.

With spatially resolved spectroscopy, we can distinguish spatial distribution and fraction of shocked gas. Rich et al. (2011) showed that velocity dispersion is a powerful tool to determine the shock and non-shock sources of ionization in nearby galaxies. This separation is not always possible by the optical line ratio diagnostic plots. Velocity dispersion can be used for this purpose only when data has high enough spectral resolution, and multiple kinematic components are fit to the emission lines.

In this Chapter, we present our WIYN SparsePak IFU observations for a sample of 22 galaxy merger, analysis of emission lines and shock detection, and dynamical modeling of one merger system. We examine correlation between encounter parameters and shocks. In §4.2 we describe the observational setup, the instrument, and target selection. In §4.3 we describe the data reduction producing the sky subtracted spectra and the error arrays. In §4.4 we present the analysis of emission lines including fitting multiple kinematic components and an MCMC code to measure the error of the fit parameters. In §4.5 we discuss how to separate emission from shocked gas and that from star forming regions, and measure contribution from different ionization sources to the total Hα flux. In §4.6.2 we present our attempts to model dynamics of equal mass mergers in our sample, and in §4.7 we discuss our results and implications of how merger encounter parameter affect merger-induced shocks. We present notes on individual systems in the Appendix.

4.2 Observations

We observed 21 galaxy merger systems[2] using the SparsePak Integral Field Unit (IFU) Bershady et al. (2004) on the WIYN telescope at Kitt Peak National Observatory (KPNO). The observations took place from March 2008 to May 2013 in five different observing runs which consisted of a total of 14 nights, with the dome being closed in 3 full nights and parts of some other nights due to precipitation, low dew point, or high wind. As our primary goal in these observations was to measure the kinematics of Hα and [N II] emission lines we observed in non-photometric conditions, and occasionally thin clouds were covering our targets during the observation. Resultingly, we did not attempt to flux calibrate our data.

4.2.1 The Instrument

The WIYN SparsePak IFU consists of a total of 82 sparsely packed grid of fibers each 4.687" in diameter, covering a Field of View (FoV) of 72"×71.3". Seven sky fibers are placed at $\approx 25''$ distance form the science grid on the north and east sides (Bershady et al., 2004).

SparsePak is especially suitable for the purpose of finding velocity maps for galaxy dynamical models, as it has a sparsely packed grid that covers a relatively large FoV. We do not require a uniform velocity coverage on the system. Rather, velocity information that provides the rotation near the center of the disks and the large scale

---

[2] Along with the Mice galaxy merger we analyze 22 systems in this Chapter

velocity gradient in the tidal tails is enough. Many of previous dynamical models have used HI velocity maps with much lower spatial resolution than is obtained with SparsePak (Hibbard & Mihos, 1995; Privon et al., 2013). In this work we found dynamical model for UGC 07593 with only a couple of fibers with velocity information at the end of the tidal tails. (See Figure 4.8.) Therefore, we obtained a single SparsePak pointing for each part of the system without dithering.[3] The slightly denser grid in the center of the SparsePak footprint helps us to put a better constraint on the rotation near the cores of the galaxies. For shock fraction measurements, however, full coverage is more desirable as we may miss regions with extensive shocks between the sparsely placed fibers. In additions, we put the center of Sparsepak pointing on the center of galaxies in most cases. The denser pack in the center of SparsePak introduces a bias in the galaxy-wide shock fraction toward the value near the center.

The bench spectrograph and 860 lines/mm grating blazed at 30.9° in order 2 was used, obtaining a dispersion of 0.69 Å/pixel(FWHM) in the wavelength range of 6050-7000Å. (R$\sim$4500, and velocity resolution of $\sim$30 km/s near the Hα line) Our spectral coverage is less than current and ongoing galaxy surveys such as CALIFA, and MaNGA. Our spectral resolution, however, is higher. In red band, CALIFA, and MaNGA surveys have resolution R of 850 and 3000, respectively. Higher spectral resolution enables us to resolve multiple emission line components, usually appearing in the central regions of galaxies where multiple gaseous components overlap.

---

[3] In some of the coalesced systems dithering was done for full coverage in order to find a better handle on the spatial distribution of outflows.

4.2.2 Target Selection

We used three different catalogues to find the merger systems that match our requirements. Our targets are chosen from the catalogue of isolated pairs of galaxies in northern hemisphere (Karachentsev et al., 1985), the Arp atlas of peculiar galaxies (Arp, 1966), and the *Galaxy Zoo* morphological classification catalogue (Lintott et al., 2010). In the *Galaxy Zoo* catalogue, we inspected galaxies with merger probability >0.5 to find proper candidates.

We looked for binary systems of interacting galaxies[4] with strong tidal features, because our primary goal was to use them for our dynamical modeling method. These are the features that are reproduced in test particle simulations like Identikit, and their shape is sensitive to the encounter parameters. Requiring strong tidal features introduces a selection bias to our galaxy merger sample. A prograde merging galaxy (for which the initial angular momentum of the disk is aligned with the orbital angular momentum) make larger tidal effects compared to retrograde merging galaxies (with anti-aligned disk). We have probably selected more prograde systems in our sample. In Chapter 2 we showed that prograde mergers are easier to model with our method

Targets are selected to have a FoV similar to that of SparsePak science grid (72"×71.3"). Most of observed systems and their tidal tails fit in two SparsePak pointings, one for each galaxy. A few smaller systems fit in one pointing and a few larger ones require three and four pointings. All of the systems analyzed in the Chap-

---

[4] Our sample includes three coalesced systems with strong tidal features suggesting that they have experienced a recent major merger.

ter and the SparsePak grid pointings are shown in Figure 4.1. Table 4.1 shows the sky position of the targets, observation date, redshift, number of SparsePak pointings, and exposure time on each pointing.

Most of the observed systems were in the footprint of Sloan Digital Sky Survey (SDSS). We required both galaxies in each system to have archival spectroscopic data near the center showing strong or medium Hα emission. By visual inspection, we also required the rest of the galaxies to have blue color, making them likely to host star forming regions. We estimated the continuum flux density near the Hα ($\lambda 6563 \AA$) line using the SDSS r band image (when available). The surface brightness in the faint tidal features our systems ranged from 8.4×10^{-19} to 3.8×10^{-18} erg s^{-1} cm$^{-2}\AA^{-1}$arcsec^{-2}.

4.2.3 Observation Setup

We used the surface brightness calculated from SDSS r-band image to determine the exposure time required for these observations. With r-band image we estimate the continuum level flux density near Hα line throughout the system. We planned to spend the exposure time required to achieve S/N$\approx$5 in the continuum in fibers laying on the tidal tails. However, we had bad weather conditions in some nights. Our goal was to get enough signal in the Hα emission, so in order to observe more systems in our limited time, we cut the exposure time when we could see strong Hα lines in outskirt fibers in the first couple of exposures. Table 4.1 show the number of

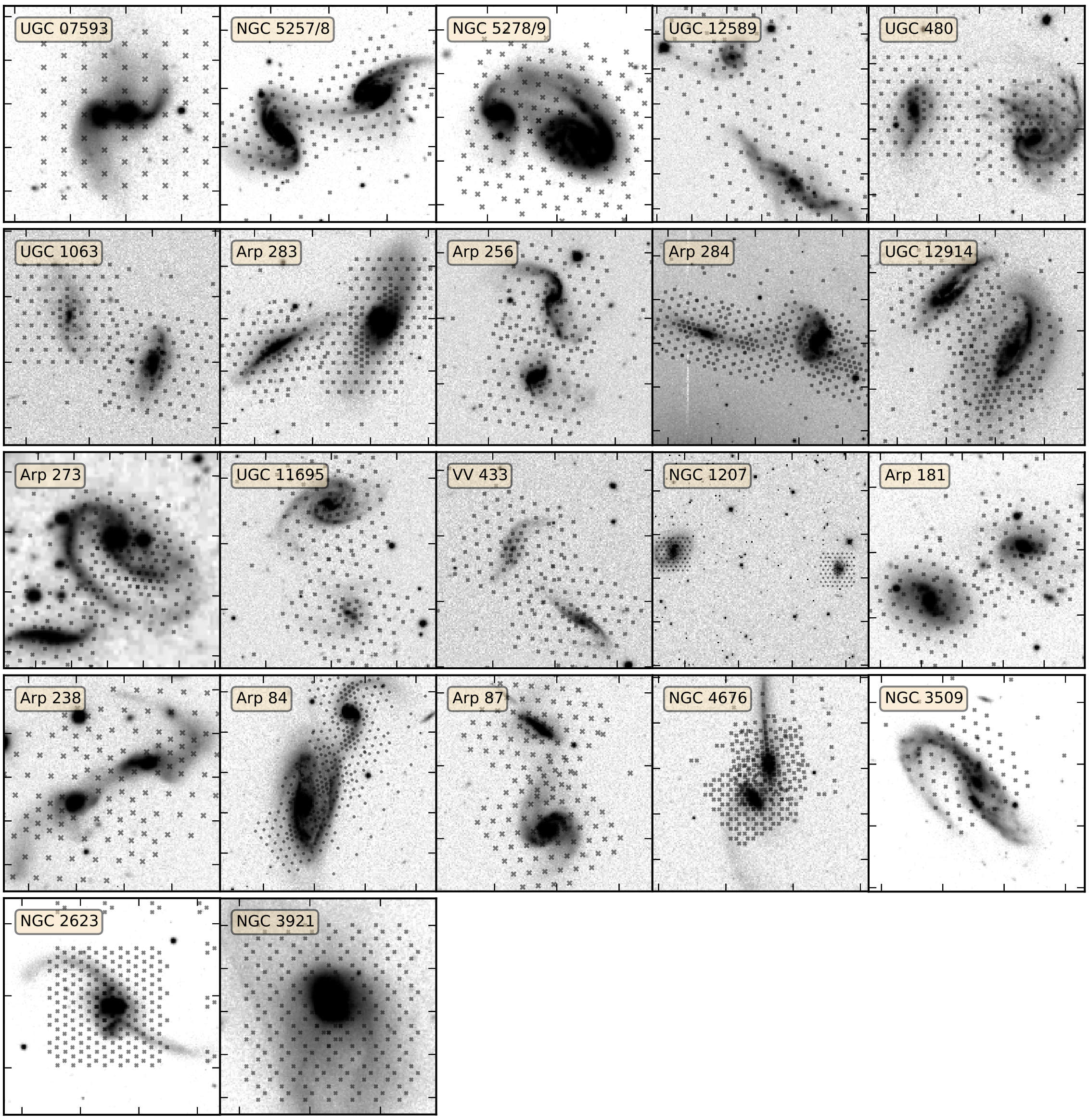

Figure 4.1: Shows a collage of systems observed with SparsePak. SparsePak pointings used are shown on each image with x showing the fiber positions. Images are taken from SDSS, except for Arp 273 which is taken from DSS.

system name	RA	DEC	observation date	redshift	# of pointings	exposure time (mins)
UGC 12914	0.4171	23.4898	Oct 2012	0.0146	3	65, 30, 125
Arp 256	4.7104	-10.3693	Oct 2012	0.0272	2	40, 65
VV 433	9.8322	13.1064	Oct 2012	0.0353	2	60, 105
UGC 480	11.6472	36.3286	Oct 2012	0.0374	2	97, 90
UGC 1063	22.2881	11.1360	Oct 2012	0.0193	2	65, 65
Arp 273	35.3778	39.3660	Oct 2012	0.0251	3	37, 50, 32
NGC 1207	47.0034	38.3769	Oct 2012	0.0160	2	50, 25
NGC 2623	129.6001	25.7545	Mar 2008	0.0185	3	185, 86, 90
Arp 283	139.3624	41.9970	Oct 2012	0.0060	3	55, 65, 95
Arp 181	157.1193	79.8182	May 2013	0.0326	1	30, 82
NGC 3509	166.0981	4.8286	Mar 2008	0.0257	1	110
Arp 87	175.1850	22.4379	May 2013	0.0237	2	25, 58
NGC 3921	177.7786	55.0788	Mar 2008	0.0197	3	120, 120, 120
UGC 07593	187.0612	44.4532	Apr 2012	0.0230	1	95
NGC 4676	191.5443	30.7271	Mar 2008	0.0220	4	150, 120, 120, 120
Arp 238	198.8870	62.1269	May 2013	0.0308	2	25, 35
NGC 5257/8	204.9805	0.8354	Apr 2012	0.0227	2	85, 90
NGC 5278/9	205.4237	55.6722	Apr 2012	0.0252	2	65, 65
Arp 84	209.6492	37.4391	May 2013	0.0116	4	105, 30, 35, 30
UGC 11695	318.0418	-1.4857	Oct 2012	0.0323	2	65, 125
UGC 12589	351.2615	0.0096	Oct 2012	0.0338	2	45, 125
Arp 284	354.0750	2.1557	Oct 2012	0.0093	4	39, 35, 55, 121

Table 4.1: List of objects observed systems sorted by the date of observations. redshifts are obtained from the current work. Number of pointings show how many times we moved the SparsePak IFU to cover both galaxies and their tidal tails. Total exposure time is written for each pointing. This was originally determined either by calculation of continuum S/N from SDSS r-band image, but we reduced it in favor of observing more systems when strong emission lines were observed in tidal tails during the first few exposures.

pointings and the observed exposure time on each pointing.

Sky spectra was obtained simultaneously with the 7 outer SparsePak fibers. SparsePak was oriented on the target in a way to maximize the number of sky fibers laid on dark patches of sky in the SDSS image. If the outskirts of the galaxies were far enough to cover the sky fibers, we oriented the IFU to put some of the science fibers on blank sky.

CuAr and ThAr calibration lamps were taken either before or after the science exposures on most pointings for accurate wavelength calibration. We made three or more science exposures at each pointing to correct for the night sky lines and the cosmic rays. We also took dome and twilight flats and zero exposures at the beginning/end of the night to adjust the variation in the CCD.

4.3 Data Reduction

IRAF (Tody, 1986, 1993) was used to reduce the data and prepare the sky subtracted spectra for fitting emission lines. Along with the standard IRAF manuals, Cigan (2004); Hooper et al. (2014) were used. The raw images are reduces using the zero level, dome flat, twilight flat, calibration lamp and sky fibers. Zero level image is subtracted from the raw image. Dome flat image is used to correct for CCD variation, and calibration lamp exposures are used for wavelength calibration. The sky fibers are subtracted from each exposure separately. We also used twilight flats for fiber-to-fiber correction, and applied it when it helped for better sky subtraction.

First, the overscan portion and the trim section of the frame are used to make the overscan correction on all of the raw images (ccdproc task). Then zero level images are combined (zerocombine task), and the combined zero level image is subtracted from all overscan corrected images (ccdproc task). Dome flat exposures are combined (flatcombine task). LA cosmic package (van Dokkum, 2001) is used to remove the cosmic rays from all science exposures. We used a relatively high detection limit to prevent the Laplacian edge detection algorithm from confusing bright sky emission lines with cosmic rays (sigclip ≈ 20). We also apply the IRAF cosmicrays task on LA cosmic cleaned images as we learned that it is very robust in removing the remaining bad pixels and does not significantly affect the science features. We then combine different science exposures on the same target in the same night (imcombine). Next, lists of sky fibers for each pointing, and the nearest in time calibration lamp exposure to each science exposure are prepared by careful inspection of IFU orientation and observing logs. These lists are used by the dohydra task. We use the dohydra to apply flat correction and wavelength calibration, and spectra extraction. We do the process above for the twilight flats, and use the twilight flat extracted spectra for obtain fiber-to-fiber throughput correction. We use task skysub to subtract the average of sky fibers from science fibers, get the final spectra.

For accurate measurement of the uncertainty of fitted parameters we need to calculate the error of the spectra at each wavelength, which are also called the “error arrays". Assuming that data of science fibers, sky fibers, flat image, and zero level image are independent, a simple error propagation gives

$$\text{error array} = \text{science image} \times \sqrt{\frac{\sigma_{\text{raw}}^2 + \sigma_{\text{sky}}^2 + \sigma_{\text{zero}}^2}{(\text{raw-sky-zero})^2} + \left(\frac{\sigma_{\text{flat}}}{\text{flat}}\right)^2}. \tag{4.1}$$

We took both flat and twilight exposures with long enough exposures to have high number counts in all pixels without saturating the CCD. So, we can ignore the $(\sigma_{\text{flat}}/\text{flat})$ term above. We will have

$$\text{error array} = \frac{1}{\text{flat}}\sqrt{\sigma_{\text{raw}}^2 + \sigma_{\text{sky}}^2 + \sigma_{\text{zero}}^2}, \tag{4.2}$$

where σ_{raw}, σ_{sky}, and σ_{zero} are errors of raw image, sky, and zero, respectively. With Poissonian errors being the square root of the number count, we have

$$\text{error array} = \frac{\sqrt{\text{raw} + \text{sky} + \text{zero}}}{\text{flat}} \quad \text{and} \quad \text{error array}^2 = \frac{\text{raw} + \text{sky} + \text{zero}}{\text{flat}^2}. \tag{4.3}$$

In order to calculate the error arrays we went through these extra steps. First, we add combined zero level image to the raw image (imsum task). We calculate the square of the combined flat images (imfunction task), and combine zero added images (imcombine). We use the dohydra task to apply flat correction with the flat squared image, and to do the wavelength calibration. In order to get the square of error arrays based on Equation 4.3, we should add the average sky spectrum to other spectra. But, we did not find an IRAF task to do this, so we decided to calculated the errors without adding the sky. Note that the zero + raw spectra in science fibers have larger values than the sky fibers. The square of error arrays in Equation 4.3 is underestimated by no more than 50% when we do not add the sky. This will reduce the error arrays by only less that 30%. In this work, we did not add sky for measuring the error arrays, and our errors are a close lower limit of the actual errors of the spectra. We inspected the spectra and visually compared the estimated errors with the variation of flux density in the continuum, to confirm that the errors are realistic. (See Figures 4.3 and 4.4.)

4.4 Emission Line Analysis

The goal of theses observations were to obtain the kinematics of Hα and [N II] emission lines throughout the systems, including the faint tidal tails. We did not make any attempt to fit the stellar model to the continuum as it is usually too faint in the tidal tails. We only fit emission line models to the Hα [λ6563]- [N II][λ6583, λ6548] triplet. The absence of stellar model affects the Hα line flux measurements, as we do not take the underlying Hα absorption into account. Our measurement of Hα flux is underestimated, and our [N II]/Hα is overestimated. Assuming a typical underlying

Hα absorption equivalent width (EW) of 2Å, the log([N II]/Hα) is overestimated by about 0.1 dex. We will discuss this effect in §4.4.3.

The relatively high spectral resolution of our data allows us to explore fitting more that one emission line components. This step is essential for separating the shocks using the velocity dispersion of emission lines. Sometimes, two gaseous components with different line of sight velocities lay into the same fiber, and their emission line profiles blend with each other. One-component fit may measure a velocity that is offset from the velocity of both components. It may also measure a velocity dispersion that is broader than the velocity dispersion of individual blending components. In the following sections we describe the method we used for fitting one and two velocity components and estimating the errors of the fit parameters.

4.4.1 One-Component Fit

We first fit a triple Gaussian (three Gaussian functions with same free velocity dispersion, σ, and free normalization factor, p_0 and p_3, with centers separated by the wavelength difference between [N II]λ6549, H$\alpha\lambda$6563, and [N II]λ6585) and a straight line with a free slope representing the background. The fit function is

$$
\begin{aligned}
\text{model}_{\text{1-comp}} &= \text{slope} \times x + \text{offset} \\
&+ \frac{1}{\sigma\sqrt{2\pi}} \left(p_0 e^{-(x-6562.82(1+z))^2(2\sigma)^{-2}} \right) \\
&+ \frac{1}{\sigma\alpha\sqrt{2\pi}} \left(p_3 e^{-(x-6583.46(1+z))^2(2\alpha\sigma)^{-2}} \right) \\
&+ \frac{1}{\sigma\beta\sqrt{2\pi}} \left(p_3/2.95 \; e^{-(x-6548.05(1+z))^2(2\beta\sigma)^{-2}} \right), \\
z &= \frac{p_1}{c}, \\
\sigma &= \frac{p_2}{\sqrt{8\log 2}},
\end{aligned}
\tag{4.4}
$$

where p_0, p_3 are the fluxes of [Hα]λ6562.82, [N II]λ6583.46, respectively, p_2 is the FWHM of the Gaussian, and p_1 is the receding velocity. α=6562.82/6583.46 and β=6562.82/6583.46 are factors that take the small difference of line widths for same velocity dispersion into account. We use the theoretical value of 2.95 for [N II]λ6583.46/[N II]λ6548.05 ratio (Acker et al., 1989). Along with the slope and the offset of the background we fit a total of 6 parameters.The fit range is from 6518Å to 6608Å in the target rest frame.

We use a Markov Chain Monte-Carlo (MCMC) method to estimate the uncertainty of the fit parameters. The initial MCMC step is determined with the least square minimization. We use the emcee python package, varying the the 6-

dimensional parameter with the following prior constraints.

$$\begin{aligned} 1.5 \leq \text{slope} &\geq -1.5 \\ \text{H}\alpha\ \text{flux}(p0) &\geq 0 \\ 600\ \text{km/s} \geq \text{velocity}(p_1) &\geq -600\ \text{km/s} \\ 14\mathring{A} \geq \text{FWHM}(p_2) &\geq 1\mathring{A} \\ [\text{N II}]\lambda6583.46\ \text{flux}(p3) &\geq 0 \end{aligned} \tag{4.5}$$

The velocity here is with respect to the reported redshift for each system. The log of the used likelihood function is

$$\ln p(y_i|x_i, \sigma_i, \text{model}) = \sum \left[\frac{(\text{model}(x_i) - y_i)^2}{\sigma_i^2} + \log \frac{1}{2\pi\sigma_i^2} \right], \tag{4.6}$$

where y_i and x_i are the spectrum data points, and σ_i is the error array.

We performed 700 MCMC steps with 100 walkers, to make sure that we reach an equilibrium distribution in the last 200 steps. We checked the MCMC time series for all of our fits to confirm that we have the equilibrium distribution in the last 200 steps. Figure 4.2 shows an example of the posterior probability distribution of parameters given by last 200 steps of the time series. It shows all the one and two dimensional projections of the 6-dimensional distribution. The uncertainty of each parameter can be measured robustly from the variance of these projections. We used the 16% and 84% percentile values for the low and high error limits.

4.4.2 Two-Component Fit

Visual inspection of our one-component fits makes it clear that in some of the fibers the emission has more complicated profile than a simple Gaussian. Sometimes the three emission lines in the Hα -[N II] triplet show a consistent deviation from a single Gaussian profile, indicating that the emitting gas projected into the fiber has more than one kinematic components. Figure 4.3a shows an example of a fiber for which one-component triple Gaussian cannot well-describe the shape of the emission line triplet.

We fit two triple-Gaussian functions along with the background line to the Hα -[N II] triplet in all fibers. The model we used is the one-component model with an extra triple-Gaussian added to it. In this model p_4, p_5, p_6, and p_7 are the Hα flux, redshift, FWHM, and [N II]λ6583.46 flux of the second component, respectively. Again, we perform MCMC to estimate the error of the fit parameters. We only attempt to fit the second component when we find Hα flux S/N>3 in the one-component fit. The same prior constraints of Equation 4.5 are used for both components. However, we add the following constraints to make sure that the two components have either different redshift or different FWHM. Without this constraint two components with the same kinematics can reproduce a fit that is similar to a single component fit, and provide no new information about the line profile. To prevent walkers from waisting

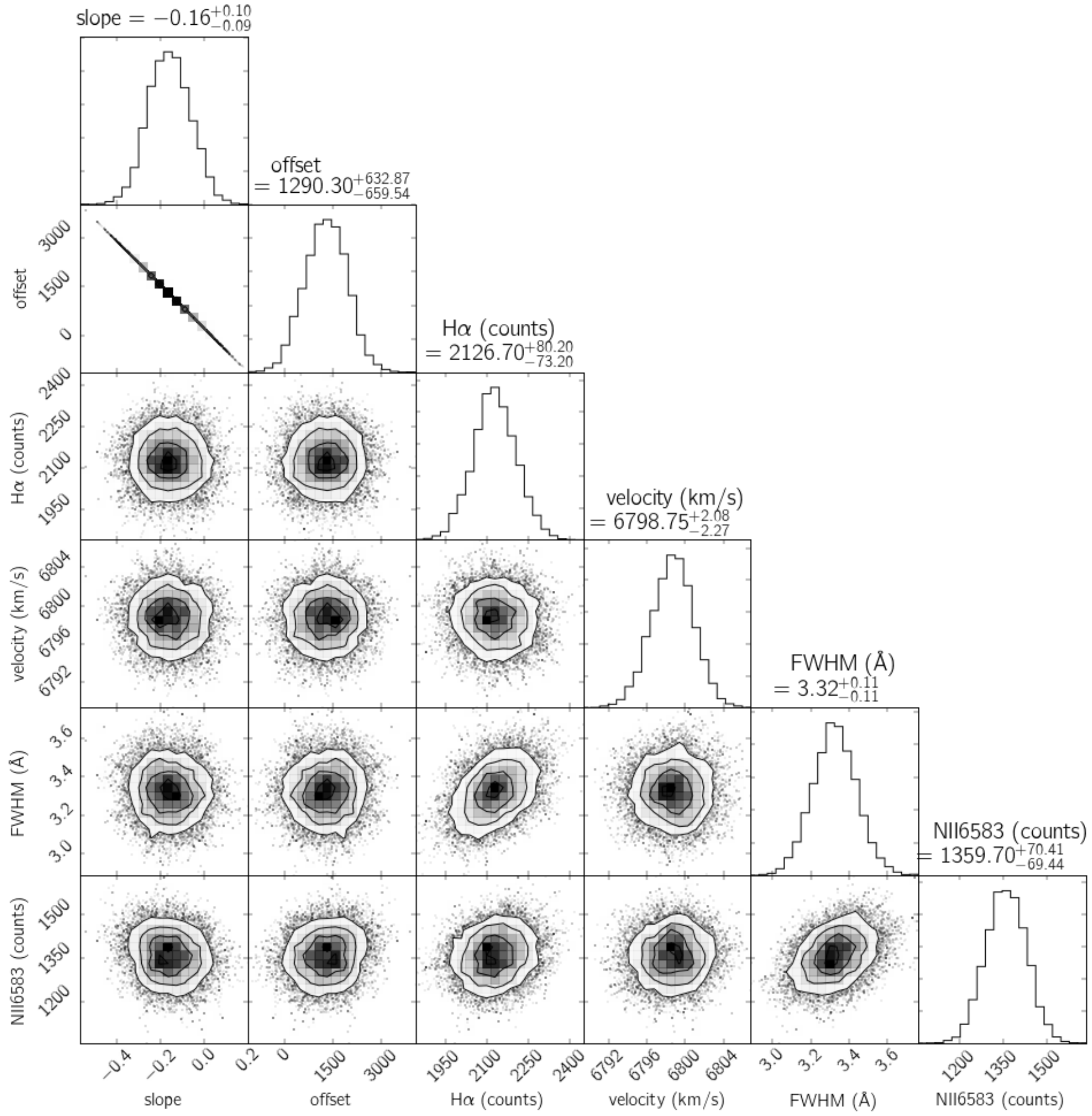

Figure 4.2: One and two dimensional projections of the posterior distribution function of parameters of one triple-Gaussian and a background. The distribution is obtained from the last 200 steps of the time series when the MCMC walkers are in equilibrium. The 16 and 84 percentiles are used as the low and high error limits. The errors written on top of each column are typical for emission lines with S/N >20.

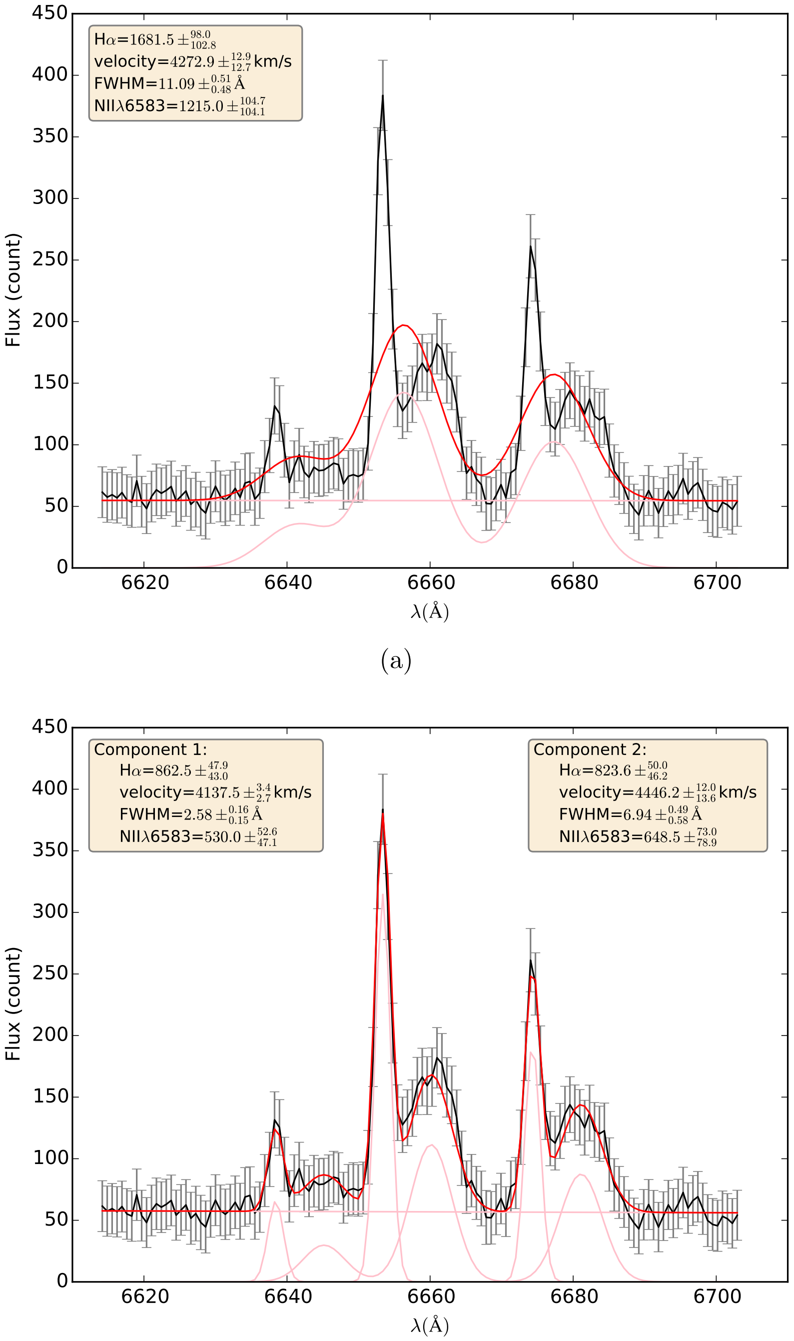

(a)

(b)

Figure 4.3: (a)Fitting of one triple-Gaussian with a background line to a fiber in observation of UGC 12914. (b) Fitting two triple-Gaussians with a background line to the same fiber. The parameters of the triple-Gaussian function and their MCMC uncertainties are shown in the text box(es) in the upper left (and upper right) corner(s). It is clear that the one-component can not capture all the information available in the emission line profile.

time in these answers, we exclude them in the prior:

$$
\begin{aligned}
&\mathrm{H}\alpha\ \mathrm{flux}_1(p_0) \geq \mathrm{H}\alpha\ \mathrm{flux}_2(p_5)\ \text{and} \\
&\mathrm{velocity}_1(p_1) \geq \mathrm{velocity}_2(p_6) + 45\ \mathrm{km/s}\ \text{or}\ \mathrm{velocity}_1(p_1) \leq \mathrm{velocity}_2(p_6) - 45\ \mathrm{km/s} \\
&\text{or} \\
&\mathrm{FWHM}_1(p_2) \geq \mathrm{FWHM}_2(p_7) + 1.5\mathring{A}\ \text{or}\ \mathrm{FWHM}_1(p_2) \leq \mathrm{FWHM}_2(p_7) - 1.5\mathring{A}
\end{aligned}
\tag{4.7}
$$

The likelihood function is the same as Equation 4.6. Fitting the two-component fit involves 10 parameters, so more MCMC time steps are required to achieve an equilibrium distribution. We performed 1200 MCMC steps with 100 walkers, and used the distribution of the last 200 steps for estimating the posterior distribution of the parameters and measuring their uncertainties. We checked MCMC time-series to confirm that for all fibers the equilibrium is reached in the last 200 steps. Figure 4.3b shows the two-component fit to the same fiber shown in Figure 4.3a.

We use an F-test (Lomax, 2007) to determine whether a two-component model is preferred over the one-component fit. In general, increasing the number of parameters improves the χ^2 statistics as more parameters can push the model to reproduce the subtle features in data, even if they are statistically insignificant. The F-test uses the number of free parameters in the two models and the number of data points, to compare the models and determine if the improvement in the χ^2 is enough to pick the model with more components. As an example, for the fit in Figure 4.3 the F-test prefers the two-component fit, because the second component significantly improves the χ^2. We perform the F-test only when the Hα flux of the second component has a S/N larger than 3, otherwise one-component fit is preferred without performing the F-test.

In general, we find two classes of two-component models. One class is when the two components are both relatively narrow, their FWHM being close to each other, and their difference being mostly in their velocity (redshift). These two components are likely to be two star forming regions of the galaxy moving at different line of sight velocities. This can happen in binary galaxy mergers when two or more segments of the two galaxies lay in the same line of sight direction. The other class of the two-component models is when the two-components have very different FWHM, one being much broader than the other one. The broad emission is likely to originate from the high-velocity dispersion winds/shocks or even ionized inflowing gas toward the star forming region detected by the narrow components. Figure 4.4 shows examples for both of these classes.

4.4.3 Underlying Hα absorption

Taking a straight line as the background means that we are ignoring the underlaying Hα absorption in this fit. So, our measurement of Hα flux is a lower limit and our measurement of [N II]/Hα is a higher limit. In Chapter 3 we discussed this effect on

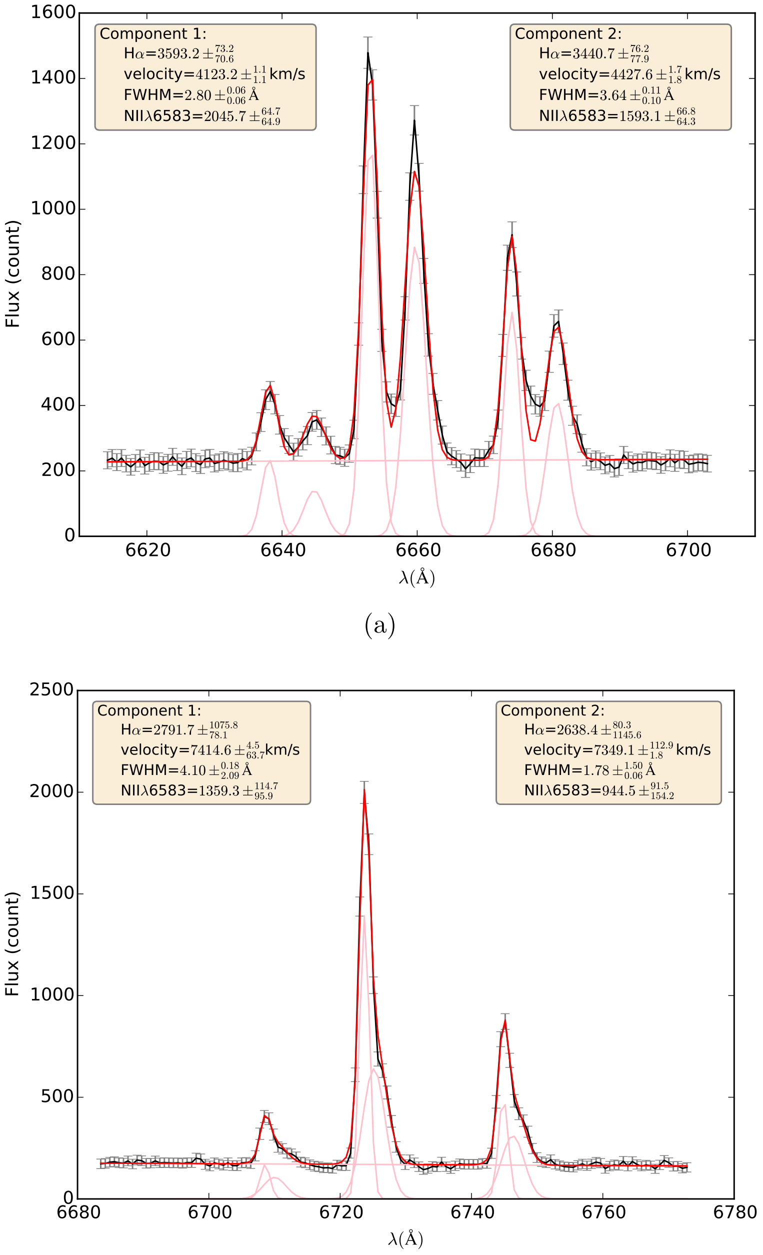

(a)

(b)

Figure 4.4: Two different classes of two-component fit to the Hα -[N II]triplet. Both fibers are from observation of NGC 5258. In (a) both components are relatively narrow and are separated by redshift(velocity). These components are likely to be two star-forming regions from different parts of the galaxies laying in the same fiber field of view. In (b) one component is significantly broader than the other, indicating that the source is more turbulent ionized gas with higher velocity dispersion, residing around the HII regions that emits the narrow component. In this particular case the broad component is redshifted with respect to the narrow component, suggesting the presence of high speed inflowing gas.

the spectra of the Mice galaxies (NGC 4676). We showed that by putting the same cut of -0.2 on log([N II]/Hα), the same bi-cone structure as of the CALIFA data (Wild et al., 2014) is found to have high [N II]/Hα . CALIFA data analysis includes stellar modeling, and the similarity of our results with that of Wild et al. (2014) suggests that the underlying Hα absorption does not significantly change many of [N II]/Hα measurements.

For our shock analysis we need to have an estimate of the effect of underlying Hα absorption on the measured [N II]/Hα . In Table 4.2 we show the minimum of 1-component fit Hα equivalent width (EW) in fibers with Hα flux S/N>3. The highest minimum EW is measured in Arp 283 (minimum EW$\approx 7\AA$). To minimize the effect of Hα stellar absorption we remove fibers with Hα EW< 7 Å from our shock analysis.[5] By having Hα emission line EW > 7 Å, and assuming a typical underlaying absorption EW of ~ 2 Å, the log([N II]/Hα) used for shock analysis changes by less < 0.10 dex which is within the typical error of log([N II]//Hα) in faint components.

Putting a lower cut on Hα EW removes a significant number of detected components with S/N > 3 ($\approx 30\%$). However, most of the Hα flux in these galaxies come from the luminous fibers, so the flux in the removed fibers are not significant, and they do not affect the measurements of shocked Hα fraction significantly. To demonstrate this in Figure 4.5 we show the both un-weighted and Hα flux weighted histograms of Hα EW for all of the observed systems. When looking at this plot please note that

---

[5] We keep them for velocity measurements as the underlying absorption does not significantly affect the velocity of the emission lines.

our data is not flux calibrated. So for weighting this histogram, and for comparing Hα flux ratio between observed systems we used the total Hα flux counts from the fit parameters and weighted them by the exposure time. This is not accurate because of CCD variations and because some systems were observed in non-photometric conditions. However we only use this method for qualitative estimates like in Figure 4.5. In this Figure, the cut of EW=7Å is shown with the vertical red dashed line. The weighted histogram (green) shows that most of the flux is coming from fibers with large enough EW.

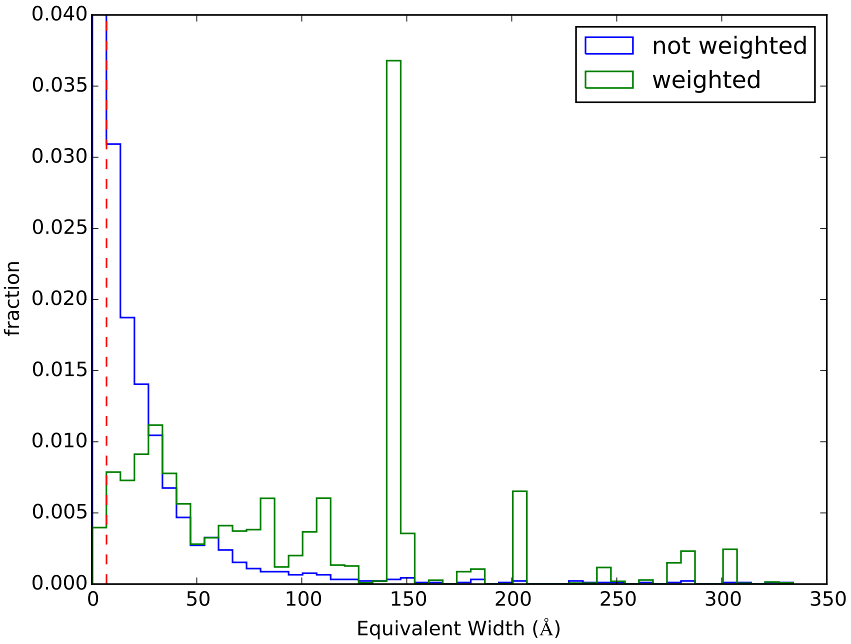

Figure 4.5: Histogram of Hα EW from 1-component fits. Blue and green lines show the un-weighted and Hα flux weighted histograms, respectively. The dashed red vertical line shows the EW cut limit of 7Å. This plot demonstrates that most of the Hα flux in our galaxies is not affected by the underlying Hα absorption.

4.5 Source of Ionization

Hα is emitted from ionized hydrogen gas and the source of ionization can be various processes. Normal HII regions are regions where the gas is photo-ionized by the UV light from the young O, and B stars with energies > 13.6 eV. Though, the photons from these stars are typically not energetic enough to significantly ionize metals (e.g. N and O) to high ionizing levels. If the star formation is not happening in a turbulent region of the ISM, the velocity dispersion of this photo-ionized gas is only a few tens of kilometers per second.

Star-forming regions provide the most appropriate kinematic tracers among optical emission lines for dynamical modeling of disk galaxies. Photo-ionization does not change the kinematics of the gas significantly. If the gas was moving with the bulk of the baryons before photo-ionization, we can safely assume that it continues to do so, after photo-ionization. One must remember, however, that gas can be displaced from stars before it starts to form stars. We find clear evidence for this in our sample in UGC 12914.

If the galaxy hosts an AGN, the hard UV and/or X-ray emission from the AGN with energies of up to a few keVs can also ionize the neutral gas. These energetic photons also ionize heavy metals and produce high-ionization line emissions. Specifically, highly ionized [O III]λ5003 line becomes much stronger by AGN emission. Other lower-ionization optical lines such as [N II]λ6583, [S II]$\lambda 6717, 6731$, and [O I]λ6300 also enhance compared to Hα . Some AGNs, though, only display low-ionization emission lines in the nuclei and produce much less [O III] emission. These are known as LINERs, low-ionization nuclear emission-line region galaxies.

Ionization can also happens by the input of kinetic energy rather than photo-ionization. The kinetic energy may originate from the colliding gas flows, or direct energy deposition from outflowing winds and superwinds from star forming regions or AGNs. These collisions produce shocks. Shocks are disturbances that move faster that the speed of sound in the ambient medium. These disturbances make shock fronts that dissipates much of the kinetic energy and converts it to heat. The shock-heated gas cools via radiation which is itself a powerful source of ionizing photons. Photons from the post-shock gas can travel upstream and may photo-ionized the pre-shock material known as pre-cursor. The emission from the shock and the precursor can produce high emission line ratios, particularly among the low-ionization species. It has been shown that LINER-like emissions, particularly in the extranuclear regions of interacting galaxies, are more consistent with shocks rather than photo-ionization (Monreal-Ibero et al., 2010b; Rich et al., 2011). Brightness of the radiative shocks and its precursor scales with the rate of dissipation of kinetic energy in it; resultingly, one expects to see higher velocity dispersion in bright shocked emission lines (Dopita & Sutherland, 1995).

Unlike photo-ionized regions around young stars, shocked gas is not a good kinematic tracer for modeling gravitational features like tidal tails. Processes like high speed stellar wind, supernova (SN) feedback, and AGN-driven outflows, produce shock-heated ionized gas with velocities that can be significantly different from the rest of baryons in their vicinity. The Hα velocity obtained from this gas is not suitable for modeling tidal tails, especially with collisionless N-body simulations, because gravity is the only player in the formation of tidal tails. So, we need to find a way to separate the emission from the shocked gas and that from the photo-ionized gas near young stars. In this section, we propose a new method, based on previous observations, to do this separation. We find indications that shocked gas increases in galaxy mergers as time goes from the first passage the the second passage. The shocked gas fraction shows a slight correlation with mass ratio, suggesting that a more massive companion produce more shocks in a galaxy.

4.5.1 Separating Shocked and Star Forming Regions

Diagrams first proposed by Baldwin et al. 1981, know as Baldwin, Phillips & Terlevich (BPT) diagram, are used to separate nuclear star formation from AGNs (Kewley et al., 2006b; Kauffmann et al., 2003). These diagrams also suggest that sometimes the emission-line ratios are consistent with a combination of star formation and AGN hard ionization. These are known as composite galaxies.

Integral Field Spectroscopy (IFS) has made it possible to investigate emission line ratios in extended regions around the galaxies. IFS observations have shown that in some galaxies one can find LINER-like (or even Seyfert-like) emission in extranuclear regions of galaxies. In some cases, the line ratios are even larger when looking at large distances from the core (Wild et al., 2014). Optical emission line ratio maps provide a wealth of information about the possible source of excitation in different parts of the galaxy.

It has been shown that velocity dispersion of the lines also is indicative of the source of ionization, given the velocity resolution of the spectra is high enough (Rich et al., 2014). Velocity dispersion is particularly useful to distinguish emission from shocks. Monreal-Ibero et al. (2006) showed that in shock-heated extended gas, velocity dispersion of emission lines is correlated with low-ionization line ratios particularly with [O I]/Hα ratio. Monreal-Ibero et al. (2010b) and Rich et al. (2011) confirmed these results, indicating that velocity dispersion can be used as an independent probe of shocks.

Rich et al. (2011) showed that flux weighted histogram of velocity dispersion of emission lines in their high spectral resolution IFU data of LIRGs reveal bi-modality. They display a peak at low velocity dispersion of a few kilometers per second corresponding to photo-ionization by stars, and a peak at velocity dispersions higher that 100 km/s. Rich et al. (2014) showed that composite spectra in nuclei of galaxies can be made by combination of shocks and star-formations rather that AGN and star formation. Based on this observations, Rich et al. (2015) proposed a limit of $\sigma < 90$ km/s for velocity dispersion of emission from normal and turbulent star forming regions. They suggest that components with $\sigma > 90$ km/s are emitted from low velocity shocks.

As described in §4.2 our observations were carried out in the wavelength range 6050-7000Å and did not include Hβ and [O III] emission lines. So, we can not use the BPT diagnostic diagrams to separate the emission lines. However, our SparsePak data was obtained with relatively high velocity resolution of ~ 30 km s^{-1}, making it possible to use the width of emission lines to separate star formation and shocks.

The intrinsic FWHM of our SparsePak data is about 1.5Å, and to obtain the correct velocity dispersion of each emission line component we subtract the intrinsic FWHM from the fit FWHM in quadrature:

$$\mathrm{FWHM_{corr}} = \sqrt{\mathrm{FWHM_{fit}^2} + \mathrm{FWHM_{intrinsic}^2}} \tag{4.8}$$

In Figure 4.6 we show the Hα flux weighted histogram of velocity dispersion for all 956 high-S/N (>3) components in high EW fibers (>7Å) in all observed systems. We find a bi-modality in the flux weighted distribution of velocity dispersions similar to that observed by Rich et al. (2011). There is significant bump in flux of components around velocity dispersion of ~ 150 km/s. The high velocity dispersion bump seem to be more prominent in the coalesced systems. It can be seen that the small companions in galaxy pairs do not display the bump at that velocity.

Combining a projection of the BPT diagrams on the [N II]/Hα direction and our understanding of line width of shocked line emission, we decided to use plots of

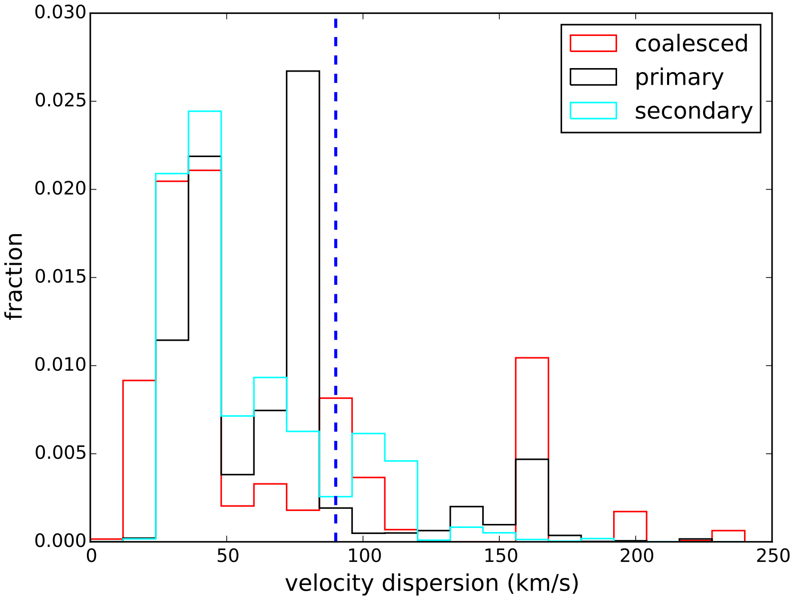

Figure 4.6: Hα flux weighted histogram of velocity dispersion for 956 components in all galaxies in our sample. These are the components with S/N>3 in fibers with Hα EW > 7Å. The limit of 90 km/s is shown by the blue dashed vertical line. The coalesced systems show a bigger bump at high velocity dispersion. The same is true for primary galaxies compared the secondary ones.

[N II]/Hα vs. velocity dispersion to separate the shocked regions from normal star forming ones. Based on the line suggested by Kewley et al. (2006b) for separating star-forming galaxies from composites, spectra with [N II]/Hα <-0.2 are more likely to be star-forming, and spectra with [N II]/Hα >-0.2 are more likely to be composite or AGN. Rich et al. (2014) showed that many composite-like spectra are shock-dominated. On the other hand, for velocity dispersion, Rich et al. (2015) showed that one can separate the shocked emission line components by use of velocity dispersion alone. They put a limit of 90 km/s to separate star formation and shocks. Like the limit of line-ratio, this limit is not rigid. On the low side of the limit, components are more likely to be star forming, and on the high side the opposite is true.

In Chapter 3, we used the same plot for separating emission lines observed in the Mice galaxies. In Figure 3.3, we divided the emission line components visually into three groups. Group 1 has low [N II]/Hα and low velocity dispersion. Both criteria indicate that group 1 components are likely to be emitted from the star-forming regions. We used these components to produce the Hα velocity map that was in excellent agreement with HI velocity map of the Mice galaxies. The criteria for a group 1 component is

$$\begin{aligned} &\sigma < 90 \text{ km/s} \\ &\log([\text{N II}]/\text{H}\alpha) < 0.00166\sigma - 0.5 \ . \end{aligned} \tag{4.9}$$

Group 2 components have high [N II]/Hα :

$$\begin{aligned} &\log([\mathrm{N\ II}]/\mathrm{H}\alpha) > 0.001\sigma - 0.30 \\ &\log([\mathrm{N\ II}]/\mathrm{H}\alpha) > 0.00166\sigma - 0.5\ , \end{aligned} \tag{4.10}$$

and group 3 components have high velocity dispersion:

$$\begin{aligned} &\sigma > 90\ \mathrm{km/s} \\ &\log([\mathrm{N\ II}]/\mathrm{H}\alpha) < 0.001\sigma - 0.30\ . \end{aligned} \tag{4.11}$$

The separating lines are shown in Figure 4.7 and all future Figures of [N II]/Hα vs. velocity dispersion. For the Mice we took group 2 as shocks, and group 3 as unresolved blending of multiple emission lines in the center. In this chapter we consider group 3 components as shocks along with group 2. The reason is that we find most group 3 components to come from extranuclear regions, and visual inspection of lines confirm that they are indeed wide single components.

Group 1 components are from star forming regions and group 2 and 3 are from shocked gas. Selection of group 1 components are fairly conservative, but for the shocked gas we should keep in mind that high low-ionization line ratios and wide emission lines can be caused by other ionization sources, such as AGN hard UV/X-ray emission and heating by post AGB stars. In the next subsection we discuss the source of ionization in our systems from [N II]/Hα maps of the components selected as shocks.

Figure 4.7 shows plot of [N II]/Hα vs. velocity dispersion for all components, similar to that of Figure 3.3 in Chapter 3. In this plot one can see that most of the emission line components in our sample are in group 1, emitted from normal HII regions. There is clear concentration of points at 30 km/s which is due to our velocity resolution. Black and cyan points are components in the primary and secondary companions in the pairs, respectively, and red points are components in the coalesced systems. We can see that the black points are concentrated in a slightly higher region in group 1 region, having a slightly higher [N II]/Hα . This suggests that they are emitted from a slightly more excited gas. We will discuss this in §4.5.5.

Table 4.2 shows different quantities measured for the systems observed. The light ratios are mostly obtained from the K-band magnitudes of the 2MASS survey (Skrutskie et al., 2006). The projected separation between the cores of the two galaxies is measured using the redshift distance and angular separation. The difference in the velocities of the cores (Δv_C) is measured for the closest star-forming component to the morphological core. We present the lowest Hα EW for components in each system. We use an EW low cut of 7 Å in all systems as discussed in §4.4.3.

We measure the fraction of Hα emission from shocked gas to the total Hα flux in each system($\mathrm{f_{shocked}}$). This value is obtained by dividing the sum of Hα flux from groups 2 and 3 components to the total Hα flux in all fibers. This measurement is an approximate estimate as our spatial coverage is not complete, and we may have missed regions with effectively high or low shock fraction laying in between the

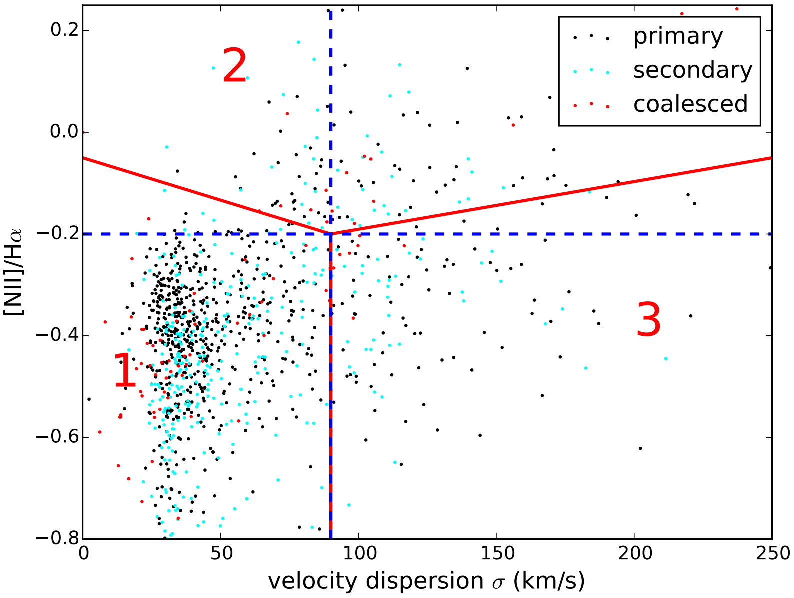

Figure 4.7: Plots of [N II]/Hα vs. velocity dispersion for all 956 components in all galaxies in our sample. These are the components with S/N>3 in fibers with Hα EW > 7Å. This includes the two components that are occasionally fit in a single fiber. The black points show the components in the massive (more luminous) companion (primary) and the cyan points show the component in the secondary one. the red point show the components in the coalesced systems. One can see the distribution of black points lay slightly higher in [N II]/Hα .

sparsely positioned fibers. Moreover SparsePak has a denser grid in the center which is usually placed on the cores of the galaxies. As a result, our measurement of shocked Hα fraction is biased toward its value near the cores of the galaxies. We measured the uncertainty in the fraction of shocked Hα ($\sigma_{\rm fshocked}$) by bootstrap sampling of data points in the [N II]/Hα -velocity dispersion space, based to the measured uncertainty for [N II]/Hα and velocity dispersion. For each sample we sum of the Hα flux in components of groups 2 and 3 and divide it by the total Hα flux. The standard deviation of shocked Hα fraction in 100 samples is reported as the uncertainty of shocked fraction.

4.5.2 Velocity Maps

Figure 4.8 shows map of velocity of star forming components in all of the observed systems. Velocity of Hα emission is not much affected by the underlying absorption, so we plot these velocity maps for all components with with S/N$>$ 3 without the Hα EW cut. In 13 out of 19 separate pairs we find smooth rotation in both galaxies confirming that these components move with the bulk of the baryon in their vicinity and can be used to trace velocity of material governed by gravity. Four systems only show rotation in one galaxy. The secondary companion in UGC 480, Arp 273, and Arp 181 do not display a lot of star forming regions. In Arp 283 the primary galaxy shows no Hα emission in the outskirts, and has a disturbed velocity field in the center. NGC 5278/9 shows a disturbed rotation, and UGC 12914 displays a messy velocity

system name	light ratio	separation (kpc)	Δv_C (km/s)	minimum EW($\AA$)	$f_{\rm shocked}$	$\sigma_{\rm fshocked}$
NGC 1207	8.34	113.7	92.1	1.0	0.034	0.059
UGC 480	2.70	63.9	71.4	1.4	0.213	0.030
UGC 11695	8.00	51.5	162.2	4.6	0.239	0.028
UGC 12589	3.64	51.4	41.0	2.0	0.239	0.018
VV 433	3.12	50.5	168.1	4.1	0.126	0.058
Arp 181	1.98	49.2	102.7	1.4	0.004	0.005
Arp 273	2.84	41.7	406.9	0.6	0.304	0.079
NGC 5257/8	1.17	37.4	148.7	1.5	0.151	0.023
Arp 256	1.90	31.3	51.6	5.6	0.134	0.024
Arp 87	1.27	30.8	74.2	1.6	0.412	0.014
Arp 84	5.00	28.9	88.5	0.4	0.101	0.005
UGC 1063	9.44	26.7	17.2	6.3	0.002	0.003
Arp 238	1.51	22.4	67.0	7.0	0.722	0.073
Arp 284	8.81	22.4	50.4	1.0	0.392	0.008
UGC 12914	1.61	20.2	142.4	1.8	0.378	0.036
NGC 5278/9	3.19	19.7	386.5	1.5	0.250	0.031
NGC 4676	1.25	16.1	287.5	1.0	0.257	0.024
Arp 283	8.43	11.5	1.9	0.7	0.232	0.059
UGC 07593	1.81	5.6	96.5	0.8	0.401	0.001
NGC 3509	-	0.0	0.0	3.4	0.012	0.012
NGC 2623	-	0.0	0.0	0.3	0.895	0.050
NGC 3921	-	0.0	0.0	1.0	0.702	0.064

Table 4.2: This table shows the some of the measured quantities for the observed systems. It is sorted based on the separation of the the centers. Horizontal lines indicates where we divide bins of wide pairs, close pairs, and coalesced systems. Projected separation is measured from the angular separation and redshift distance. For most systems light ratio is obtained from the 2MASS Ks-band magnitudes. For NGC4676 no measurements were found in 2 MASS catalogues. Instead we used the stellar mass ratio from Wild et al. 2014. UGC 07593 pair is not resolved in 2 MASS so SDSS r-band light ratio is used instead. Velocity difference, Δv_C, is the difference in the line of sight velocity of the star-forming components that are closest to the centers. Minimum Hα EW measured by a single-component fit is written for fibers with S/N > 3 in each system. The highest value EW=7.0 (Arp 283). In order to measure a consistent shock fraction among all systems and to minimize the effect of the underlying Hα absorption, we remove fibers EW< 7 from our analysis. Shocked Hα fraction and error are shown in the last column.

field in a bridge of star forming regions between the two galaxies, consistent with HI and CO observations. We will discuss some of the interesting features of individual systems in the Appendix.

In some of the velocity fields one can see a void in the center of the galaxy. This can be due to high velocity dispersion, or [N II]/Hα of components near the center, that made us classify them in groups 2 or 3. Also some of the galaxies show an old or post-starburst stellar population near the center.

Among the three coalesced systems we see smooth rotation only in NGC3509. This system has very little shocked Hα fraction. The other coalesced systems, NGC 2623 and NGC 3921, display few star forming components and show no clear rotation.

4.5.3 Indications for Galaxy-Wide Shocks from [N II]/Hα Maps

IFS observations of systems with unambiguous AGN usually display a gradient of emission line ratios from the center to the edge. Hard ionizing radiation from AGN affects the gas in its vicinity more than the gas that is kpcs away in the disk or above it. In the presence of an AGN in the center one expects to find higher [N II]/Hα near the center than in the outskirts. (Davies et al., 2014; Leslie et al., 2014) For galaxy-wide shocks, on the other hand, the regions of high velocity dispersion or high [N II]/Hα are spread throughout the galaxy. When we see these regions throughout the

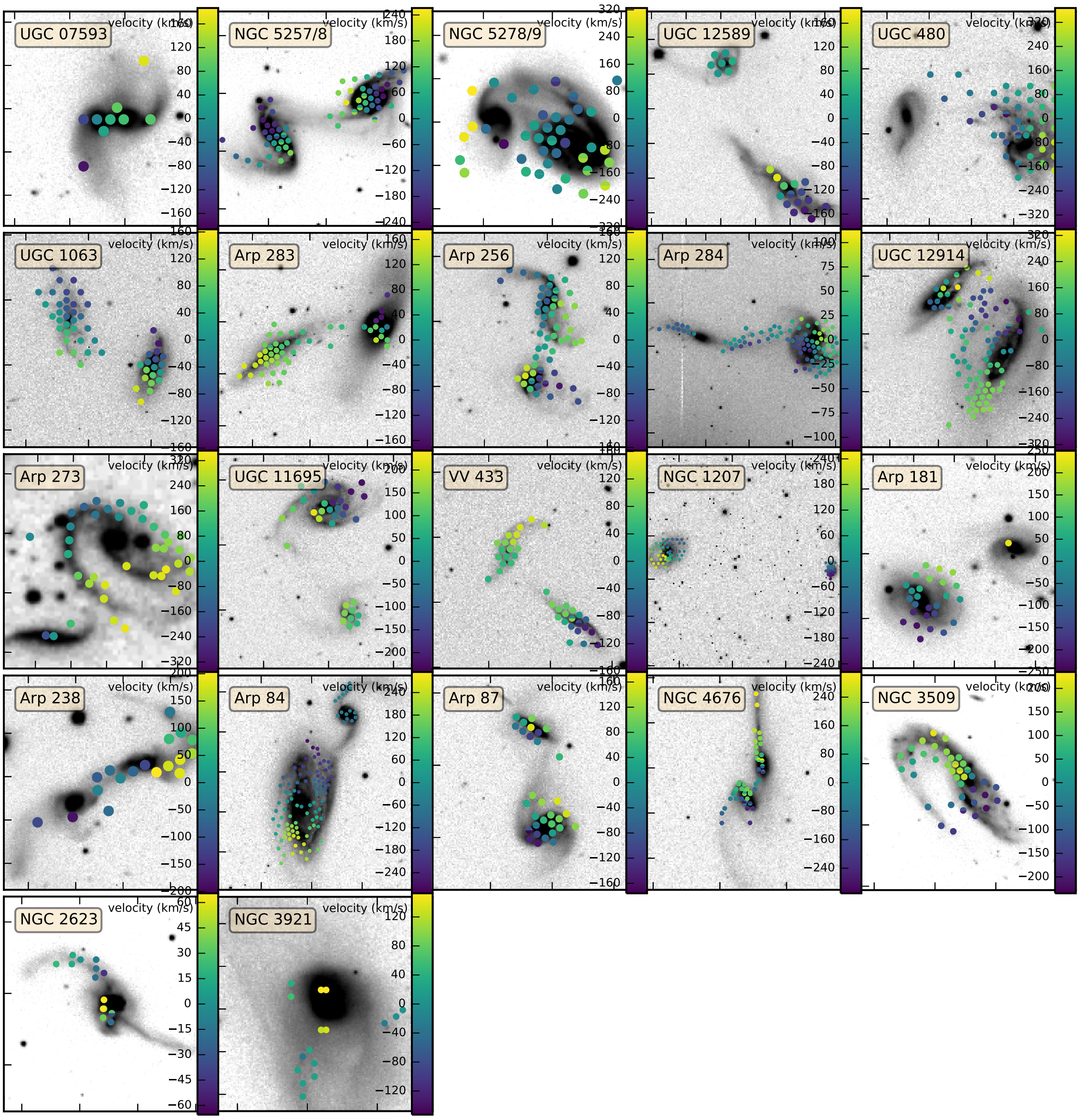

Figure 4.8: Collage of velocity maps of group 1 (star forming) components in observed systems. The scale of velocity gradient is shown next to each panel. Most of the galaxies show smooth rotation confirming that they are moving along with the bulk of baryons in their vicinity and are good tracers of kinematics for modeling tidal features.

galaxy with no gradient toward the center, we can argue that the source of ionization is most likely shocks. However, sometimes the source of shocks are the superwinds or outflows from a central processes such as starbursts of AGNs. They can also produce a gradients in the observed [N II]/Hα . So, the mere existence of a gradient in [N II]/Hα is not an indication of hard photo-ionization from AGN.

Based on the arguments above we look for indications of shocks in the [N II]/Hα maps. None of these systems are unambiguous AGNs according to the literature.[6] Figure 4.9 shows a collage of [N II]/Hα maps of group 2 and 3 components in our systems. For these maps we have implemented the Hα EW limit to reduce the effect of the underlying Hα absorption. This removed about 30% of the components most of them with high [N II]/Hα . In the maps of the remaining components in Figure 4.9 we find that four systems display no group 2 and 3 components. In 12 out of the remaining 18 systems indications from spatial distribution of group 2 and 3 components and gradient of [N II]/Hα suggest that these components are most likely emitted from shocked gas. For example, in UGC 12914 (shocked gas fraction, $f_{\rm shocked}$ = 37%) these components all lie in the bridge between the galaxies, and are more likely to be the result of collision of gas clouds during the head-on encounter between the two disks. In Arp 284, UGC 480, and NGC 3921 we see a cone-like structure toward the center, though the gradient of [N II]/Hα does not suggest a central hard ionizing source. In the remaining six systems (UGC 07593, UGC 12589, Arp 273, VV

---

[6] Some galaxies like NGC 2623 are AGN candidates, but for all of them the controversy stays. See discussion in the Appendix.

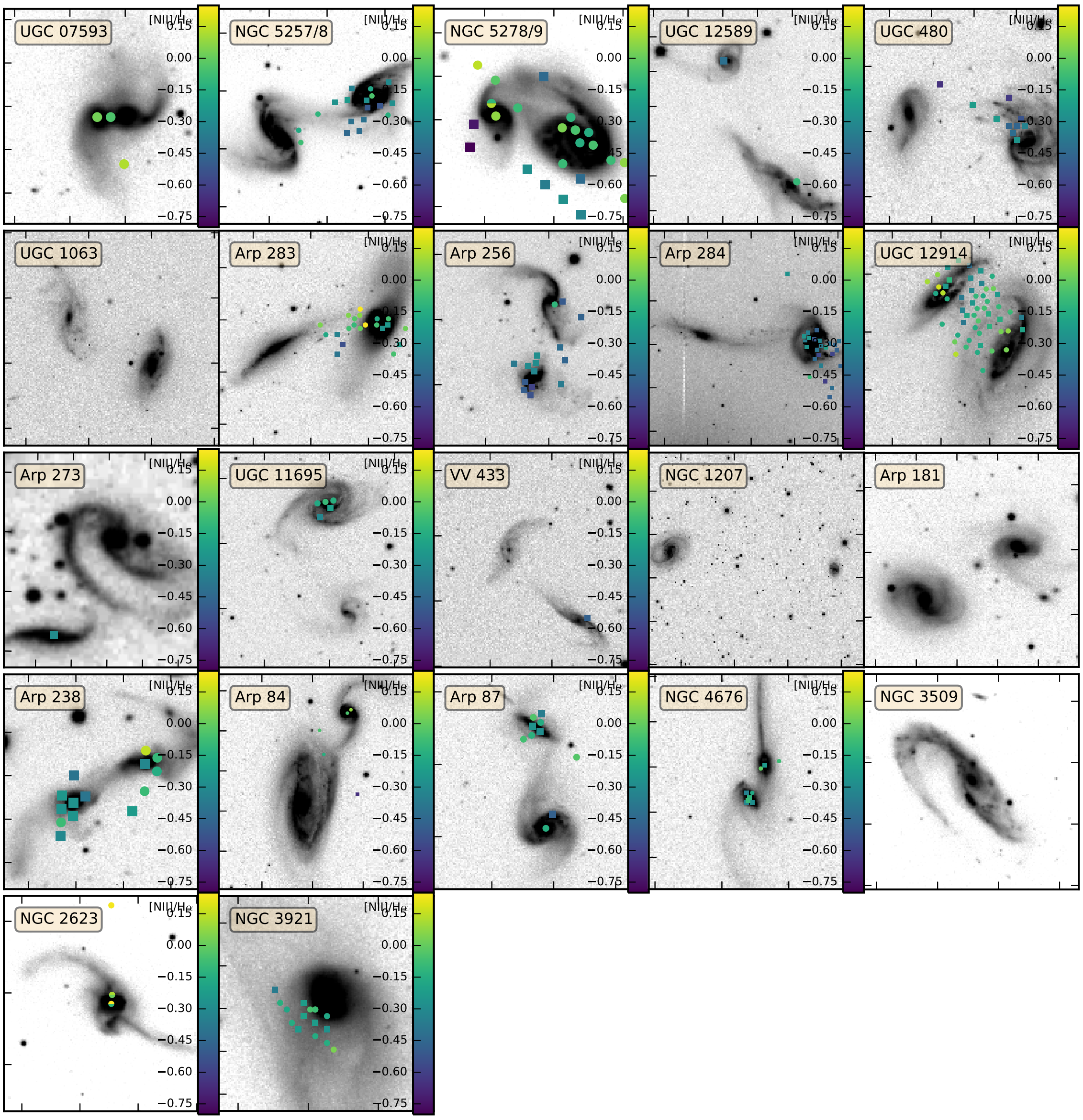

Figure 4.9: Collage of [N II]/Hα maps of group 2 and 3 components (possibly emitted from shock-heated gas) in the observed systems. Group 2 components are shown with circles and group 3 components are shown with squares. The spatial distribution of [N II]/Hα in most of they systems suggest that these are produced by shocks.

433, Arp 84, and NGC 2623), we only find one or two group 2, and 3 components near the center. While AGNs are candidate for the source of ionization, it could be the result of shocks from central gas inflows and outflows, therefore the source is ambiguous in these systems.

4.5.4 Shocked Gas and Merger Sequence

Except for the three coalesced systems, our sample is selected so that all galaxies are pairs with strong tidal features. In this sample we look at a specific stage of the galaxy evolution, between the first and the second passage. We have a unique possibility to check with statistical significance, what happens to each galaxy as a function of the properties of its companion. In particular, we can separate the galaxies based on the mass ratio and follow the effect of the mass of the companion on the amount of shocked gas at different merger stages.

Figure 4.10a shows the plot of shocked Hα fraction from the total Hα emission line versus projected separation between galaxies. Assuming that the separation is a sign of merger stage, close pairs are in a later stage and closer to coalescence. This assumption is obviously an oversimplification of the geometry and dynamics of the merger.

Similar to Rich et al. (2015) we bin our systems into close and wide pairs and coalesced mergers. Close pairs have projected separation of <25 kpc, and the rest are wide pairs. We selected 25 kpc to have significant statistics in both bins. Figure

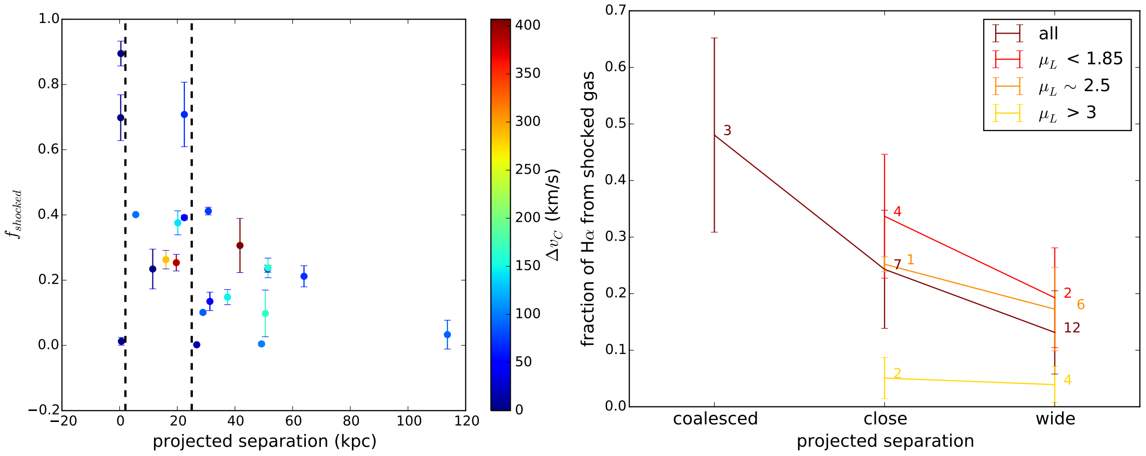

(a) (b)

Figure 4.10: (a)Plot of shock fraction vs. projected separation between the two galaxies color coded with difference between the velocities in the core. One can see an anti-correlation. Close pairs display more shock fraction and wide pairs show less. two of the coalesced systems show shock fraction higher than $> 80\%$ and one has a shock fraction of < 10 %. Vertical dashed lines show the separation used for binning in (b). Close pairs are the ones with separation <25 kpc. The rest are considered as wide pair. The anti-correlation is clear and significant across all mass ratios. Also note that more equal mass merger tend to have higher shock fraction. Next to each point we have written the number of systems in that bin.

4.10b shows the trend in these bins for different mass ratio bins. We can see that not only close pairs are clearly more shocked than wide pairs, but also more equal mass mergers have notably more shocks. Similar to Rich et al. (2015) we find the highest shock fraction in the coalesced systems.

Another way to find this trend between close pairs and wide pairs is to look at [N II]/Hα vs. velocity dispersion plots themselves, separating components from coalesced, close pairs, and wide pairs. Comparing Figure 4.11 for close and wide pairs shows a significant shift of the population upward (and slightly rightward) in close pairs, a signature of enhanced shock ionization. This plot not only confirms the

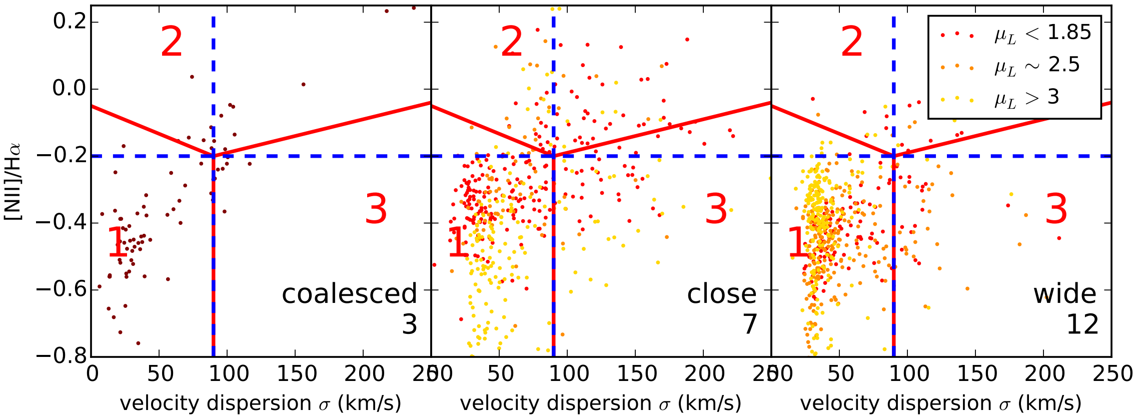

Figure 4.11: Plot of [N II]/Hα vs. velocity dispersion for all components in wide pairs (right) close pairs (middle), and coalesced systems (left). The number of galaxies in each bin is shown on the panel. The significant rise of components even in the part corresponding to star forming area (group 1), is another indication that close pairs has more shocks. This is not obvious for the coalesced systems. In the two plot on the right components of systems with different mass ratio bins are plotted with different colors. There is not a significant difference in wide pairs. In close pairs, however more equal mass merger components have higher [N II]/Hα . We will discuss this in §4.5.5.

result of Figure 4.10b, but also provides some extra information. It is not only the percentage of points in groups 2 and 3 that increases in panel of close pairs if Figure 4.11, but also the points in group 1 show higher excitation and slightly higher velocity dispersion. Different light ratio bins are also separated in these plots. One can see that in close pairs more equal light components stand slightly higher than the other two light ratio bins.

If Figure 4.11 the coalesced systems do no show significant enhancement in the number of higher exited components. This may be due to the small statistics and the fact that most of these components are the star forming components of NGC 3509. However, the few components in the groups 2 and 3 display enough Hα to bring the average shock fraction of this bin to more than 50%. This is shown more clearly in Figure 4.12 which shows the flux weighted histogram of velocity dispersions in these three bins. Again, we see a more prominent peak in the Hα flux of coalesced systems at high velocity dispersions. The close pairs also show more flux at high velocity dispersion compared to wide pairs consistent with Figures 4.10b and 4.11.

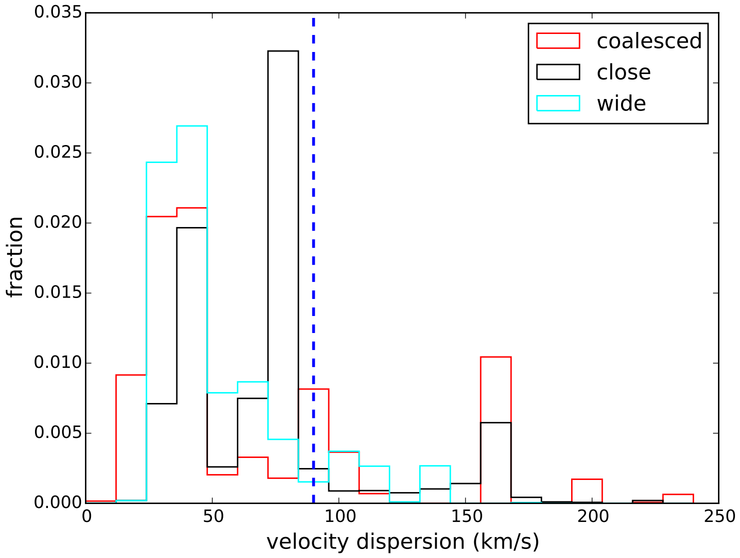

Figure 4.12: Hα flux weighted histogram of velocity dispersions for different separation bins. Similar to Figure 4.6 coalesced systems have a higher peak at high velocity dispersions. Close pairs also show more flux at high velocity dispersion compared to wide pairs.

We should keep in mind that small projected separation is not necessarily a signature of late stage merger. There other factors than can determine the projected separation. First is the geometry of observation. Projected separation is not always correlated with the actual separation. We may find a pair at large distance that look close to us because of the geometry of our line of sight. In addition, a pair of galaxies just after the first passage look as close to each other as a pair that are about to coalesce. Moreover, distance between the interacting pair of galaxies at the pericenter, R_{peri}, also affects how far they appear to a random observer. For better constraints on these encounter parameters we need to model the dynamics of the merger. We will discuss this in §4.7.

4.5.5 Shocked Gas and Merger Mass Ratio

One of the benefits of having a sample of early stage mergers before coalescence is that we can explore how properties of the companion affect the other galaxy. We can find out about the properties of the individual isolated galaxies from their cores which supposedly have not lost much of its stellar mass, morphology, and kinematics after the first passage.

One of the properties that is relatively easy to measure at this stage is the mass ratio. If the shocks are produce as the result of mass flows generated by tidal forces, we should find stronger shocks in a galaxy when companion is more massive, as tidal force depends on the mass of the perturber. (See Equation 1.1.) This leads to two predictions: First is that when galaxies have comparable mass the tidal force on both galaxies will be strong during the first passage, and one should expect higher overall shock fraction compared to more minor mergers. Second is that for non-equal mass mergers one should expect a higher shock fraction in the smaller companion as it experiences a more massive perturber.

The mass ratio of the merger can be estimated from the stellar mass ratio, if we assume that the halo mass proportionally grows with stellar mass. We use 2MASS survey Ks-band magnitude to estimate stellar mass ratio in the two galaxies. Figure 4.13a shows the plot of shock fraction vs. light ratio in separated pairs of our sample. Similar to what we did for separation we bin light ratio, μ_L, into 3 bins: $\mu_L < 1.85$ representing the more equal mass mergers. $1.7 < \mu_L < 4$ representing major galaxy merger of non-equal mass, and $4 < \mu_L$ representing minor galaxy merger in our sample. The dividing values are arbitrarily chosen to have enough galaxies in each bin. In Figure 4.13a vertical dashed lines show the separating limits of light ratio. Figure 4.13b shows the the overall trend in these bins. The first prediction is somewhat verified. The total shock fraction is slightly enhanced in more equal mass mergers. However, we are careful about this interpretation as in such low statistics removing one or two systems can change the conclusion. The second prediction, is not verifiable with our data as the scatter in shocked fraction in secondary galaxies is too large.

Figure 4.14 shows the different position of components in these light ratio bins on plots of [N II]/Hα vs. velocity dispersion. This confirms that in more equal mass mergers components generally have higher [N II]/Hα and higher velocity dispersion compared to more minor mergers.

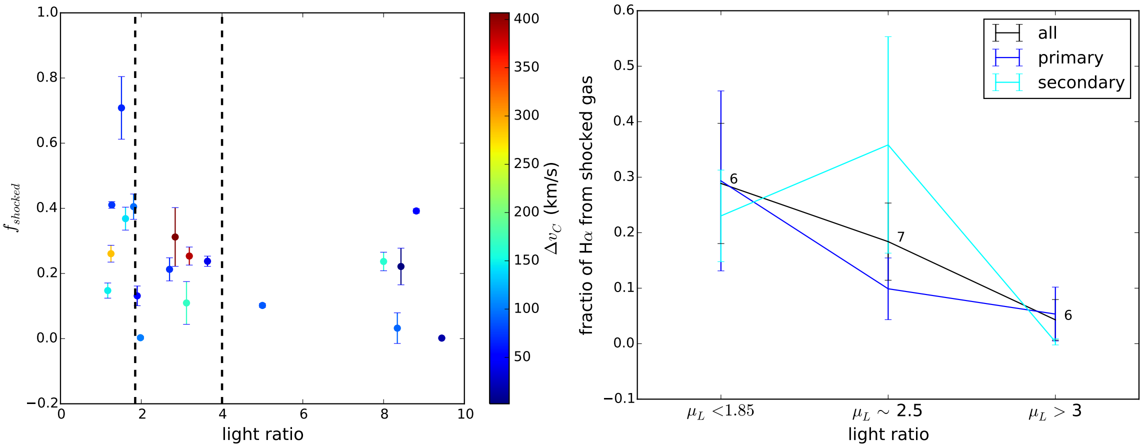

(a)

(b)

Figure 4.13: (a) Plot of shock fraction vs. light ratio in separate pairs of our sample. Vertical dashed lines show the light ratio bins used for binning systems in (b). Equal mass mergers have a higher overall ionization fraction, as was expected. However one should be cautious about these results because of low statistics. The difference between shock fraction in primary and secondary galaxies is not significant in these bins.

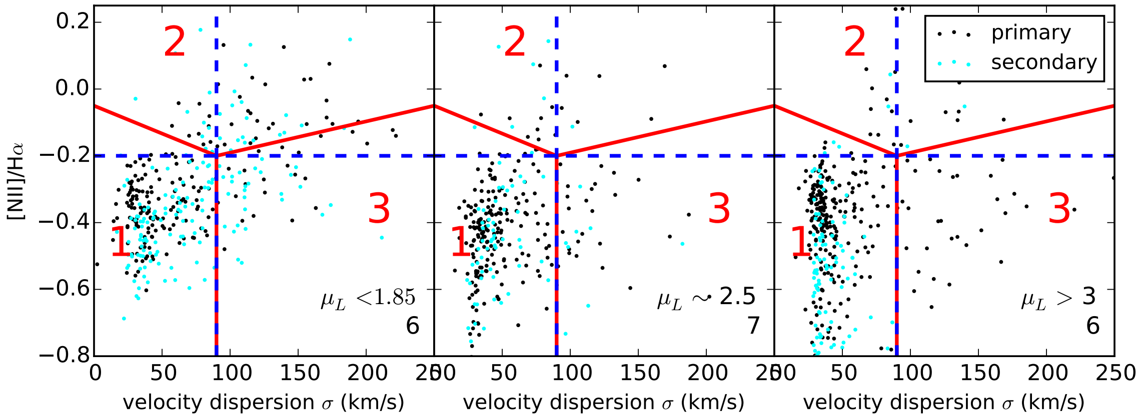

Figure 4.14: Plots [N II]/Hα vs. velocity dispersion for all components in bins of light ratio (left) $\mu_L < 1.85$ (middle) $1.85 < \mu_L < 4.0$, and (right) $\mu_L > 4.0$. One can see that from left to the points in the left plot have slightly higher [N II]/Hα and velocity dispersion.

4.6 Encounter Parameters of Equal Mass Mergers

In Chapter 2 we described a method for measuring the encounter parameter of galaxy mergers. Our method uses Identikit (Barnes & Hibbard, 2009; Barnes, 2011), a software package for modeling the dynamics of interacting pairs of disk galaxies. Identikit galaxy models contain spherically symmetric distribution of massive collisionless particles to reproduce the potential of dark matter halo, and stellar bulge and disk. To represent visible morphology and kinematics of disks, however, these models include massless test particles initially in circular orbits. as the galaxies interact massless test particles move according to the potential made by the massive particles. Test particles have been shown to be successful in producing the large scale tidal features in the disk-disk galaxy merger (Dubinski et al., 1999). As they are massless, multiple disks in a single galaxy will not affect each other, so we can make models of as many disks as we want in a single simulation run. This facilitates relatively rapid exploration of encounter parameter space to find the best model that matches the data.

In this section we use our method to put constraints on the initial conditions systems observed for this Chapter. As we have only tested equal mass Identikit models, we apply our method on the systems that have Ks-band light ratio ≤ 1.85. These are the systems in the first light ratio bin in §4.5.5.

We discussed in Chapter 2 that velocity information on the tidal features of the galaxy merger is required to break the degeneracy between possible encounter parameters. In Chapter 3 we discussed the effect of using different kinematic tracers for modeling the Mice galaxy merger, concluding the we have found consistent results between models of HI and Hα . In this work we use the kinematics of Hα emission from normal HII regions. We showed in §4.5.2 that velocity maps of these components show normal rotation in the center of most of our observed systems. This must agree with with the velocity of the bulk of baryons (stars and cold gas), and it is less affected by non-dynamical processes such as winds from starburst, SNe, or AGN.

For a set of Identikit models with a range of encounter parameters we calculate the goodness of the fit based on the "score" measured by Identikit. To calculate the score we put phase space boxes on the tidal features of the interacting galaxies. Identikit calculates the score for each model based on the number of test particles that populate these boxes. We use the same algorithm that we used in Chapter 3 for selecting the boxes. The size of the phase space boxes were determined by the diameter of the SparsePak fibers ($5''$).

We classified our tests in Chapter 2 into three levels of convergence based on the distribution parameters in models with high enough scores. When it is well converged we found that the measured encounter parameters have either little systematics or the systematics are controllable. In these tests, we can trust the constraint we put on most of the parameters. However, fair or poor convergence showed to lead to

system name	light ratio	separation (kpc)	previous models
UGC 07593	1.81	5.6	—
NGC 5257/8	1.17	33.8	Privon et al. (2013)
UGC 12914	1.61	14.8	Vollmer et al. (2012)
Arp 238	1.51	19.7	—
Arp 87	1.27	2.5	—

Table 4.3: List of systems we attempted to model using our method. The light ratios are obtained from 2MASS Ks band, except for UGC 07593 which is not resolved in the 2MASS Ks survey, and we used SDSS r-band light ratio instead.

unreliable constraints. We determine the convergence by the distribution of initial orientations of the disks in models that are within one σ of the best-fit model. When these distributions show a narrow peak, we conclude that a subset of Identikit models with close initial orientations have resulted in the best scores. and we can determine the constraints on our on the encounter parameters by the extent of these models in the parameter space. On the other hand, flat distributions of disk orientations suggest that disks with a variety of orientations, and subsequently, with a variety of encounter parameters have all resulted in good scores, so the encounter parameters are less constrained.

4.6.1 Systems Selected for Dynamical Modeling

Table 4.3 shows the systems we selected for dynamical modeling. They are the most equal light systems based on their K-band light ratio obtained from the 2MASS galaxy survey (Skrutskie et al., 2006). K-band magnitude can be used as a crude estimate of the stellar mass of a galaxy We selected the galaxies with light ratio less that 1.85, and attempted to model them with equal mass Identikit models. For two of these systems we found prior dynamical models in the literature. In Table 4.3 we show previous attempts for modeling the dynamics of each of these systems.

NGC 5257/8 is previously modeled by Privon et al. (2013). They model this system using Identikit I and via visual comparison of the model with HI data. The HI data reveals a significantly longer tail in NGC 5257 extending more than twice the size of stellar tail. Privon et al. (2013) only test equal mass models with eccentricity of 1. The best model they find has a relatively large pericentric distance (0.625 R_{vir}=21 kpc). They find that this system is at an early stage about 1/7 of the time between the first pass and the second passage. NGC 5258 is almost prograde ($i = 15°$) while NGC 5257 is almost polar ($i = 85°$). Because of the large pericentric separation, it takes a long time until they coalesce ($\approx$ 1200 Gyr).

UGC 12914 reveals a very different morphology when observed in radio continuum, X-ray, or with atomic and molecular gas (Condon et al., 1993; Braine et al., 2003; Gao et al., 2003; Appleton et al., 2015). In all of these bands it glows in the bridge region between the two galaxies. The strong difference in the morphology and kinematics of gas and stars in this system suggest that the gas have undergone significant dissipation in the merger process. We will discuss the physical processes in this system in the light of our IFU observation in the Appendix.

Vollmer et al. (2012) have tried to model the dynamics of UGC 12914. Their primary goal have been to reproduce the morphology and kinematics of both gas and stars, so their model includes collisionless halo particles and stars along with collisional sticky gaseous particles. The complexity of the model they have used leaves little room for scanning large subset of parameter space and find accurate constraints on the encounter parameters. They first make a set of ≈ 20 head-on collisions ($R_{peri} = 0$) with mass-ratio 1:3. In these simulations, they vary the inclination of disks and the cross section of gaseous cloud particles. After finding the best parameters from their set of models, they run a second set by varying the impact parameter. Their best-fit model has an impact parameter of 1-2.5 kpc, and the maximum relative velocity between the two galaxies at the time of the first passage is 1080-1120 km/s. They find the galaxies to be 23 Myr after the pericenter.

4.6.2 Results

We obtained good convergence only for UGC 07593. Here we present the encounter parameters we found for UGC 07593. We also discuss the possible reasons for the failure of our method in dynamical modeling of other systems.

4.6.2.1 UGC 07593

Figure 4.15 shows slices of the map of scores across three encounter parameters, eccentricity, pericentric distance, and time since pericenter. The slices are taken at the best-fit parameters shown by the cyan box. This system is at a relatively late stage at $0.68\pm^{0.08}_{0.01}$ of the time between the first passage and the second passage. The

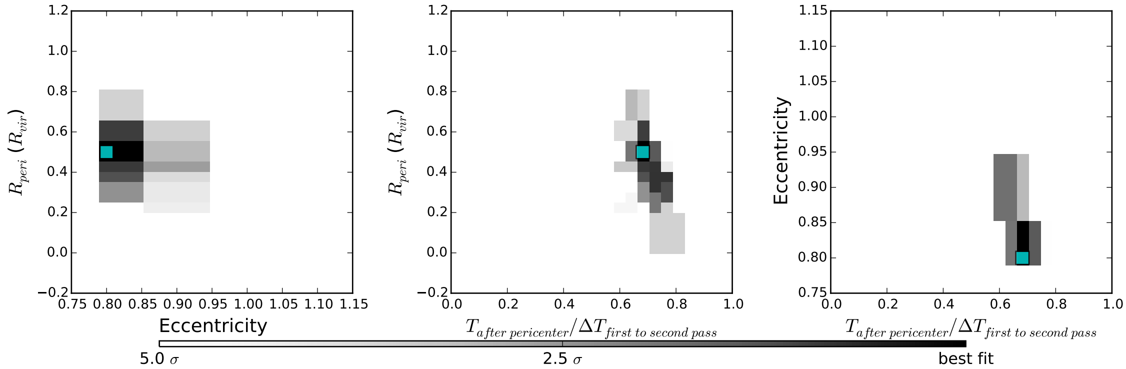

Figure 4.15: Three slices of the score map across pericentrinc distance, time, and eccentricity. for modeling UGC 07593. The slices are taken at the best-fit parameter point, shown by the cyan box. the grayscale shows the goodness of the fit from black (the best-fit model) to white (5 σ from the colorbar).

pericentric distance is measured to be $0.50 \pm^{0.16}_{0.16}$ R_{vir} and eccentricity is $0.8 \pm^{0.05}_{0.05}$.

Figures 4.16 and 4.17 show the distributions of different parameter in the models within 1 σ of the best-fit model. The variation of parameters in these distributions determine the accuracy of the measurement of each model. The measured physical time since the two galaxies first passed by each other is $27 \pm^{30}_{3}$ Myr. The physical pericentric distance is $2.5 \pm^{0.6}_{0.7}$ kpc. Both galaxies are relatively prograde with inclination being at about 45° from the orbital plane. The uncertainty of this angle is about ±20° for both galaxies.

4.6.2.2 Unsuccessful Attempts

We looked more carefully at the systems with unsuccessful dynamical model to come up with possible reasons for poor convergence. In this section we present briefly our notes on each of these systems.

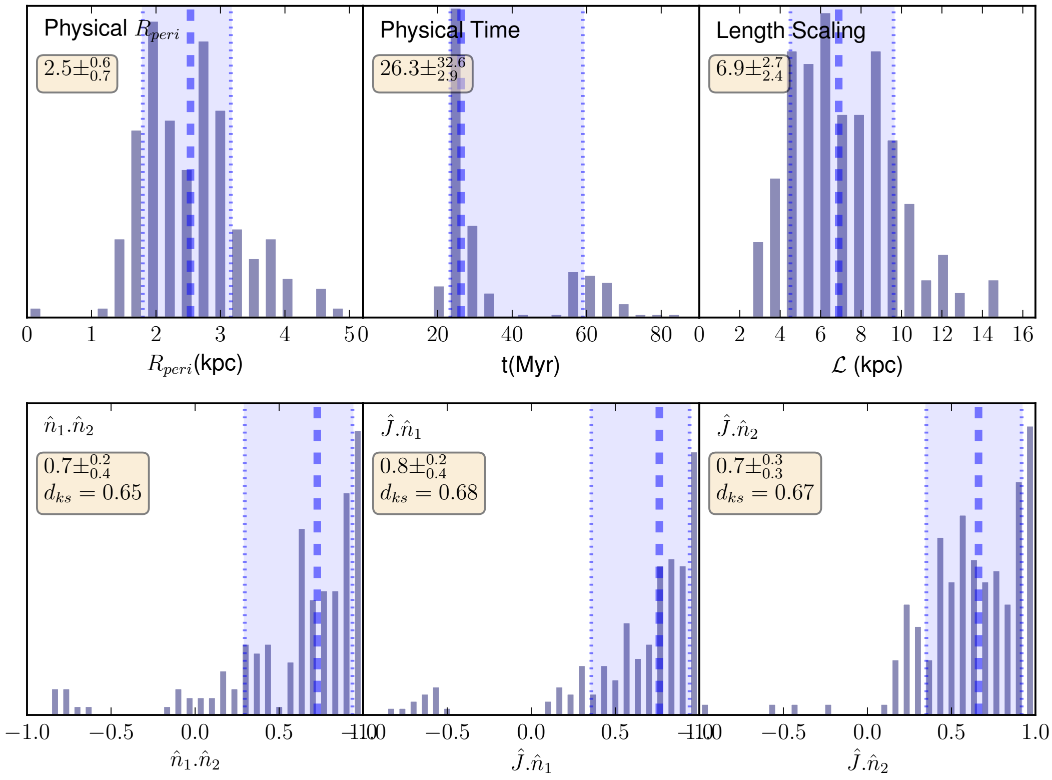

Figure 4.16: Distribution of parameters in models within one σ of the best-fit model. $\hat{n_1}.\hat{n_2}$ is the dot product of the orientation of the to galaxies, and $\hat{J}.\hat{n_i}$ is the dot product of the orientation of each disk with the direction of orbital angular momentum. This confirms that both galaxies have been in prograde orbits.

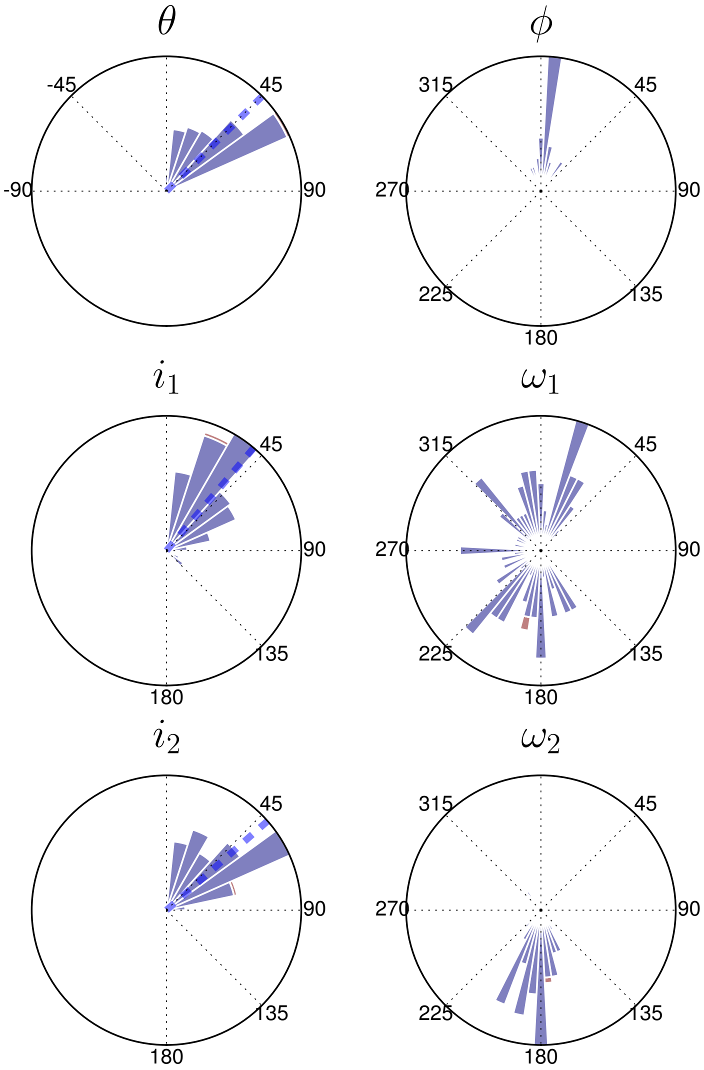

Figure 4.17: Distribution of angles in parameters within 1 σ of the best fit model. The best fit viewing direction is a tilted view with $\theta \approx 45^\circ$ and $\phi \approx 0^\circ$. i_1 and i_2 show the inclination of the two disks, both peaking close to 45°. Since i_1 is slightly closer to 0°, the corresponding argument of periapsis ω_1 is not well constrained. Disk 1 orientations in these models are so close to the pole that the change in ω_1 does not affect them much. For disk 2, argument of periapsis ω_2 is well-constrained around 180°.

UGC 12914: It was easy to predict that our method would not be able to find a good answer for this system by looking at its velocity map shown in Figure 4.8. Fibers with strong Hα line emission are scattered in the region between the two galaxies. The velocity of group 1 components do not show an smooth rotation. The gas in the bridge also shows significant number of shocked components. All of this, along with the detection of significant HI, CO, radio continuum, and X-ray in the bridge suggest that gas of the two galaxies have been stripped off as a result of a close head on encounter. Gas does not follow the rest of the baryons anymore and it can not be reproduced by Identikit test particles.

NGC 5257/8: NGC 5257 has a prominent tail in HI that is absent in the optical image. This prominent tail played an important role in the modeling by Privon et al. (2013). Without the information in the extended tail we do not have the same constraints on encounter parameters. On the other hand, the model presented by Privon et al. (2013) suggests that NGC 5258 is in a polar orbit. In Chapter 2 we performed two tests on interacting galaxies in polar orbits, and none of them were well-converged, so assuming that model of Privon et al. (2013) is correct we should have expected similar failure.

Arp 87: This system consists of one edge-on and one close to face-on galaxy, so even without knowledge of the orbit, we know that one of the galaxies is likely to be close to a polar orbit, and the limitation of our method in modeling polar mergers applies. Moreover, while we found smooth Hα velocity information near the center of of both disks, the tail did not display detectable Hα emission. Lack of velocity information in the tails introduces more degeneracy in possible dynamical models and makes it hard to find good convergence.

4.7 Discussion

In this Chapter we measured the Hα kinematics of a sample of 22 galaxy mergers. Nineteen of these mergers are in the stage between the first passage and the coalescence and the other three are already coalesced. All of these mergers are the result of interaction between rotation-supported disk-dominated galaxies, because all of them display strong elongated tidal features. These features do not survive if the interacting galaxies are dispersion-supported. We know all pairs in our sample are being observed after the first passage, because tidal features seen in these systems are produced by the tidal impulsive force that the galaxies experienced during a close passage. (See Chapter 1.) Tidal forces produce deformations that grow with time. The striping of mass by the tidal features and dynamical friction removes angular momentum from the orbit of the galaxies, and the orbit decays rapidly. The galaxies coalesce in a short time after the second passage.[7] So we can confidently say that most of the pairs in our sample are between the first and the second passages.

We examine the power source of ionization in these mergers using the kinematics and flux ratio of Hα and [N II] emission lines. We used empirical cuts of velocity

---

[7] short time, relative to the time between the first and second passages.

dispersion and [N II]/Hα to separate Hα emission from shocks and star forming regions. In many of these systems there is evidence in the [N II]/Hα maps indicating that the components selected as shocks are indeed powered by shocks. We find that close pairs of galaxies with projected separation $< 25km/s$ have a higher fraction of shocked Hα emission compared to wide pairs with projected separation $> 25km/s$. The average of the shock fraction in the coalesced systems is even higher; shocks are responsible for an average of about 50% of Hα emission in these systems. This suggests that sequence of wide pairs, close pairs, and coalesced mergers is a time sequence consistent with Rich et al. (2015); wide pairs are early stage with more time left to coalescence, and close pairs are late stage near coalescence.

However, dynamical modeling, which incorporates the complex morphology and kinematics of tidal features, is required to constrain encounter parameters in most galaxy mergers. Determining merger parameters such as merger stage, only using the separation between the pairs is not alway correct. Geometry of the encounter and observer can give a close projected separation to a physically wide pair. Moreover, a pair right after the first passage appears as close as one near coalescence. The impact parameter of the encounter also affects the appearance of projected separation during the encounter.

In the second Chapter of this thesis we developed a new automated method to model the dynamics of galaxy mergers and constrain their encounter parameter. Our method is distinguished from previous modeling methods by being automated, less subjective, and providing well-defined errors of the measured quantities. We applied this method on the equal light (mass) pairs ($\mu_L < 1.85$) observed in this Chapter. We only found good convergence in one of them (UGC 07593).

With the model of UGC 07593, we have dynamical models of five of the merger systems in our sample. We modeled the Mice galaxies (NGC 4676) in Chapter 3. The Mice, NGC 5257/8 and NGC 2623 are among the four systems model in Privon et al. (2013). We also find a dynamical model of UGC 12914, Arp 284 in Vollmer et al. (2012) and Struck & Smith (2003), respectively. The measured time since the first passage, time left to coalescence and pericentric separation of these models are shown in Table 4.4 along with the measured shocked Hα fraction.

Table 4.4: List of systems with available dynamical models. The source of the model, time since pericenter, time left to coalescence (Δt), pericentric separation (R_{peri}), and fraction of shocked Hα emission ($f_{shocked}$), are shown. All of these systems except UGC 12914 have been modeled with equal mass galaxies. Mass ratio of the model of UGC 12914 is 3. Vollmer et al. (2012) and Struck & Smith (2003) do no provide the time left to coalescence in their models. The table is sorted by shock fraction.

system name	source	time (Myr)	Δt (Myr)	R_{peri} (kpc)	$f_{shocked}$
NGC 5257/8	Privon et al. (2013)	230.0	1200.0	21.0	0.15
NGC 4676	this chapter	190.0	775.0	18.0	0.26
UGC 12914	Vollmer et al. (2012)	26.0	-	1.2	0.37
Arp 284	Struck & Smith (2003)	170.0	-	6.5	0.39
UGC 07593	chapter 3	27.0	12.0	2.5	0.40
NGC 2623	Privon et al. (2013)	220.0	-80.0	1.0	0.90

Table 4.4 is sorted by shock fraction. One can see that time since pericenter varies with no obvious trends, but time till coalescence, Δt, displays a trend of small shock fraction for systems with long times until coalescence to large shock fraction

for systems near coalescence or after coalescence. Vollmer et al. (2012) and Struck & Smith (2003) do not provide Δt in their model.

The pericentric separation is also almost sorted in Table 4.4. Systems with wide pericentric distance have less fraction of shocked Hα than systems with small pericentric distance. This trend and the trend of time till coalescence is shown in Figure 4.18.

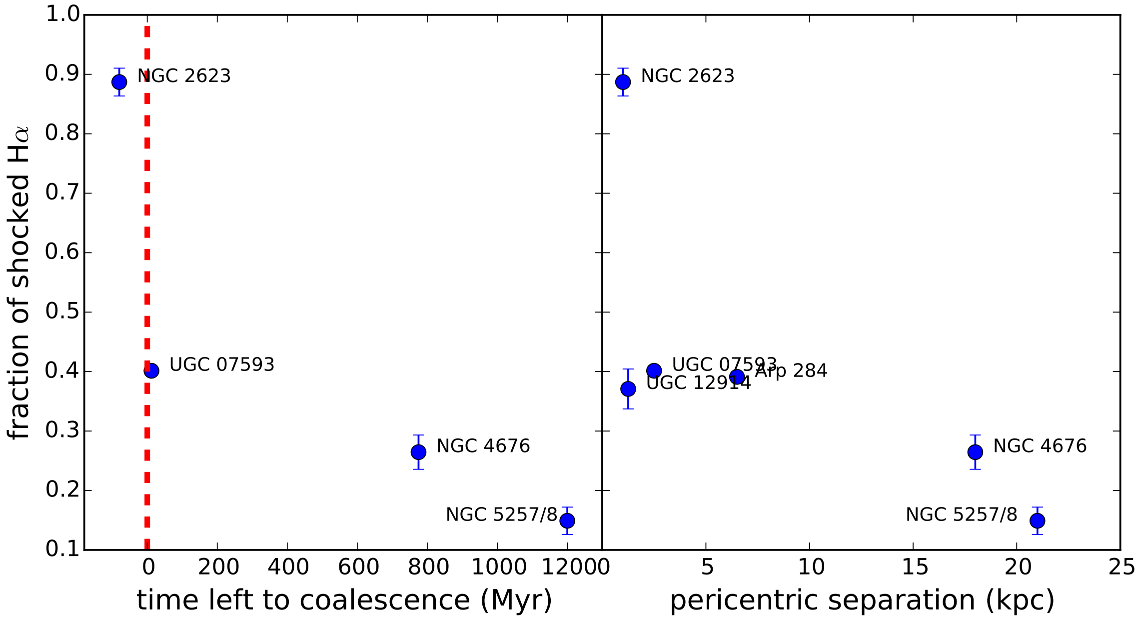

Figure 4.18: The left panel shows how shocked Hα emission changes with time until the galaxies coalesce in the four systems for which dynamical model provides this information. The red dashed line is the time of coalescence. The right panel shows the trend with pericentric separation.

Production of shocks is a complex process and can not be reduced to simple correlations like the ones in Figure 4.18. Shocks can be produced during interaction of galaxies in two different modes. The first mode is initiated by the tidal impulse.

As was described in the introductory Chapter, the tidal impulse at the time of the first pericenter derives the rotating gas in the disks to flow in toward the center of the galaxies. The inflowing gas collides with the gas at lower orbits and if the collision is fast enough shocks can be produced. The inflowing gas may also reach the core of the galaxies and trigger or enhance starbursts or AGN. Starbursts and AGN produce fast outflowing material that can collide with gas clouds on their way out and produce shocks. In this mode shocks are produced a few dynamical times after the tidal impulse kicks in. This mode is a side effect of the gravitational tidal impulse during the close passage, so factors that affect the tidal impulse should affect the shock production from this mode.

Pericentric distance, for example, strongly affects the amount of tidal acceleration induced in the interacting galaxies at the time of the first passage. From Equation 1.1 we know that the tidal response is proportional to the inverse cube of the distance to the perturber. A factor of two in pericentric separation changes the tidal impulse induced at the time of pericenter by a factor of eight. Tidally induced inflows are also more prominent in prograde encounters, where the orbital angular momentum is aligned with disk spin. In prograde disks the tidal acceleration during the close passage pushes or pulls the rotating material in the same direction at all times during the passage, and the resulting tidal effect is maximized. So, we expect to find stronger shocks of this mode in prograde mergers with small pericentric separation.

In a second mode, sometimes, the geometry of galactic encounter allows the ISM of the two gas rich disks to directly collide with each other. For this to take place, the two disks should have small enough distance at the pericenter of their orbit, so that the disks and not just the dark matter halos cross during the first passage. The shocks are produced immediately during the first passage, and decay as they cool down via radiation. Unlike the other mode of shock production, this one is less likely to happen in prograde disks, because the overlapping rotating material move in the same direction in prograde disks. So, in this mode of shock production, one expects to find more shocks in retrograde and polar disks at small pericentric separation.

From the geometry of Hα emission it is clear that UGC 12914 is producing shocks in the second mode. The presence of the continuous gaseous bridge observed on different bands suggest that gas has been striped from the two galaxies because of the recent head-on encounter. Vollmer et al. (2012) model suggests that the relative velocity of galaxies at the time of the encounter was $\approx$ 1000 km/s. Gas clouds in the ISM of the two disks have collided at this speed and dragged themselves away from the stars in the disk toward the bridge region. If Vollmer et al. (2012) had provided the time until final coalescence, we expect that to be a long time as the galaxies are observed to be still receding from each other. This would be inconsistent with the trend we see in Figure 4.18 for time left to coalescence. We suggest that this is an indication that the shocks in this galaxy are produced in a fundamentally different procedure.

Pericentric separation affects the shock production in the same way in the two proposed modes of shock production. The smaller pericentric separation of the encounter is, the stronger tidal impulse is induced, and the stronger shocks via the fist mode is produced, subsequently. Also, small enough pericentric separation results in direct collision of gas in the ISM of the two disks, producing shock. This hypothesis, is consistent with the trend that we see in Figure 4.18. However, after the coalescence violent relaxation produces shocks via complicated processes, and our simple shock production modes may not apply then. One may find strong shocks in a recent remnant of a merger with large separation at first passage.

Both modes that we proposed for shock production, can remove or heat up the cold gas reservoir in the disks which is the fuel for star formation, and hence contribute to quenching. Investigating mechanisms that produce shocks is useful to understand what quenches star formation in galaxies. In a simplified picture, we expect galaxies to become quenched after a short period of being highly shocked throughout their gas content. If shocks are made by strong galactic winds or by direct collision of gas in the disks, they move the cold gas away into the hot gaseous halo (Cox et al., 2006b; Oppenheimer et al., 2010). The gas may not be able to come back to its cold state on the disk due to gravitational shock heating (Birnboim & Dekel, 2011). Understanding the timing of possible quenching from shock production in mergers requires larger statistical sample of galaxy mergers observed with optical IFU instruments. Ongoing and future IFU galaxy surveys (e.g. SAMI, MaNGA, etc.) provide a promising area for this field in near future.

4.8 Summary

In this Chapter we observed 22 galaxy mergers with strong tidal features, using the SparsePak IFU on WIYN telescope at KPNO. We reduce the data, and analyze the emission line using one and two overlapping Gaussians. We use an MCMC code to estimate the uncertainty of fit parameters, and select the best number of components using the F-test. High spectral resolution of our data, allows us to use velocity dispersion of emission lines along with [N II]/Hα line ratios to separate Hα emission of star forming regions and Hα from shocked gas. We use emission line maps to confirm that most of high velocity dispersion and high [N II]/Hα components are galaxy wide shocks, possibly induced by mergers. We found that the fraction of Hα emission from shocked gas is correlated with the separation of galaxies in pairs. Close pairs have higher shocked Hα fraction than wide pairs. The three coalesced systems show the highest average shocked Hα fraction.

We used the modeling method we developed in Chapter 2 along with the velocity maps of star forming regions to model the dynamics of equal mass pairs in our sample. We found the first ever constraints on the encounter parameters of UGC 07593, but obtained poor convergence in the other four attempts. Along with the dynamical model of the Mice galaxies from Chapter 3, we found dynamical models for six of the systems in our sample. In these systems time left to coalescence and pericentric separation appear to be correlated with the fraction of shocked Hα .

Chapter 5

Conclusion

This work presents an investigation of interacting galaxy pairs with tidally disturbed morphology. Galaxy mergers play an important role in the formation and evolution of galaxies, by contributing to the galaxy baryonic mass assembly and transforming galaxy morphology. The formation of today's quiescent ellipticals with a variety of photometric and rotational properties is the possible consequence of their merging history, in which a primary galaxy has been involved in one or more major and/or minor mergers over the past 10 billion years. (Toomre, 1977; Faber et al., 1997; Boylan-Kolchin et al., 2005; Emsellem et al., 2007; Narayanan et al., 2008; Rodriguez-Gomez et al., 2016). Understanding what transforms galaxies from star forming disks at z∼2 to quiescent ellipticals we see today (Bell et al., 2004; Faber et al., 2007; Bell et al., 2012), and the possible role of galaxy mergers in this process is among the important and current questions of the field of galaxy formation.

The properties of the remnant of a pair of merging galaxies depend on their encounter parameters and the amount of gas in the progenitors (Bois et al., 2011; Naab et al., 2014). Encounter parameters of galaxy mergers can be measured using the vast amount information that lays in the complicated tidal structures (Toomre & Toomre, 1972; Hibbard & Mihos, 1995; Dubinski et al., 1999). The task of visually finding a simulation that reproduces morphology and kinematics of tidal features requires a lot of computing resources and expert time. One needs to run a lot of simulations with various encounter parameters, and look at the simulated mergers at different times, from different viewing angles to find the best match to the data. It is possible to exclude a large fraction of parameter space using hints from other observables and experience from systems modeled before (Barnes & Hibbard, 2009; Privon et al., 2013). But, the visual matching can be subjective with different experts obtaining different results. Also the errors of measured encounter parameters are not well understood in visual matching, and the large number of parameters involved makes it hard to ensure that the best matched model is unique.

In Chapter 2 our goal was to develop a new automated method for modeling interacting galaxy pairs. We developed this method based on a software package called Identikit (Barnes & Hibbard, 2009; Barnes, 2011) that combines self-consistent N-body simulations with test particle techniques to reduce the computational demand for producing merger models and searching for a good match. Test particles represent the disks of the merging galaxies. Identikit calculates the "score", an informal measure of goodness of the match, based on how many test particles populate user-selected boxes on the tidal features of data. We developed a pipeline that automates application of Identikit from box-selection to estimation of realistic errors for measured encounter parameters. We test our method against an independent set of hydrodynamical simulations (Cox et al., 2006b) which include various components such as cold gas, old and young stars, and dark matter. In these tests we find that prograde disks are better modeled with Identikit rather than retrograde or polar disks. In prograde encounters most of the times we find better results with gaseous components as they are more extended in the isolated disks and produce stronger tidal features (Hibbard & van Gorkom, 1996b). Though, in a couple of tests, the gaseous components produce tidal tails that were too large and Identikit had trouble reproducing them with the correct initial conditions.

These results suggest that the mass model of the isolated disks in Identikit are important for making just enough tidal features to match observations. Barnes (2016) used this idea to explore a large set of Identikit-like simulations with different mass models for isolated galaxies. He found that the luminous mass fraction[1] in isolated galaxies is the most sensitive internal parameter affecting the morphology of tidal features. In principle, he claims that one may find constraints on internal mass profile of isolated galaxies by careful modeling of tidal structures during interaction. This is a possible future direction for this work. A robust automated pipeline for scanning

---

[1] luminous mass fraction = $(\mathrm{M_{bulge}} + \mathrm{M_{disk}})/(\mathrm{M_{halo}} + \mathrm{M_{bulge}} + \mathrm{M_{disk}})$

parameter space can be used to test Identikit models with different luminous mass fractions and find insights into the internal mass profile of disk galaxies. Similar attempts have been underway to model the internal structure of the Milky Way halo based on morphology and kinematics of its satellites and their tidal streams, particularly the Sagittarius stream (e.g. Law & Majewski 2010). These studies suggest that it is hard to constrain the halo mass profile of an individual system (i.e., the Milky Way), but statistical results for a large number of galaxies may provide insights into the formation of halos in a ΛCDM Universe.

To improve Identikit modeling we suggest to add a few capability to Identikit. We can select boxes based on morphology of tidal features only. In many real interacting galaxies, obtaining kinematic information in the faint tidal tails is hard, and only the morphology of the tails is available. For example, when we use Hα kinematics, sometimes, no Hα emission is found in the tails as in some of the systems we observed in Chapter 4. Low continuum level of stellar light makes it hard to obtain uniform velocity information from stars. Available all sky surveys like SDSS (York et al., 2000) reveal stellar tidal tails in many nearby interacting features. In near future LSST (Collaboration et al., 2009) will provide much deeper photometric data for many more interacting galaxies revealing even fainter features. In Identikit, we can put phase space boxes that only occupy a morphological region, and put no constraints on the line of sight velocity when it is not available.

Identikit can be improved by adding a capability that down-weights test particles which fall in regions with no features. While modeling a pair of interacting galaxies, an experienced user can select regions in phase space that no model particles should be present in a good match. Currently, there is no penalty for having particles where they are not supposed to be, and this causes some of the models with poor match to obtain good scores. We suggest to add a new type of box called “penalty box” to Identikit. The user puts penalty boxes in phase space regions where no particles should be present. If test-particles lay on these regions they would decrease the score of the corresponding model, which then may eventually exclude some of the poor matches, and partly break the degeneracy.

Moreover, it seems that tidal features are not sufficiently strong to constrain the orientation of disks in retrograde and polar mergers, so it is likely that using the information in the kinematics of the cores of the interacting galaxies would better constrain the initial orientation of disks. Often, an expert in modeling mergers can exclude many of the possible initial disk orientations by looking at the rotation curves and morphology of the disks. In the current version of Identikit, the scores are calculated for a complete sphere of possible disk orientations. We suggest to improve Identikit by making the user capable of restricting the range of disk orientations to be searched. This will improve search speed, and will make it more likely to find a correct match as the best-fit model. In the newest version of Identikit, Identikit 3, Barnes (in preparation) have implemented some of these suggestions, such as adding the penalty box and restricting the range of search in disk orientation.

In Chapter 3 we apply our method from Chapter 2 on a well-studied interacting galaxy pair, the Mice (NGC 4676). We use two different kinematic tracers, HI emitted from cold gas, and Hα from star forming regions. Archival HI data is available (Hibbard & van Gorkom, 1996a), and for Hα kinematics we observed the Mice with the SparsePak IFU on the WIYN telescope at KPNO. The resolution of our data allows us to separate shocks from star forming regions using velocity dispersion of Hα line and the ratio of [N II]/Hα . We find that the velocity map of star forming Hα lines are in excellent agreement with HI kinematics. The dynamical models we obtained with HI and Hα were consistent within the reported uncertainty, suggesting that at least for some mergers Hα velocity maps can be used instead of HI for dynamical modeling.

This conclusion is significant because measuring velocity map of Hα lines is much less expensive compared to stellar or HI kinematics. There are massive IFU galaxy surveys such as CALIFA (Sánchez et al., 2012), SAMI (Croom et al., 2012), MaNGA (Bundy et al., 2015), and HECTOR that have observed or will observe resolved optical kinematics of thousands of galaxies including hundreds of mergers. These surveys have different aerial coverage, and spatial and spectral resolution, so they provide Hα velocity maps with various qualities. However, they all provide kinematics near the central regions of galaxies, and with the improvements in Identikit 3 we may be able to put reasonable constraints on the encounter parameter of the observed systems. The vast amount of data available from these surveys makes it is possible to measure reliable encounter parameters for a statistically significant number of mergers and put new cosmological constraints on distribution of galaxy encounter parameters in the nearby Universe.

In Chapter 4, we observed 21 other systems using the same instrument, WIYN SparsePak IFU. Eighteen of these systems have the same visual characteristics of the Mice galaxies, separate pairs with strong tidal features. Three other ones seemed to be recently coalesced mergers with strong signatures of tidal disruption. The same criteria as in Chapter 3 is used to separate shocks and star forming regions in these systems. We applied our dynamical modeling method on five systems with light ratio, $\mu_L < 1.85$, and found converged results in one of them. The other ones mostly appear to be in polar orbit for which tests in Chapter 2 show that our method is usually not successful.

We investigate Hα flux from shocked gas in these systems. To detect the shocks we separate emission line components with high velocity dispersion and [N II]/Hα ratio. In order to confirm that these regions are shocked we study maps of [N II]/Hα . The distribution of these components across the galaxies and the gradient of [N II]/Hα suggest that in most of these systems the components with high velocity dispersion and high [N II]/Hα are indeed from shocked gas. In six systems, these components are only found near the center, and our data does not allow us to confidently determine the source of ionization for them. IFU instruments with higher spatial resolution (e.g. MUSE) can be used to find the source of ionization in these systems (Medling et al., 2015).

We find that shocked Hα fraction in close pairs with projected separation < 25 kpc is higher than wide pairs with separation > 25 kpc, and the coalesced mergers show the highest average shock fraction. These results are in agreement with the results of Rich et al. (2015). Our relatively large sample of separate pairs allowed us to investigate how properties of progenitors affect the shocked gas fraction in a merger. We find that more equal light (mass) pairs are more shocked than minor mergers. Both of these trends are consistent with tidal impulse during the first passage being the primary source of shocks.

In total, for six of the systems observed in this work we find reliable dynamical models. Comparing shocked Hα fraction with other merger parameters we find a trend for pericentric separation vs. shocked Hα fraction; systems with lowest pericentric separation displaying the highest shocked gas fraction and vice versa. This is consistent with two modes for shock production we propose for interacting galaxies at early stages before coalescence. One mode is due to gravitational tidal impulse during the first passage which can derive inflow of gas, trigger central starbursts or AGNs, and make the corresponding outflows, producing shocks. The other mode is from direct collision of ISM in the two disks. Both modes are expected to enhance in close encounters with low pericentric distance.

One of the questions we asked in Chapter 1 is whether we can learn anything about the role of mergers in quenching star formation in galaxies, by studying shocks. As we described in Chapter 1, processes that produce shocks can also be responsible for quenching or regulating star formation. This includes the outflows that produce shocks in the ISM as they swipe gas out of the galaxies (Oppenheimer et al., 2010), and the direct collision of ISM of interacting disks which can move the gas out into the bridge between the two galaxies (Struck, 1997; Amram et al., 1998). Dynamical model of Struck & Smith (2003) for Arp 284 suggests that the secondary galaxy has depleted its gas content into the primary after the first passage. This has left the secondary quiescent. We observe the inflow of gas from the secondary toward the center of the primary confirming this picture for the quenching of the secondary. (See Appendix.) The relation we found between shocked gas fraction and merger stage is consistent with the claim that interactions heat up and redistribute the fuel for star formation and may contribute to quenching. Though, better understanding of merger stage using dynamical modeling, and larger statistical samples are required to further investigate this claim.

Ongoing and Future IFU galaxy surveys (e.g. SAMI, MaNGA, etc.) picture a promising outlook for this field. MaNGA, for example, will observe $\approx$ 10,000 galaxies in the nearby Universe, including more that 100 close pairs. Even though, the spectral resolution of MaNGA data is R$\sim$2000, we show in our preliminary investigation of emission lines that in one of MaNGA galaxy mergers (VV 705), broad shocked components can be separated from narrow star forming ones. We show that even with MaNGA resolution, we are able to fit two components to the emission lines in most of the spexels of this highly perturbed merger.

MaNGA and SAMI mergers also provide the resolved velocity information needed for dynamical modeling of a large sample of galaxy mergers in the nearby Universe. As described in Chapter 1 measuring the encounter parameters of many galaxy mergers provides the statistical sample required for comparing the distribution of galaxy merger parameters with dark matter halo merger parameters in cosmological simulations (Benson, 2005; Khochfar & Burkert, 2006). It is also demonstrated in Chapter 4 that with a large sample of mergers with reliable dynamical models, we can better understand the physics of shock production in galaxy mergers. We have tried to model VV 705 with our modeling method but obtained no convergence mostly because MaNGA fiber bundle does not cover the tidal tail in this system. However, Identikit 3 improvements may be able to find convergence using the available data. Success in modeling VV 705 will determine if our method can be used for further systems in the MaNGA merger sample.

In summary, in this thesis we have developed a new tool for modeling the encounter parameters of equal mass mergers. Our tool has limitations that we studied using mocked data. We applied our method on both HI and Hα kinematics of a well-studied galaxy merger, finding consistent results. This suggests that data from large optical IFU surveys provide the raw material for dynamical modeling of many new systems. We find dynamical model for a system that is never modeled before (UGC 07593). We observe 22 galaxy merger systems with strong tidal signitures, and based on kinematics and [N II]/Hα ratio of emission lines we separated shocks from star forming regions. We find that on average, close pairs are more shocked than wide ones, coalesced systems are more shocked than separate ones, and major mergers are more shocked than minor ones. We present the outlook to improve our results on dynamical modeling and on shock detection in galaxy mergers, and the prospects of future optical IFU surveys.

Appendix A

Notes on Individual Systems

In this Appendix we describe the interesting features we found in some of the observed systems from Chapter 4.

NGC 5257/8: This is a well studied merger system. Our modeling method was not successful in modeling this systems, but Privon et al. (2013) found a model with a relatively large pericentric distance (0.625 R_{vir}) at a very early stage, just after the first pass. For this model, we expect NGC 5257/8 to have little tidal-shocks as only outskirts of the of the disks collide. Cox et al. (2008) shows that with large pericentric separation, the merger-induced star formation occurs at later times, and we do not expect shocks related to the merger-induced starburst at such an early stage. There is no evidence of strong AGN in any of the two galaxies.

This system is also one the systems observed in Rich et al. (2015). Their IFU data covers only the central regions of the interacting galaxies. They find little components

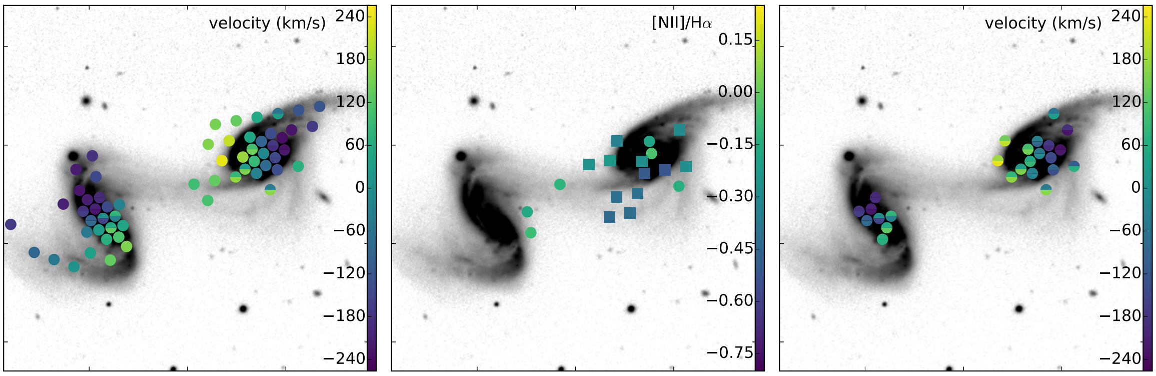

(a) (b) (c)

Figure A.1: **NGC 5257/8**: (a) Velocity map of star forming components. The smooth rotation suggests that their velocity is governed by gravity along with the rest of the baryons. (b) Map of [N II]/Hα for components in groups 2 and 3 expected to be from shocked regions. The low [N II]/Hα ratio and the widespread spatial distribution of these components confirm that they are shocked. This system has a relatively low shocked gas fraction $\approx 15\%$. (c) Fibers for which two-component fit to [N II]-Hα triplet is preferred by the F-test. The colors show the velocity of components, the top half is the velocity of the narrower fit component and the bottom half shows the velocity of the broader one. In this case most of double component fits are of the class of two narrow star forming components falling into the same fiber as a result of tilted inclination of the disks.

with velocity dispersion > 90 km/s consistent with our results ($f_{\mathrm{shocked}} = 0.15 \pm 0.02$). Figure A.1a shows the velocity dispersion obtained in this system. Figure A.1b shows [N II]/Hα ratio maps for group 2 and 3 components. The distribution of these components confirm that the source of ionization is shock as they are located in widespread regions. Similar to Rich et al. (2015), we find slightly more shocks in NGC 5257 (the western galaxy). Figure A.1c shows the fibers in which we found double component fits to be preferred. Most of them are consistent with the class double components fibers in which two narrow star forming are in the same fiber. (See §4.4.2.)

NGC 5278/9: The light ratio based on 2MASS K-band magnitude is 3.19. Repetto et al. (2010) presents scanning Fabry-Perot (FP) Hα observations of this system. They measure different dynamical estimates of the masses of the two systems based on their low resolution Hα kinematics. Rotation curve decomposition provides a dynamical mass of $8.1 \times 10^{10} M_{\odot}$ for NGC 5278, the primary galaxy to west of images in Figure A.2 , but they are unable to find a mass for NGC 5279, the smaller companion, due to the unusual shape of the rotation curve. They also show that simple dynamical analysis, assuming flat disks in both galaxies and using the point of maximum velocity difference on the rotation curve, suggest a mass of $9.7 \times 10^{10} M_{\odot}$ for NGC 5278 and $1.3 \times 10^{10} M_{\odot}$ for NGC 5279. This suggests a mass ratio of ≈ 7, significantly different from the light ratio ≈ 3, suggesting that mass to light ratio differs by more than a factor of two. They also use the rotation near the center, indications for the near side from the dust lanes observed with HST image (Windhorst et al., 2002), and the shape of spiral arms (tidal arms), to argue that both galaxies have trailing arms.

The shocked gas fraction measured for this systems is 25%. In Figure A.2a, we find a disturbed rotation in NGC 5278, and there are only few normal HII region emission in NGC 5279. In both galaxies there is a gap in the center of the velocity field, because those fibers are dominated by shock emission. In particular, in NGC 5278, the void in the velocity map resembles a cone-like structure. This cone-like void is emitting shocked Hα emission shown in Figure A.2b. This is an indication of outflows from central starburst. The other map of [N II]/Hα in Figure A.2b does not show an obvious radial gradient, consistent with shock ionization. Shocks in the center of NGC 5279 explain the unusual velocity field Repetto et al. (2010) obtained by FB Hα observations. This demonstrates the importance of resolving kinematic components with high spectral resolution spectroscopy, and separating the shocked Hα emission for mass profile analysis of velocity curves. It is worth mentioning that Keel et al. (1985) used optical emission line ratios to classify both cores in a class between Seyfert 2 and LINERs.

UGC 480: It is an asymmetric face-on galaxy paired with a smaller edge-on companion to the east. Figure A.3a shows that star formation is happening in almost all parts of the primary galaxy except near the center, displaying an smooth rotation. The eastern galaxy and the central regions of the western one reveal almost no Hα

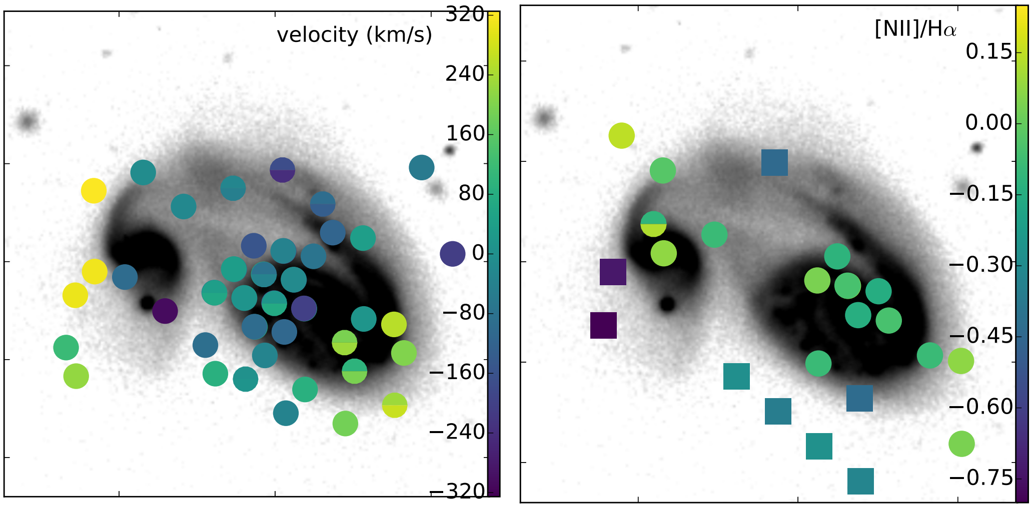

(a)

(b)

Figure A.2: **NGC 5278/9**: (a) Velocity of star forming components. NGC 5278 (primary galaxy - west) displays disturbed rotation. Few star forming components are found near the center of NGC 5279 (secondary). (b) Map of [N II]/Hα for group 2 and 3 components supposedly from shocks. In the center of NGC 5278 we can see a bi-conal structure consistent with shocks due to outflows.

emission, suggesting that they are dominated by older stellar populations.

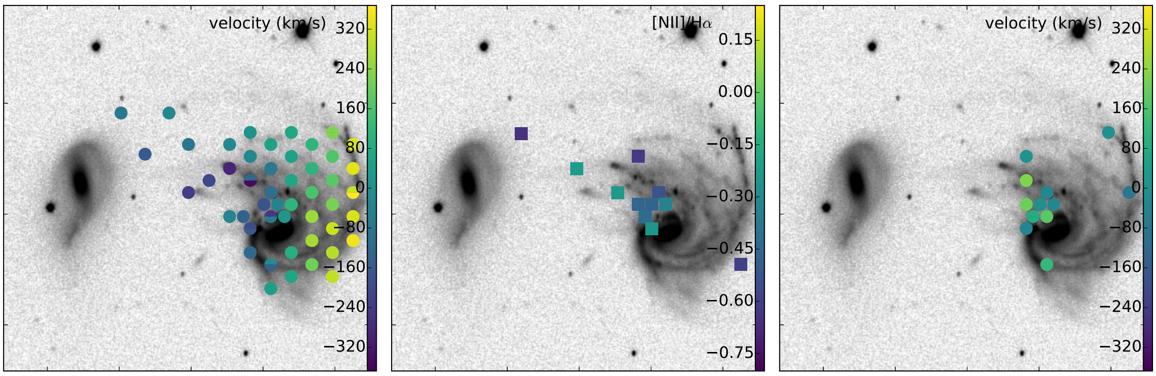

(a) (b) (c)

Figure A.3: **UGC 480**: (a) Velocity map of star forming components. Almost no Hα emission is found in the center of the primary galaxy and throughout the secondary one, indicating old stellar populations. (b) Map of [N II]/Hα for supposedly shocked components (groups 2 and 3). They occupy a particular region east of the primary. (c) The difference in the velocity of broad and narrow components in fibers where double component fit is preferred. It suggests that most of shocked components in panel (b) are blueshifted by 50-150 km/s with respect to star forming components in panel (a).This is suggestive of outflows from individual HII regions in the disk of the primary galaxy.

Shocked components shown in Figure A.3b display a very distinct structure to the east of the primary galaxy. They have relatively low [N II]/Hα ratios and are mostly the wide component of a double component fit. Figure A.3c shows the difference in the velocity of fibers in which double component fit is preferred. It shows the velocity of broad component minus the velocity of narrow component. So, the more broad component is blueshifted with respect to the narrow component the bluer it is shown in this Figure. It can be seen clearly that most of shocked components in Figure A.3b are the blueshifted broad components with respect to narrow star forming components in Figure A.3a. This is a strong evidence for outflows with velocities between 50-150 km/s. The variation of outflow velocities, and the absence of central Hα emission suggest that outflows originate from individual HII regions in the disk, and not from central starburst or ANG.

Arp 283: We did not find Hα emission in the outskirts of the the primary galaxy to the west (NGC 2798). The bar in the center, and the diffuse stellar tidal features suggest that before interaction this was an SBa galaxy with a strong bulge. Figure A.4a is consistent with a strong starburst in the center detected with ultraviolet spectroscopy (Joseph et al., 1986; Kinney et al., 1993), and far-infrared luminosity Armus et al. (1990). Figure A.4b shows group 2 and 3 components which are consistent with shocks produced by outflows from the central starburst. The secondary galaxy is an edge-on star forming galaxy, displaying rotation, and little shocked gas emission.

Arp 256: Both galaxies show smooth rotation with star forming regions present out to the end of the visible tidal tails in the SDSS r-band image shown in Figure A.5a. The southern galaxy looks smaller in the SDSS r-band image, though its 2MASS Ks-band flux is almost twice the northern galaxy. So we take the southern galaxy as the primary.

The primary shows broad group 3 components on both sides of the disk in the vicinity of the center shown in Figure A.5b. There are also three group 2 and 3 components to the south-west of the core of the secondary. This system is a LIRG with FIR luminosity of $\log(L_{\mathrm{FIR}}/L_{\odot}) = 11.27$ (Sanders et al., 2003), indicating a

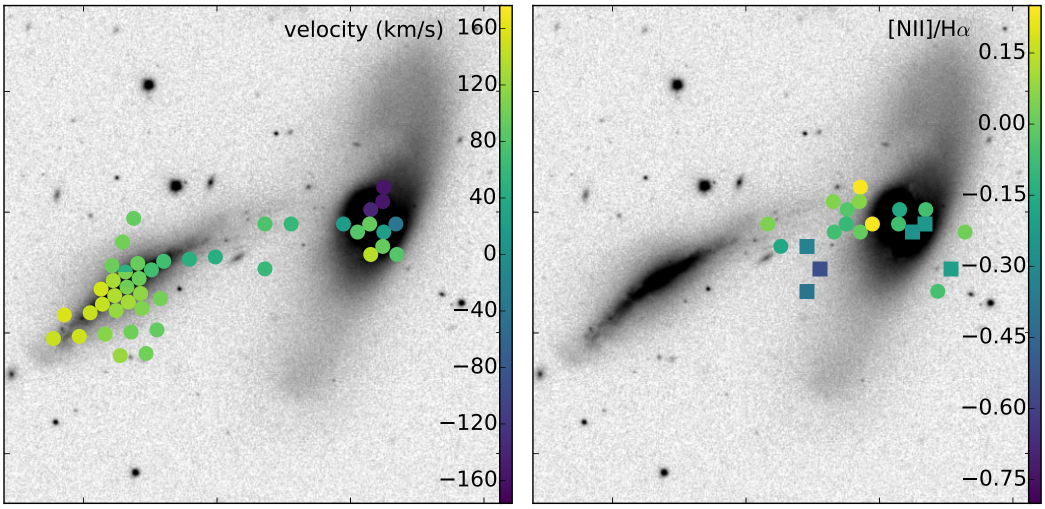

(a) (b)

Figure A.4: **Arp 283**: (a) Velocity map of star forming components. The secondary galaxy displays star formation all over the galaxy. The primary galaxy has strong starburst in the center (Armus et al., 1990) but no star formation in the tidal tails. (b) Map of [N II]/Hα for the supposedly shocked components of groups 2 and 3. Their spatial distribution is consistent with shocks produced by outflows from the starburst in the center of the primary galaxy

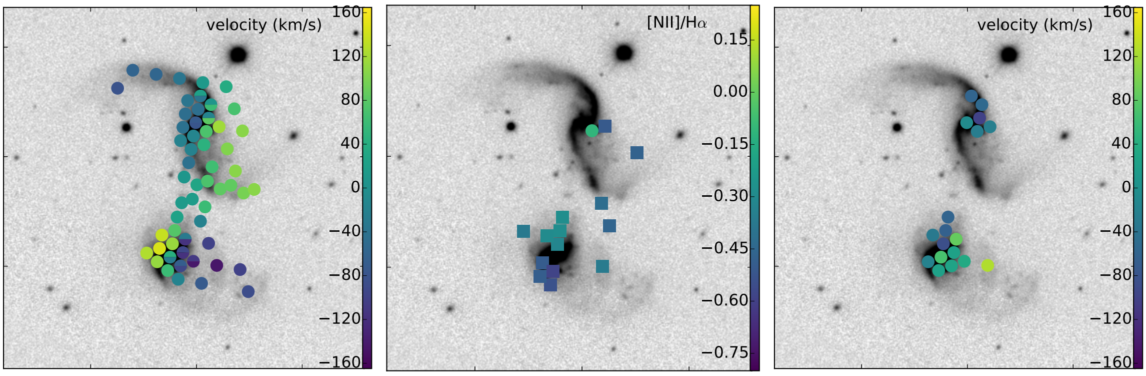

(a) (b) (c)

Figure A.5: **Arp 256**: (a) Velocity map of the star forming components (group1) displaying smooth rotation and star formation all over both galaxies. (b) Map of [N II]/Hα for group 2 and 3 components. Their low overall [N II]/Hα and spatial distribution suggest that they are mostly produced by outflows from central starburst. (c) Map of difference between the velocity of broad and narrow components in fibers where two-component fit is preferred. It shows that most of shocked components in panel (b) are blueshifted by 40-80 km/s with respect to narrow star forming components in panel (a) strong starburst. So, the spatial distribution of group 2 and 3 components in Figure A.5b is indicative of central starburst outflows, particularly in the primary (southern) galaxy. This is confirmed by Figure A.5c which shows the velocity difference between broad and narrow components in fibers where two-component fit is preferred by the F-test. It shows that broad shocked Hα emission in Figure A.5b is blueshifted with respect to star forming components in Figure A.5a, by velocities in the range of 40-80 km/s.

Arp 284: In the secondary galaxy (NGC 7715) we only detect Hα emission in the outskirts of the edge-on disk, shown in Figure A.6a. There are HII regions in the tidal bridge between the galaxies. Smith & Wallin (1992) finds HI bridge coincident with the optical bridge. The western primary galaxy (NGC 7714) displays smooth rotation in the star forming components, scattered all over the tilted disk.

This system is studied extensively in the literature. Delgado et al. (1998) used HST/GHRS ultraviolet spectroscopy and ground based radio, optical, and X-ray observations to perform a spectral synthesis modeling on central 300 pc of the primary galaxy. They suggest that the center of this galaxy contains a very young starburst (4.5 Myrs) along with an older stellar population with age of tens of Myrs or older. Dynamical modeling by Struck & Smith (2003) indicates that a significant amount of gas is being transferred from the smaller companion to the the primary galaxy after the first passage, which occurred $\approx$ 170 Myr ago. This gas transfer is fueling the starburst in the core of NGC 7714. It is the gas loss and lack of mass input that have

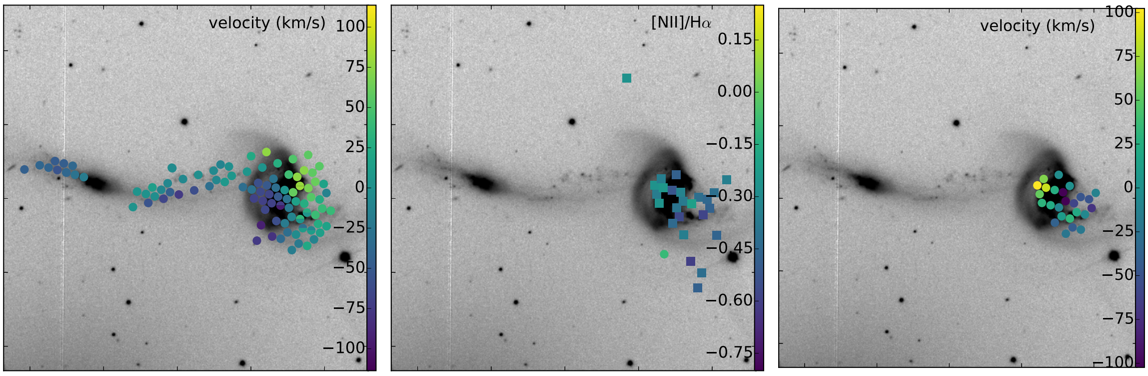

(a) (b) (c)

Figure A.6: **Arp 284**: (a) Velocity map of star forming components. In the secondary galaxy (east) there is no Hα emission near the center. Dynamical modeling of Struck & Smith (2003) suggests that the secondary has been loosing gas to the primary since the first passage about 170 Myr ago, leaving it quiescent. (b) Map of [N II]/Hα of group 2 and 3 galaxies supposedly from shocked gas. They show a cone-like structure. (c) Map of difference in the velocity of broad and narrow components in fibers where two-component fit is preferred. On the right (west), the broad components are blueshifted consistent with outflows. On the left (east), however, the broad components are redshifted consistent with inflows from the secondary galaxy, and in agreement with the dynamical model of Struck & Smith (2003).

made the secondary galaxy quiescent. Smith et al. (2005) observed X-ray emission in the core of the the primary galaxy attributing it to mechanical energy injected by supernovae into to the ISM, or High Mass X-ray Binaries (HMXBs), both as results of the central starburst. In addition, Infrared spectroscopy with Spitzer space telescope shows no evidence of an obscured AGN in the center of the primary, confirming that it is a young unobscured starburst galaxy(Brandl et al., 2004).

We find a vertical cone-like structure by group 2 and 3 components in the primary galaxy shown in Figure A.6b. At first, this structure and its low overall [N II]/Hα ratio suggest that they are the outflows from the central starburst. However, our conclusion changes by looking at the map of difference in velocity of broad and narrow components in fibers where two-component fit is preferred by the F-test. This map is shown in Figure A.6c. There is a gradient in the velocity difference from east to west (left to right). In the western fibers the broad components from panel A.6b are blueshifted with respect to the star forming components from panel A.6a, suggesting outflows from the central starburst, as expected. However, in the eastern double-component fibers which are closer to the smaller companion we find that the broad components are redshifted with respect to the star forming components, suggesting that they are shocked inflows toward the center. This is in excellent agreement with the dynamical model of Struck & Smith (2003) in which gas is being flowing from the secondary companion to the center of the primary galaxy. In NGC 7714 we find shocks from both inflows and outflows.

UGC 12914/5 This system is also known as the "Taffy galaxies", because HI and 4.86 GHz observations by Condon et al. (1993) showed a joined HI and radio continuum bridge between the two galaxies. They suggest that cosmic rays, magnetic fields, and HI gas have been striped from the two galaxies as the result of a nearly head-on collision, about 20 Myrs ago. In the bridge, they find double peaks in the HI profile separated by 100-300 km/s. Braine et al. (2003) finds a significant amount of molecular gas emission (CO) in the bridge, suggesting that 18-35% of total gas mass in the system sits in the bridge. The CO emission does not reveal the double peak and only the high-velocity HI component has a CO counterpart.

Vollmer et al. (2012) modeled the dynamics of this system using a model that includes collisionless halo+stars particles and collisional sticky gas particles. They distinguish the molecular gas from neutral hydrogen using a prescription for total gas density. They find the best-fit model at about 26 Myr after the first pass. Their model reproduces the morphology and kinematics of stars and gas in this system including the prominent gaseous bridge. They also reproduce the double-component HI profile and the single component CO profile in the bridge region. Changing the cloud-cloud collision parameter in their simulation, they argue that the double component profile is produced mainly by the distortion caused by the collisional nature of ISM, and not by the tidal distortions.

Appleton et al. (2015) used the Chandra observatory to show that the bridge also emits a significant amount of X-ray. They showed that 19% of the X-ray luminosity of the the system comes from the bridge. They also used Herschel Far-IR data to estimate the star formation rate (SFR) in the bridge, concluding that SFR is too low to account for X-ray emission via outflows. Moreover, they showed that the peak of the diffuse X-ray emission does not match with the peak of the radio continuum, ruling out a direct connection between the X-ray and synchrotron emission caused by cosmic rays in the bridge. They suggest that the main source of X-ray emission in the bridge is shock heating due to collision of the ISM in the two galaxies as is suggested by Struck (1997). This shocked gas can heat up to $\sim 10^6$ K, and cool down to $\sim 10^5$ K in 35 Myr, and to $\sim 10^4$ K within less than 100 Myr. Based the estimated

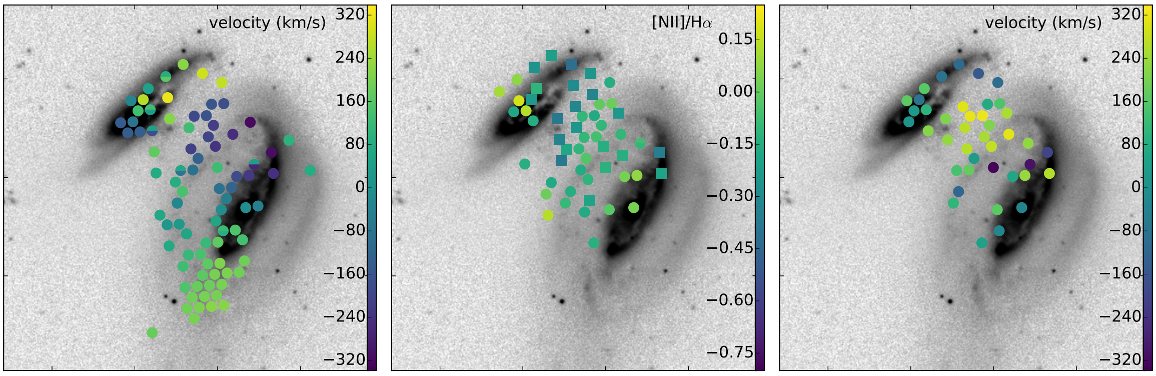

(a) (b) (c)

Figure A.7: **UGC 12914/5**: (a) Velocity map of star forming region. The strong Hα emission from the bridge which is relatively faint in the SDSS r-band image is consistent with strong HI, CO, radio continuum, and X-ray emission from the bridge. Vollmer et al. (2012) proposes a dynamical model in which the galaxies have had a head-on collision about 26 Myr ago. The collision have striped off the gas from both disks into the bridge between them. (b) Map of [N II]/Hα ratio for group 2 and 3 components supposedly from shocked gas. They are located mostly in the bridge region, suggesting the shocks are made by direct collision of gas in the ISM of the two disks. (c) Map of velocity difference between the broad and narrow components in fibers where the two-component fit is preferred by the F-test. The velocity difference $\approx$ 300 km/s is consistent with extended X-ray emission in the bridge region originating from the shocks of similar velocities (Appleton et al., 2015).

time of $\sim$ 26 Myr after the pericenter, the temperature of the observed soft X-ray is consistent with heating with shocks with speed range of 430-570 km/s.

Figure A.7c shows the velocity difference between broad and narrow component in fibers where two component fit is preferred by the F-test. It shows that most of the fibers in the bridge region prefer a double component fit to the Hα emission line. Im most of these fibers, the narrow component meets the criteria for a normal star formation, and the broad component is considered shocked. In most of these double component fits the broad component is significantly red-shifted with respect to the narrow component (> 300 km/s). This suggests that star formation outflows are not responsible for producing the shocks in this region. This velocity difference is consistent with the velocity difference between peaks in the HI profile in the bridge. Based on the velocity difference we can argue that the narrow star forming components shown in figure A.7a correspond to the HI components with CO emission line, and broad shocked components shown in A.7b correspond to the HI component without CO emission. The velocity difference is also consistent with shock speeds required to produce the X-ray emission in the bridge region. Therefore, we confirm that the shocked components in the bridge are produced as a result of the fast collision of gas in the ISM at the time of the first passage.

In Figure A.7a we also find a void of star forming components in the center of UGC 12914. Appleton et al. (2015) find a slightly extended ultra-luminous X-ray source in this location, hinting at the presence of an obscured AGN. Though, the velocity dispersion of the shocked components are not as high as what is expected for AGN hosts (Rich et al., 2014).

UGC 11695: This galaxy and its smaller companion are both spirals close to a face-on view. Both display smooth rotation shown in Figure A.8a. The shocked Hα fraction is $23.9 \pm 1.8\%$ in the whole system. 2MASS Ks-band light ratio is $\approx$ 8. Shocked components are only seen in the primary northern galaxy near the center (Figure A.8b), consistent with shocks being produced by outflows from central starburst.

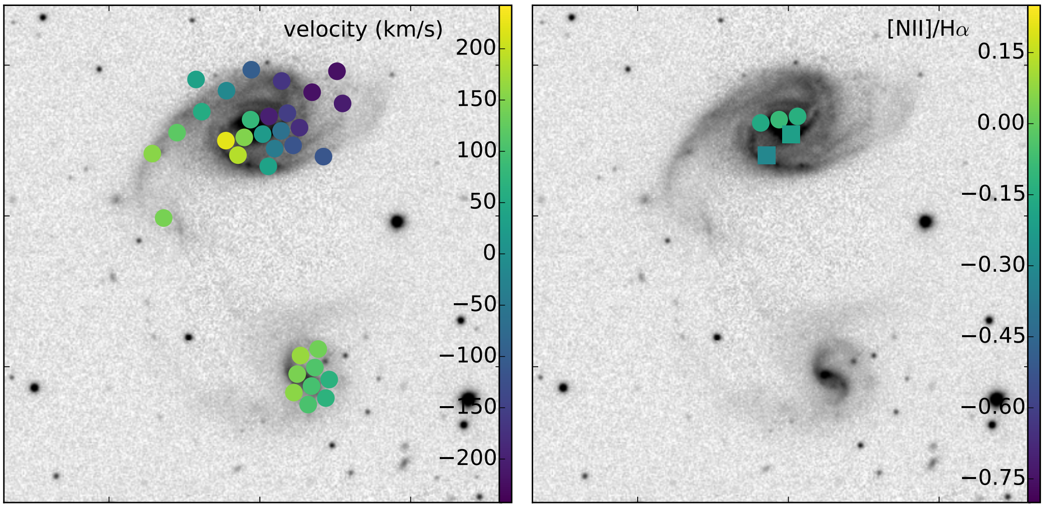

(a) (b)

Figure A.8: **UGC 11695**: (a) Velocity map of star forming components. Both galaxies display star formation throughout the disk. (b) Map of [N II]/Hα of the group 2 and 3 components supposedly from shocked gas. The secondary galaxy has no shocks. the Primary shows shocked components near the center, consistent with central starburst outflows.

arp238: Also known as VV 250, this system is a close pair with strong tidal tails and a bridge that links the galaxies. VV 250a, the south-east companion, is a Luminous Infrared Galaxy (LIRG) in the GOALS sample with $\log(L_{IR}/L_{\odot}) = 11.81$ (Armus et al., 2009). Hattori et al. (2004) shows that most of the Hα flux in this system is being emitted from a compact source in VV 250a.

We find strong Hα along the north-west tail and the bridge. The south-east tail though, shows less Hα emission. The north-west tail has a smooth rotation in star forming components shown in Figure A.9a. We find shocks near the cores of both galaxies. The shocks are stronger near the core of VV 250a as can be seen in Figure A.9b. Assuming that the shocks are related to central starbursts, more

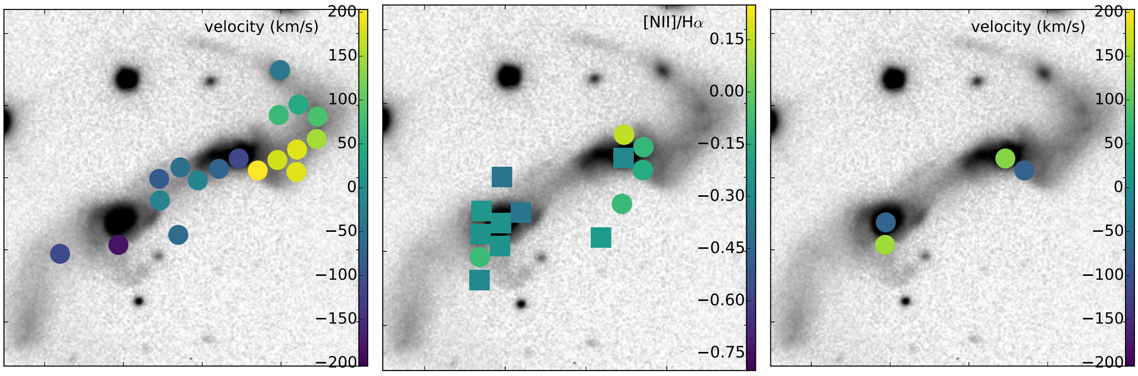

(a) (b) (c)

Figure A.9: **Arp 238**: (a) Velocity map of star forming components. North-west tail hosts star forming regions, but south-east tail does not display much Hα emission. (b) Map of [N II]/Hα four group 2 and 3 components supposedly from shocked has. They are concentrated near the centers, consistent with being related to central starbursts. (c) Map of velocity difference between broad and narrow components in fibers where the two-component fit is preferred. It shows that in three out of four of these fibers, the broad component is redshifted by 80-150 km/s with respect to the narrow star forming component in panel (a), consistent with inflows.

shocks near the south-east core is consistent with its stronger IR luminosity. Figure A.9c shows the difference in velocity of broad and narrow components in fibers where two-component fit is preferred. We find the in three out of four of these fibers the broad component is redshifted by 80-150 km/s with respect to the narrow star forming component, consistent with inflows. Higher spatial resolution near the core is required to understand the process that is producing shocks (similar to Medling et al. 2015).

Arp 87: This is one of the systems we attempted to dynamically model in Chapter 4. Northern galaxy is edge-on and the southern one is tilted but closer to face-on. They both show smooth rotation near the center, as is shown in Figure A.10a. Figure A.10b shows group 2 and 3 components from shocked gas. They are concentrated near

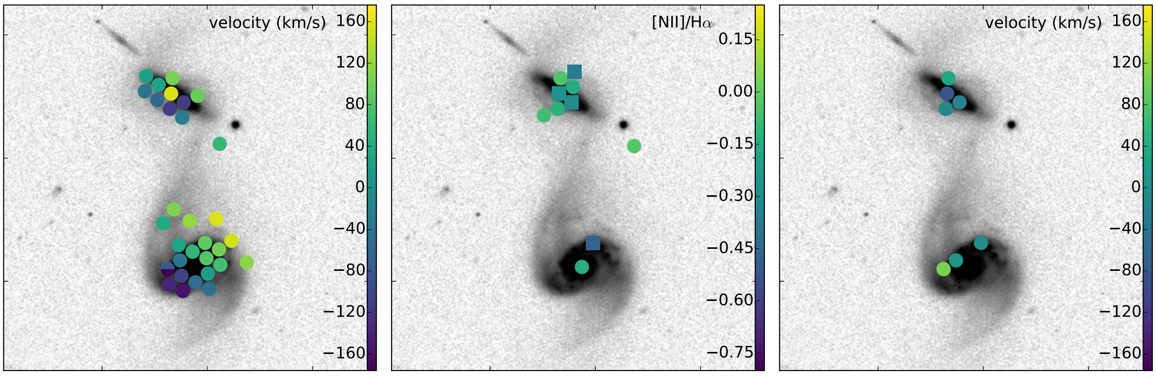

(a) (b) (c)

Figure A.10: **Arp 87**: (a) Velocity map of star forming components. Both galaxies show smooth rotation near the centers. No Hα velocity is found on the end of the tails of the southern galaxy. This negatively affects the constraints one can put on encounter parameters by dynamical modeling of tidal tails. (b) Map of [N II]/Hα for group 2 and 3 components supposedly from shocked gas. (c) Map of velocity difference between narrow and broad components in fibers where two-components fit is preferred by the F-test. Most of the broad components are blueshifted with respect to the narrow components in panel (a), consistent with outflows.

the center, particularly the center of the northern edge-on galaxy. The are consistent with shocks being related to central starburst. Figure A.10c shows the difference in velocity of broad and narrow components in fibers where two-components fit is preferred by the F-test. As can be seen in most of them the broad component is slightly blueshifted with respect to the star forming narrow component consistent with outflows.

NGC 2613: This is a well studied coalesced system with strong tidal tails left from recent interaction. Privon et al. (2013) finds a dynamical model for this system in which the coalescence happened about 80 Myr ago. We find a very high shock fraction of 89.5%±5.0% in it. Figure A.11a shows the few star forming components we find in

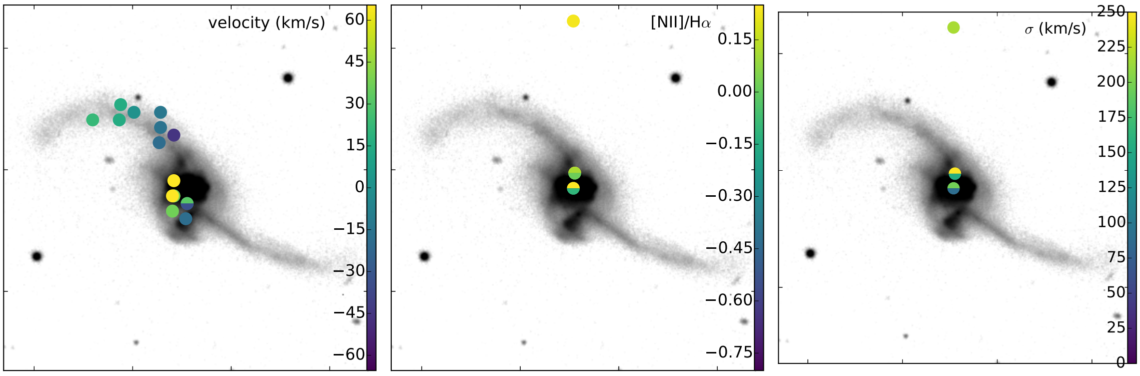

(a) (b) (c)

Figure A.11: **NGC 2623**: (a) Velocity map of star forming components. few components show star forming emission. (b) Map of [N II]/Hα for group 2 and 3 components. The high shocked gas fraction ≈ 90% in this system is because of two bright fibers in the center. (c) Map of velocity dispersion of components in panel (b). These velocity dispersions are consistent with both starburst and AGN in the center.

this system. Figure A.11b indicated that the high shocked gas fraction in this system is because of two bright central fibers. Figure A.11c shows the velocity dispersion of these components. The velocity dispersions are high enough to be consistent with both shocks and AGN hard ionization as is suggested by Rich et al. (2014).

This system is classified as a LINER by Heckman et al. (1983). While Condon et al. (1991) suggests from radio and FIR data that there is a compact starburst in the core, Maiolino et al. (2003) argues from Chandra X-ray observations that the center hosts an obscured AGN. Our data described above is consistent with both. Similar to Arp 238, with an IFU instruments of higher spatial resolution (e.g. MUSE) we would be able to better understand the source of ionization near the nucleus.

NGC 3921: In Figure A.12a we show the star forming components in this system. This system shows little Hα emission from normal HII regions. Schweizer (1996)

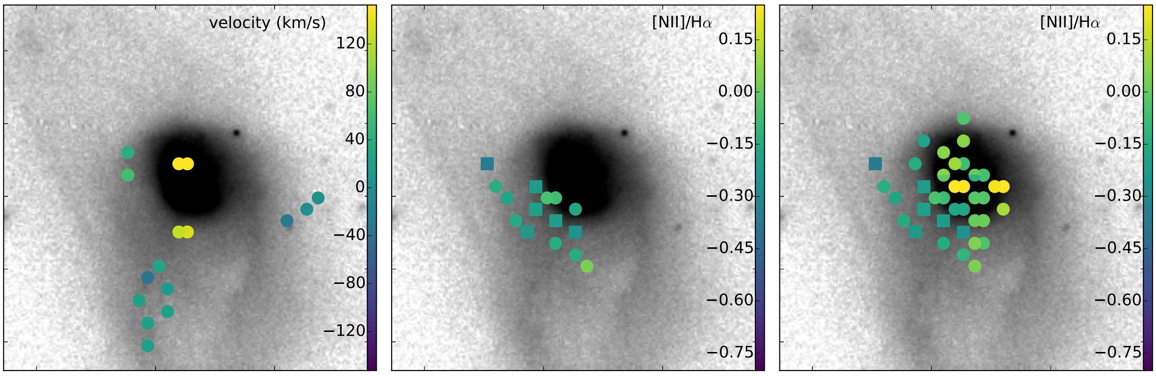

(a) (b) (c)

Figure A.12: **NGC 3921**: (a) Velocity map of star forming components. few components show star forming emission. (b) Map of [N II]/Hα for group 2 and 3 components with putting a cut on Hα EW > 7 Å. (c) Map of [N II]/Hα for group 2 and 3 components withou the cut on Hα EW. comparing panels (b) and (c) suggests that most fibers near the center have low Hα EW, consistent with post-starburst. The cone-like spatial distribution of components in panel (b) suggests that shocks are related to the central past starburst.

suggests from various optical photometric and spectroscopic observations that the main body has a typical post-starburst spectrum. We find very high shocked Hα fraction of ≈ 70% ± 6% in this system. Fibers near the center, show Hα emission with EW<7 Å, mostly because of the strong stellar continuum. So by cutting the fibers with EW<7Å, as described in Chapter 4, we loose the Hα information in the central fibers. In Figures A.12b and A.12c we show [N II]/Hα map of group 2 and 3 components with and without the limit on Hα EW. In both cases these components display a cone-like structure opening toward south-east, suggesting the they are shocks related to the past central starburst.

Bibliography

Acker, A., Köppen, J., Samland, M., & Stenholm, B. 1989, The Messenger, 58, 44

Amram, P., Mendes de Oliveira, C., Boulesteix, J., & Balkowski, C. 1998, Astronomy and Astrophysics, 330, 881

Appleton, P. N., et al. 2015, The Astrophysical Journal, 812, 118

Armus, L., Heckman, T. M., & Miley, G. K. 1990, The Astrophysical Journal, 364, 471

Armus, L., et al. 2009, Publications of the Astronomical Society of Pacific, 121, 559

Arp, H. 1966, Astrophysical Journal Supplement, 14, 1

Baldwin, J. A., Phillips, M. M., & Terlevich, R. 1981, Astronomical Society of the Pacific, 93, 5

Barnes, J. E. 1988, The Astrophysical Journal, 331, 699

—. 2004, Monthly Notices of the Royal Astronomical Society, 350, 798

—. 2011, Monthly Notices of the Royal Astronomical Society, 413, 2860

—. 2016, Monthly Notices of the Royal Astronomical Society, 455, 1957

Barnes, J. E., & Hernquist, L. 1996, Astrophysical Journal v.471, 471, 115

Barnes, J. E., & Hibbard, J. E. 2009, The Astronomical Journal, 137, 3071

Barton, E. J., Geller, M. J., & Kenyon, S. J. 2000, The Astrophysical Journal, 530, 660

Bell, E. F., et al. 2012, The Astrophysical Journal, 753, 167

—. 2004, The Astrophysical Journal, 608, 752

Bender, R., Surma, P., Doebereiner, S., Moellenhoff, C., & Madejsky, R. 1989, Astronomy and Astrophysics, 217, 35

Benson, A. J. 2005, Monthly Notices of the Royal Astronomical Society, 358, 551

Benson, A. J., Bower, R. G., Frenk, C. S., Lacey, C. G., Baugh, C. M., & Cole, S. 2003, The Astrophysical Journal, 599, 38

Bershady, M. A., Andersen, D. R., Harker, J., Ramsey, L. W., & Verheijen, M. A. W. 2004, Publications of the Astronomical Society of the Pacific, 116, 565

Binney, J., & Tremaine, S. 2008, Galactic Dynamics: Second Edition, by James Binney and Scott Tremaine. ISBN 978-0-691-13026-2 (HB). Published by Princeton University Press, Princeton, NJ USA, 2008.,

Birnboim, Y., & Dekel, A. 2011, Monthly Notices of the Royal Astronomical Society, 415, 2566

Bois, M., et al. 2011, Monthly Notices of the Royal Astronomical Society, 416, 1654

Booth, R. S., de Blok, W. J. G., Jonas, J. L., & Fanaroff, B. 2009, arXiv.org, 2935

Borne, K. D., & Richstone, D. O. 1991, Astrophysical Journal, 369, 111

Boylan-Kolchin, M., Ma, C.-P., & Quataert, E. 2005, Monthly Notices of the Royal

Astronomical Society, 362, 184

Braine, J., Davoust, E., Zhu, M., Lisenfeld, U., Motch, C., & Seaquist, E. R. 2003, Astronomy and Astrophysics, 408, L13

Brandl, B. R., et al. 2004, The Astrophysical Journal Supplement Series, 154, 188

Bridge, C. R., Carlberg, R. G., & Sullivan, M. 2010, The Astrophysical Journal, 709, 1067

Brown, M. J. I., Dey, A., Jannuzi, B. T., Brand, K., Benson, A. J., Brodwin, M., Croton, D. J., & Eisenhardt, P. R. 2007, The Astrophysical Journal, 654, 858

Bundy, K., et al. 2015, The Astrophysical Journal, 798, 7

Burkert, A., Naab, T., Johansson, P. H., & Jesseit, R. 2008, The Astrophysical Journal, 685, 897

Cappellari, M., et al. 2011, Monthly Notices of the Royal Astronomical Society, 413, 813

Cigan, P. 2004, Reducing Multi-fiber Spectra in IRAF with DOHYDRA: A Guide by Phil Cigan - retrieved from http://www.astro.wisc.edu/ cigan/reducing/reducing.html

Collaboration, L. S., et al. 2009, arXiv.org, arXiv:0912.0201

Condon, J. J., Helou, G., Sanders, D. B., & Soifer, B. T. 1993, Astronomical Journal (ISSN 0004-6256), 105, 1730

Condon, J. J., Huang, Z. P., Yin, Q. F., & Thuan, T. X. 1991, The Astrophysical Journal, 378, 65

Cox, T. J., Dutta, S. N., Di Matteo, T., Hernquist, L., Hopkins, P. F., Robertson, B., & Springel, V. 2006a, The Astrophysical Journal, 650, 791

Cox, T. J., Jonsson, P., Primack, J. R., & Somerville, R. S. 2006b, Monthly Notices of the Royal Astronomical Society, 373, 1013

Cox, T. J., Jonsson, P., Somerville, R. S., Primack, J. R., & Dekel, A. 2008, Monthly Notices of the Royal Astronomical Society, 384, 386

Croom, S. M., et al. 2012, Monthly Notices of the Royal Astronomical Society, 421, 872

Damjanov, I., et al. 2009, The Astrophysical Journal, 695, 101

Davies, R. L., Kewley, L. J., Ho, I. T., & Dopita, M. A. 2014, Monthly Notices of the Royal Astronomical Society, 444, 3961

de Grijs, R., Lee, J. T., Clemencia Mora Herrera, M., Fritze-v Alvensleben, U., & Anders, P. 2003, New Astronomy, 8, 155

Delgado, R. M. G., García-Vargas, M. L., Goldader, J., Leitherer, C., & Pasquali, A. 1998, arXiv.org, 707

Di Matteo, T., Colberg, J., Springel, V., Hernquist, L., & Sijacki, D. 2008, The Astrophysical Journal, 676, 33

Díaz, R., Rodrigues, I., Dottori, H., & Carranza, G. 2000, The Astronomical Journal, 119, 111

Dopita, M. A., & Sutherland, R. S. 1995, Astrophysical Journal v.455, 455, 468

Draine, B. T. 2011, Physics of the Interstellar and Intergalactic Medium by Bruce T.

Draine. Princeton University Press, 2011. ISBN: 978-0-691-12214-4,

Dubinski, J., Mihos, J. C., & Hernquist, L. 1995, arXiv.org, 576

—. 1999, The Astrophysical Journal, 526, 607

Duc, P. A., Brinks, E., Springel, V., Pichardo, B., Weilbacher, P., & Mirabel, I. F. 2000, The Astronomical Journal, 120, 1238

Dyson, F. 2004, Nature, 427, 297

Ellison, S. L., Patton, D. R., Mendel, J. T., & Scudder, J. M. 2011, Monthly Notices of the Royal Astronomical Society, 418, 2043

Ellison, S. L., Patton, D. R., Simard, L., & McConnachie, A. W. 2008, The Astronomical Journal, 135, 1877

Emsellem, E., et al. 2007, Monthly Notices of the Royal Astronomical Society, 379, 401

—. 2011, Monthly Notices of the Royal Astronomical Society, 414, 888

Erb, D. K., Steidel, C. C., Shapley, A. E., Pettini, M., Reddy, N. A., & Adelberger, K. L. 2006, The Astrophysical Journal, 647, 128

Faber, S. M., et al. 1997, The Astronomical Journal, 114, 1771

—. 2007, The Astrophysical Journal, 665, 265

Fabian, A. C. 1999, Monthly Notices of the Royal Astronomical Society, 308, L39

Fakhouri, O., Ma, C.-P., & Boylan-Kolchin, M. 2010, Monthly Notices of the Royal Astronomical Society, 406, 2267

Gao, Y., Zhu, M., & Seaquist, E. R. 2003, The Astronomical Journal, 126, 2171

Geller, M. J., Kenyon, S. J., Barton, E. J., Jarrett, T. H., & Kewley, L. J. 2006, The Astronomical Journal, 132, 2243

Genel, S., Genzel, R., Bouché, N., Naab, T., & Sternberg, A. 2009, The Astrophysical Journal, 701, 2002

Genel, S., et al. 2014, Monthly Notices of the Royal Astronomical Society, 445, 175

Glikman, E., Simmons, B., Mailly, M., Schawinski, K., Urry, C. M., & Lacy, M. 2015, The Astrophysical Journal, 806, 218

Governato, F., et al. 2009, Monthly Notices of the Royal Astronomical Society, 398, 312

—. 2012, Monthly Notices of the Royal Astronomical Society, 422, 1231

Hattori, T., et al. 2004, The Astronomical Journal, 127, 736

Heckman, T. M., Armus, L., & Miley, G. K. 1990, Astrophysical Journal Supplement Series (ISSN 0067-0049), 74, 833

Heckman, T. M., van Breugel, W., Miley, G. K., & Butcher, H. R. 1983, The Astronomical Journal, 88, 1077

Henry, R. B. C., & Worthey, G. 1999, Publications of the Astronomical Society of the Pacific, 111, 919

Hibbard, J. E., et al. 2005, The Astrophysical Journal, 619, L87

Hibbard, J. E., Guhathakurta, P., van Gorkom, J. H., & Schweizer, F. 1994, The Astronomical Journal, 107, 67

Hibbard, J. E., & Mihos, J. C. 1995, Astronomical Journal v.110, 110, 140

Hibbard, J. E., & van Gorkom, J. H. 1996a, The Astronomical Journal, 111, 655

—. 1996b, The Astronomical Journal, 111, 655

Holincheck, A. J., et al. 2016, Monthly Notices of the Royal Astronomical Society, 459, 720

Hooper, E., Sell, P., Wolf, M., Wojtaszek, M., Mosby, G., Mikayla, K., Moravec, E., & Grififith, Z. 2014, Guide to Reducing IFU Data, 2014 - retrieved from http://www.astro.wisc.edu/ mab/research/hexpak$_{g}radpak/pak_{r}eduction_{g}uide_{2}1nov2014.pdf$

Hopkins, A. M., & Beacom, J. F. 2006, The Astrophysical Journal, 651, 142

Hopkins, P. F., Cox, T. J., Younger, J. D., & Hernquist, L. 2009, The Astrophysical Journal, 691, 1168

Hopkins, P. F., Hernquist, L., Cox, T. J., Di Matteo, T., Robertson, B., & Springel, V. 2006, The Astrophysical Journal Supplement Series, 163, 1

Hopkins, P. F., Hernquist, L., Cox, T. J., & Kereš, D. 2008, The Astrophysical Journal Supplement Series, 175, 356

Hopkins, P. F., & Quataert, E. 2011, Monthly Notices of the Royal Astronomical Society, 415, 1027

Jog, C. J., & Solomon, P. M. 1992, The Astrophysical Journal, 387, 152

Jogee, S., et al. 2009, The Astrophysical Journal, 697, 1971

Johnston, S., et al. 2008, Experimental Astronomy, 22, 151

Joseph, R. D., Wright, G. S., & Prestwich, A. H. 1986, New Insights in Astrophysics. Eight Years of UV Astronomy with IUE, 263, Karachentsev, I., Lebedev, V., & Shcherbanovski, A. 1985, Bulletin d'Information du Centre de Donnees Stellaires, 29, 87

Kartaltepe, J. S., et al. 2007, The Astrophysical Journal Supplement Series, 172, 320

Kauffmann, G., et al. 2003, Monthly Notices of the Royal Astronomical Society, 346, 1055

Kazantzidis, S., Bullock, J. S., Zentner, A. R., Kravtsov, A. V., & Moustakas, L. A. 2008, The Astrophysical Journal, 688, 254

Keel, W. C., Kennicutt, R. C. J., Hummel, E., & van der Hulst, J. M. 1985, Astronomical Journal (ISSN 0004-6256), 90, 708

Kennicutt, R. C. J. 1998, Annual Review of Astronomy and Astrophysics, 36, 189

Kewley, L. J., Geller, M. J., & Barton, E. J. 2006a, The Astronomical Journal, 131, 2004

Kewley, L. J., Groves, B., Kauffmann, G., & Heckman, T. 2006b, Monthly Notices of the Royal Astronomical Society, 372, 961

Kewley, L. J., Rupke, D., Zahid, H. J., Geller, M. J., & Barton, E. J. 2010, The Astrophysical Journal Letters, 721, L48

Khochfar, S., & Burkert, A. 2006, Astronomy and Astrophysics, 445, 403

Kinney, A. L., Bohlin, R. C., Calzetti, D., Panagia, N., & Wyse, R. F. G. 1993, The Astrophysical Journal Supplement Series, 86, 5

Kormendy, J., & Kennicutt, R. C. J. 2004, Annual Review of Astronomy &Astrophysics, 42, 603

Krajnović, D., et al. 2011, Monthly Notices of the Royal Astronomical Society, 414, 2923

Landau, L. D., & Lifshitz, E. M. 1959, Course of theoretical physics, Oxford: Pergamon Press, 1959,

Larson, R. B., & Tinsley, B. M. 1978, The Astrophysical Journal, 219, 46

Law, D. R., & Majewski, S. R. 2010, The Astrophysical Journal, 714, 229

Lee, J. C., Salzer, J. J., & Melbourne, J. 2004, The Astrophysical Journal, 616, 752

Leslie, S. K., Rich, J. A., Kewley, L. J., & Dopita, M. A. 2014, Monthly Notices of the Royal Astronomical Society, 444, 1842

Lilly, S. J., Le Fèvre, O., Hammer, F., & Crampton, D. 1996, The Astrophysical Journal, 460

Lintott, C., et al. 2010, Monthly Notices of the Royal Astronomical Society, 410, 166

Lomax, R. G. 2007, Statistical Concepts: A Second Course (2007)

Lotz, J. M., Jonsson, P., Cox, T. J., Croton, D., Primack, J. R., Somerville, R. S., & Stewart, K. 2011, The Astrophysical Journal, 742, 103

Lotz, J. M., Jonsson, P., Cox, T. J., & Primack, J. R. 2008, Monthly Notices of the Royal Astronomical Society, 391, 1137

Madau, P., Ferguson, H. C., Dickinson, M. E., Giavalisco, M., Steidel, C. C., & Fruchter, A. 1996, Monthly Notices of the Royal Astronomical Society, 283, 1388

Maiolino, R., et al. 2003, Monthly Notices of the Royal Astronomical Society, 344, L59

Medling, A. M., et al. 2015, arXiv.org, 2301

Mihos, J. C., Bothun, G. D., & Richstone, D. O. 1993, Astrophysical Journal v.418, 418, 82

Mihos, J. C., & Hernquist, L. 1996, Astrophysical Journal v.464, 464, 641

Mo, H., van den Bosch, F. C., & White, S. 2010, Galaxy Formation and Evolution, by Houjun Mo , Frank van den Bosch , Simon White, Cambridge, UK: Cambridge University Press, 2010,

Monreal-Ibero, A., Arribas, S., & Colina, L. 2006, The Astrophysical Journal, 637, 138

Monreal-Ibero, A., Arribas, S., Colina, L., Rodriguez-Zaurin, J., Alonso-Herrero, A., & Garcia-Marin, M. 2010a, arXiv.org, A28

Monreal-Ibero, A., Vílchez, J. M., Walsh, J. R., & Muñoz-Tuñón, C. 2010b, Astronomy and Astrophysics, 517, A27

Mortazavi, S. A., Lotz, J. M., Barnes, J. E., & Snyder, G. F. 2016, Monthly Notices of the Royal Astronomical Society, 455, 3058

Moster, B. P., Macciò, A. V., Somerville, R. S., Johansson, P. H., & Naab, T. 2010, Monthly Notices of the Royal Astronomical Society, 403, 1009

Naab, T., & Burkert, A. 2003, The Astrophysical Journal, 597, 893

Naab, T., et al. 2014, Monthly Notices of the Royal Astronomical Society, 444, 3357

Narayanan, D., et al. 2008, The Astrophysical Journal Supplement Series, 176, 331

Navarro, J. F., Frenk, C. S., & White, S. D. M. 1996, The Astrophysical Journal, 462, 563

Nikolic, B., Cullen, H., & Alexander, P. 2004, Monthly Notices of the Royal Astronomical Society, 355, 874

Norman, C., & Scoville, N. 1988, The Astrophysical Journal, 332, 124

Oppenheimer, B. D., Davé, R., Kereš, D., Fardal, M., Katz, N., Kollmeier, J. A., & Weinberg, D. H. 2010, Monthly Notices of the Royal Astronomical Society, 406, 2325

Oser, L., Naab, T., Ostriker, J. P., & Johansson, P. H. 2012, The Astrophysical Journal, 744, 63

Patton, D. R., Ellison, S. L., Simard, L., McConnachie, A. W., & Mendel, J. T. 2011, Monthly Notices of the Royal Astronomical Society, 412, 591

Patton, D. R., Grant, J. K., Simard, L., Pritchet, C. J., Carlberg, R. G., & Borne, K. D. 2005, The Astronomical Journal, 130, 2043

Privon, G. C., Barnes, J. E., Evans, A. S., Hibbard, J. E., Yun, M. S., Mazzarella, J. M., Armus, L., & Surace, J. 2013, The Astrophysical Journal, 771, 120

Quinn, P. J., Hernquist, L., & Fullagar, D. P. 1993, The Astrophysical Journal, 403, 74

Repetto, P., Rosado, M., Gabbasov, R., & Fuentes-Carrera, I. 2010, The Astronomical Journal, 139, 1600

Rich, J. A., Kewley, L. J., & Dopita, M. A. 2011, The Astrophysical Journal, 734, 87

—. 2014, The Astrophysical Journal, 781, L12

—. 2015, The Astrophysical Journal Supplement Series, 221, 28

Robertson, B., Cox, T. J., Hernquist, L., Franx, M., Hopkins, P. F., Martini, P., & Springel, V. 2006, The Astrophysical Journal, 641, 21

Rodriguez-Gomez, V., et al. 2015, Monthly Notices of the Royal Astronomical Society, 449, 49

—. 2016, Monthly Notices of the Royal Astronomical Society, 458, 2371

Sánchez, S. F., et al. 2012, Astronomy and Astrophysics, 538, A8

Sanders, D. B., Mazzarella, J. M., Kim, D. C., Surace, J. A., & Soifer, B. T. 2003, The Astronomical Journal, 126, 1607

Sanders, D. B., & Mirabel, I. F. 1996, Annual Review of Astronomy and Astrophysics, 34, 749

Scharwächter, J., Eckart, A., Pfalzner, S., Zuther, J., Krips, M., & Straubmeier, C. 2004, Astronomy and Astrophysics, 414, 497

Schweizer, F. 1996, The Astronomical Journal, 111, 109

Shamir, L., Holincheck, A., & Wallin, J. 2013, Astronomy and Computing, 2, 67

Sharp, R. G., & Bland-Hawthorn, J. 2010, The Astrophysical Journal, 711, 818

Silk, J., & Rees, M. J. 1998, Astronomy and Astrophysics, 331, L1

Skrutskie, M. F., et al. 2006, The Astronomical Journal, 131, 1163

Smith, B., Higdon, J., Higdon, S., & Bastian, N. 2010, Galaxy Mergers in an Evolving Universe, 423,

Smith, B. J., Struck, C., Hancock, M., Appleton, P. N., Charmandaris, V., & Reach,

W. T. 2007, The Astronomical Journal, 133, 791

Smith, B. J., Struck, C., & Nowak, M. A. 2005, The Astronomical Journal, 129, 1350

Smith, B. J., & Wallin, J. F. 1992, Astrophysical Journal, 393, 544

Snyder, G. F., Cox, T. J., Hayward, C. C., Hernquist, L., & Jonsson, P. 2011, The Astrophysical Journal, 741, 77

Soto, K. T., & Martin, C. L. 2012, The Astrophysical Journal Supplement, 203, 3

Springel, V. 2000, Monthly Notices of the Royal Astronomical Society, 312, 859

Springel, V., Di Matteo, T., & Hernquist, L. 2005, The Astrophysical Journal, 620, L79

Springel, V., & White, S. D. M. 1999, Monthly Notices of the Royal Astronomical Society, 307, 162

Struck, C. 1997, The Astrophysical Journal Supplement Series, 113, 269

Struck, C., Kaufman, M., Brinks, E., Thomasson, M., Elmegreen, B. G., & Meloy Elmegreen, D. 2005, Monthly Notices of the Royal Astronomical Society, 364, 69

Struck, C., & Smith, B. J. 2003, The Astrophysical Journal, 589, 157

Theis, C., & Harfst, S. 2000, Galaxy Mergers in an Evolving Universe, 197, 357

Theis, C., & Kohle, S. 2001, Astronomy and Astrophysics, 370, 365

Theis, C., & Spinneker, C. 2003, Astrophysics and Space Science, 284, 495

Theys, J. C., & Spiegel, E. A. 1977, Astrophysical Journal, 212, 616

Tody, D. 1986, Instrumentation in astronomy VI, 627, 733

—. 1993, Astronomical Data Analysis Software and Systems II, 52, 173

Toomre, A. 1977, Evolution of Galaxies and Stellar Populations, 401

Toomre, A., & Toomre, J. 1972, Astrophysical Journal, 178, 623

Torrey, P., Cox, T. J., Kewley, L., & Hernquist, L. 2012, The Astrophysical Journal, 746, 108

Towns, J., et al. 2014, 16, 62

van Dokkum, P. G. 2001, arXiv.org, 1420

van Dokkum, P. G., et al. 2008, The Astrophysical Journal Letters, 677, L5

—. 2010, The Astrophysical Journal, 709, 1018

Vollmer, B., Braine, J., & Soida, M. 2012, Astronomy and Astrophysics, 547, A39

Wahde, M. 1998, Astronomy and Astrophysics Supplement Series, 132, 417

Wahde, M., & Donner, K. J. 2001, Astronomy and Astrophysics, 379, 115

Wellons, S., et al. 2015, Monthly Notices of the Royal Astronomical Society, 449, 361

White, S. D. M. 1978, Monthly Notices of the Royal Astronomical Society, 184, 185

White, S. D. M., & Rees, M. J. 1978, Monthly Notices of the Royal Astronomical Society, 183, 341

Whitmore, B. C., & Schweizer, F. 1995, The Astronomical Journal, 109, 960

Wild, V., Heckman, T., & Charlot, S. 2010, Monthly Notices of the Royal Astronomical Society

Wild, V., et al. 2014, Astronomy and Astrophysics, 567, A132

Windhorst, R. A., et al. 2002, The Astrophysical Journal Supplement Series, 143, 113

Wylezalek, D., Zakamska, N. L., Liu, G., & Obied, G. 2016, Monthly Notices of the Royal Astronomical Society, 457, 745

York, D. G., et al. 2000, The Astronomical Journal, 120, 1579

Yun, M. S., & Hibbard, J. E. 2001, The Astrophysical Journal, 550, 104

Vita

S. Alireza Mortazavi was born in 1984 in Tehran, Iran. In 2002, he graduated from Allameh Helli high school, and started college as a physics major at Sharif University of Technology (SUT) in Tehran. He also received his Master of Science degree from SUT before he moved to Baltimore, Maryland in 2008, to enroll in the Physics and Astronomy PhD program at Johns Hopkins University. Since the beginning of 2011 he has been working on galaxy mergers with Dr. Jennifer Lotz.